Study of Grain Growth in the Early Phases of Protostars: From Envelopes to Disks

Carolina Agurto Gangas

SIGILL·UNIVERSI·TAT·LUDOVIC·MAXIM

München 2020

Study of Grain Growth in the Early Phases of Protostars: From Envelopes to Disks

Carolina Agurto Gangas

Dissertation
an der Fakultät für Physik
der Ludwig–Maximilians–Universität
München

vorgelegt von
Carolina Agurto Gangas
aus Valparaíso, Chile

München, den 17. August 2020

Erstgutachter: Prof. Dr. Paola Caselli
Zweitgutachter: Prof. Dr. Til Birnstiel
Tag der mündlichen Prüfung: 22. September 2020

> “We all have an unsuspected reserve of strength inside that emerges when life puts us to the test.”
>
> ---
>
> *Island Beneath the Sea*
> *Isabel Allende*

Contents

List of Figures

List of Tables

Zusammenfassung

Die Untersuchung der Eigenschaften des Staubes um junge Protosterne ist entscheidend um zu verstehen, wie früh im Bildungsprozess von Sternen und Planeten, Staubkörner effizient zu koagulieren beginnen und sich von mikrometer-großen Partikeln zu Kieselsteinen und dann zu Planetesimalen entwickeln. Die physikalischen und Staub-Eigenschaften des kollabierenden Wolken-Materials und deren Verbindung mit den Scheibendimensionen sind jedoch noch unzureichend verstanden. Neuere Studien haben Sub-mm/mm-Beobachtungen analysiert, um zu untersuchen, wie effektiv die Staub-Koagulation in den frühesten Stadien der Sternentstehung ist. Allerdings sind die Erkenntnisse über die Korngrößen immer noch nicht schlüssig. Diese Arbeit konzentriert sich auf Per-emb-50, einen Protostern der Klasse I, der sich im Komplex NGC 1333 innerhalb des Sternentstehungsgebietes Perseus befindet. Dies ist die erste selbstkonsistente Strahlungstransfermodellierung dieser Quelle, die gleichzeitig die Scheiben-, Hüllkurven- und Staubeigenschaften durch Anpassung der Multi-Wellenlängen-Beobachtungen einschränkt.

Im ersten Teil dieser Arbeit untersuchte ich den Staub und die physikalischen Eigenschaften der inneren Hülle von Per-emb-50 innerhalb von 3000 au durch Verwendung von interferometrischen Beobachtungen von NOEMA (NOrthern Erweitertes Millimeter-Array) und SMA (Submillimeter-Array) im Millimeter-Wellenlängenbereich. Beide Datensätze werden durch analytische Modelle angepasst, um einen Vergleich mit früheren Studien zu ziehen, und werden schließlich mit vollständigen Strahlungstranfermodellen gefittet. Der Scheibenradius, die Scheibenmasse, die Hülldichte-Struktur und die Hüllkorngröße werden als freie Parameter bei der Rastersuche belassen. Ich bin zu dem Ergebnis gekommen, dass das Niveau des Kornwachstums gefunden wurde, mit einer maximalen Korngröße von 100 μm, oder niedriger. Diese Arbeit ergab auch, dass die Einbeziehung der Hüllstruktur notwendig ist, um die thermische Emission auf der Scheibe richtig zu modellieren. Tatsächlich wird der Effekt der thermischen Emission der Hülle auf die Scheibe (d.h. die Rückwärmung) bei diesen Objekten oft ignoriert. Die Vorwärmung kann, abhängig vom einigen zehn bis zu hundert Kelvin, Aus diesem Grund kann eine solche Rückwärmung auch die Gasphasenchemie und die Staubmantelchemie in jungen Quellen beeinflussen.

Der zweite Teil dieser Arbeit ist eine erweiterte Analyse der Scheibeneigenschaften von Per-emb-50. Insbesondere habe ich hochauflösende Daten aus VLA (Very Large Array)-Beobachtungen mit einer Auflösung von ∼20 au kombiniert, die es erlaubt, die Compact Disk zu untersuchen. Die neuen Multi-Wellenlängen-Strahlungstransfer-Modelle zeigten, dass die maximale Korngröße in den äußeren Bereichen der Scheibe, im optisch dünnen

Bereich zwischen 25 und 38 au, mit Körnern konsistent ist, die größer als 700 μm sind. Zusätzlich habe ich neue Grenzwerte für den Scheibenradius und die Staubmasse abgeleitet, die präziser sind als frühere, auf analytischen Methoden basierende Studien. Darüber hinaus legt die abgeleitete Scheibenmasse für Per-emb-50 nahe, dass dieser Protostern der Klasse I genügend Masse hat, um zukünftige Riesenplaneten zu bilden, wenn man einen minimalen Massenbudget von 0.01 $M_\odot$ in Betracht zieht. Bis heute ist dies die detaillierteste selbstkonsistente Modellierung eines Protosterns der Klasse I, bei der große und kleine Maßstäbe und Beobachtungen kombiniert werden.

Der letzte Teil dieser Arbeit konzentriert sich auf den Anpassungsrahmen SiDE (Simple Disk Envelope fit). Die vorherige Analyse führte ein großes Gitter von Strahlungstransfermodellen aus, die einen enormen Aufwand an Rechenressourcen und Zeit erfordern; ein Nachteil dabei ist, dass für jeden Parameter eine diskrete Anzahl von Werten untersucht wird. Dieses Rahmenwerk, das während dieser Arbeit entwickelt und getestet wurde, kombiniert die Strahlungstransport-Modellierung, die Verarbeitung der Sichtbarkeiten von MehrwellenŁangen-Beobachtungen und das Markov Chain Monte Carlo emcee Sampler-Tool zur effizienten Untersuchung eines großen Parameterraums. Dieses Werkzeug wird dringend benötigt, da Typische Studien zu planetaren Scheiben müssen eine große Anzahl von Parametern untersuchen. Dazu gehört die Anpassung von Hunderttausenden von Datenpunkt-Beobachtungen, oder sogar Millionen im Falle von ALMA (Atacama Large Millimeter/Sub-Millimeter Array). Um monatelange rechnerische Berechnungen und Analyse zu ersparen, wird dieses Werkzeug (Sampler-Tool) daher dringend benötigt. Dieses Werkzeug ist auch für die Analyse zukünftiger Multi-Wellenlängen-Beobachtungen von großen Gruppen junger Protosterne mit interferometrischen Arrays wie ALMA. Dies wird uns ermöglichen das frühe Kornwachstum zu verstehen. Schließlich hat diese Arbeit ein neues Beispiel geliefert, das zeigt, dass wir nur durch eine detaillierte Strahlungsübertragung-Modellierung die Herausforderung bewältigen können, die Scheiben- und Füllmassen, sowie deren physikalischen und Staub-Eigenschaften effizient auseinanderzuhalten.

Abstract

The study of the properties of the dust around young protostars is crucial for understanding how early in the star and planet formation process dust grains start to efficiently coagulate and evolve from micron sized particles to pebbles and then planetesimals. However, the physical and dust properties of the collapsing cloud material and their connection with the disk scales are still poorly understood. Recent studies have analyzed sub-mm/mm observations to probe how effective is the dust coagulation in the earliest stages of star formation, but the findings about grain sizes are still not conclusive.
This thesis focuses on Per-emb-50, a Class I protostar located in the complex NGC 1333 within the Perseus star forming region. This is the first self-consistent radiative transfer modeling of this source that constrains the disk, envelope and dust properties simultaneously by fitting multi-wavelength observations.

In the first part of this work I studied the dust and physical properties of the inner envelope of Per-emb-50, within 3000 au, by using NOEMA (NOrthern Extended Millimeter Array) and SMA (Submillimeter Array) interferometric observations at millimeter wavelengths. Both data-sets are fitted with analytical models to compare with previous studies and then fitted by full radiative transfer models. The disk radius, disk mass, envelope density structure and envelope grain size are left as free parameters in the grid search. I find that the level of grain growth in the inner envelope of Per-emb-50 is substantially lower than what is found for other young sources, with a maximum grain size of 100 μm or lower. This work also revealed that the inclusion of the envelope structure is necessary to properly model the thermal emission on the disk. Indeed, the effect of the envelope thermal emission on the disk (i.e. backwarming), is often ignored for those objects. The backwarming, depending of the envelope density profile, can significantly change the disk's temperature, from a few tens to hundred Kelvin, therefore, it can also affect the gas phase chemistry and the dust mantle chemistry in young sources.

The second part of this thesis is an extended analysis of the disk properties of Per-emb-50. In particular, I combined high resolution data from VLA (Very Large Array) observations with a ~20 au resolution that allows to study the compact disk. The new multi-wavelength radiative transfer models revealed that the maximum grain size in the outer regions of the disk, in the optically thin region between 25 and 38 au, is consistent with grains larger than 700 μm. I also derived new limits for the disk radius and dust mass, which are more refined than previous studies based on analytical methods. Additionally, the derived disk mass for Per-emb-50 suggests that this Class I protostar has enough mass

to form futures giant planets considering a budget threshold of $0.01\,M_{\odot}$. To date, this is the most detailed self-consistent modeling on a Class I protostar combining large and small scales and observations.

The last part of this thesis focuses on the fitting framework `SiDE` (Simple Disk Envelope fit). The previous analysis ran a large grid of radiative transfer models, which require a huge amount of computational resources and time and it has the disadvantage of exploring a discrete number of values for each parameter. This framework, which was developed and tested during this thesis, combines the radiative transfer modelling, the processing of the visibilities of multi-wavelength observations, and the Markov Chain Monte Carlo `emcee` sampler tool to efficiently explore a large parameter space. This tool is highly required, as typical protoplanetary disk studies need to explore a large number of parameters, fitting hundreds of thousands of data point observations, or even millions in case of ALMA (Atacama Large Millimeter/sub-millimeter Array), which can save months of computational calculations and analysis. This tool is also designed to analyze future multi-wavelength observations of large samples of young protostars with interferometric arrays as ALMA, that will allow us to understand the early grain growth. Finally, this work has provided a new example which shows that only through a detailed radiative transfer modeling we can overcome the challenge of robustly disentangling the disk and envelope masses as well as their physical and dust properties.

Chapter 1

Introduction

1.1 Low mass star formation process

Low-mass stars form from the fragmentation of a molecular cloud into one or more bound cores. These gravitational bound cores are internally supported by the contribution of thermal pressure, magnetic fields and turbulence. The criteria commonly used to understand how star formation is initiated is given by the Jeans-length (Jeans, 1902): $\lambda_J = (\pi c_c^2/G\rho)^{1/2}$, where $c_c^2 = kT/\mu$ is the isothermal sound speed, T is the gas temperature in the molecular cloud, typically 10 K, μ is the molecular weight ($\sim 2.3\,m_{\mathrm{H}}$), G is the gravitational constant, and ρ the local density which is of the order of 10^3-10^4 molecules per cm^{-3} for a typical molecular cloud. When the size λ exceeds λ_J, the thermal pressure is not enough to resist self-gravity and a quick collapse take place. The contraction continues until the central region becomes opaque and the temperature increases.

During the evolution of the bound core (see Fig.1.1), further dissipation of energy and angular momentum can lead the core to become gravitationally unstable. The core quickly collapses ($\sim 10^6$ yr)[1] under its own gravity and forms one or more protostars (phase 2). Let us assume that only one protostar forms. The central object enters its accretion phase, where material is moving from the infalling envelope and through the accretion disk that is formed due to the conservation of then angular momentum of the whole cloud. At this stage, the redistribution of angular momentum, from the envelope to the disk and from the inner edge of the disk to the star surface, produces the generation of outflows and bipolar jets. These mechanisms are responsible for ejecting a fraction of the accreted material and are usually oriented perpendicular to the disk plane (phase 3).
In the following stage (phase 4), between 1<t<10 Myr, material from the circumstellar disk is transported inward to the vicinity of ~ 0.1 au (Hartmann et al., 2016). Inside this region, the disk temperature increases due to heating by the radiation field on the central object, and the dust begins to sublimate; at this radius, the inner edge of this dust wall

---

[1] This is the fastest timescale on which the cloud would collapse if there was nothing to resist collapse against gravity.

re-radiates the energy it absorbs, which is observed as a near-IR excesses. This stage of continuous accretion of material from the circumstellar disk is also referred to as pre-main sequence star (PMS).
Then the object enters in the last phase (age of the order of 10 Myr, or more), where the more evolved PMS reaches its final mass, is surrounded by planets or by a debris disk and evolves towards the main sequence.

1.2 Young stellar objects classification

The classification of young stellar objects (YSO) was first established by Lada & Wilking (1984). They identified three different groups in the Ophiuchus star forming region, based on whether the emitted energy was increased in the mid-infrared or declined but presented either a tenuous or a notable infrared excess over the blackbody stellar photosphere. These three different spectral energy distribution (SED) slopes in the IR (Lada, 1987),

$$\alpha_{IR} = \frac{d\log\nu\, F_\nu}{d\log\nu} = \frac{d\log\lambda\, F_\lambda}{d\log\lambda}\,, \tag{1.1}$$

were used to classify Class I, Class II and Class III YSOs, which can be interpreted in terms of an evolutionary sequence, see Fig.1.1. Class I YSOs are typically visible in the near IR, but are generally optically obscured. In terms of mass, $M_{star} > M_{env} \sim M_{disk}$, and usually their IR slope is larger than 0.3. By the end of the Class I phase the envelope has completely dispersed. Class II YSOs are optically visible and they are characterized by a typical “IR-excess” emission, which is due to reprocessing of radiation from circumstellar dust. Disk masses at the Class II stage are a small fraction of the central stellar mass, $\sim 1\%$, while $M_{env} \sim 0$. The disk in this stage can be considered truly protoplanetary, not protostellar. Usually their SED slopes are between $-1.6 < \alpha_{IR} < -0.3$. Class III YSOs are also optically visible but they do not show any IR-excess as the previous stage. The ratio between the disk and stellar mass is even more dramatic $\ll 1\,\%$, and their IR slopes are lower than -1.6. Additionally, Greene et al. (1994) introduced an intermediate phase between Class I and II YSOs, called "flat spectrum sources", which was shown to be in agreement with the theoretical studies of a rotating, collapsing core by Adams et al. (1987). At the same period, André et al. (1993) introduced a stage even less evolved than the previous phases, Class 0 YSOs, using sub-millimeter continuum observations in the ρ Ophiuchi A cloud. These extremely young objects were characterized by cold temperatures $< 20\,\mathrm{K}$, high internal obscuration and very low values of bolometric luminosities, $L_{bol} \lesssim 1\,\mathrm{L}_\odot$.
Later on, a millimeter survey of 100 YSOs at ρ Ophiuchi molecular cloud with the IRAM 30 m telescope (André & Montmerle, 1994), revealed the presence of unresolved disks around Class II sources and resolved, extended envelopes around Class I sources. Moreover, it was confirmed that the envelopes of Class I sources contain more circumstellar material than Class II disks, in consistence with Class I sources being younger than Class II sources.

The gas and dust budget around young protostars plays a fundamental role in the process

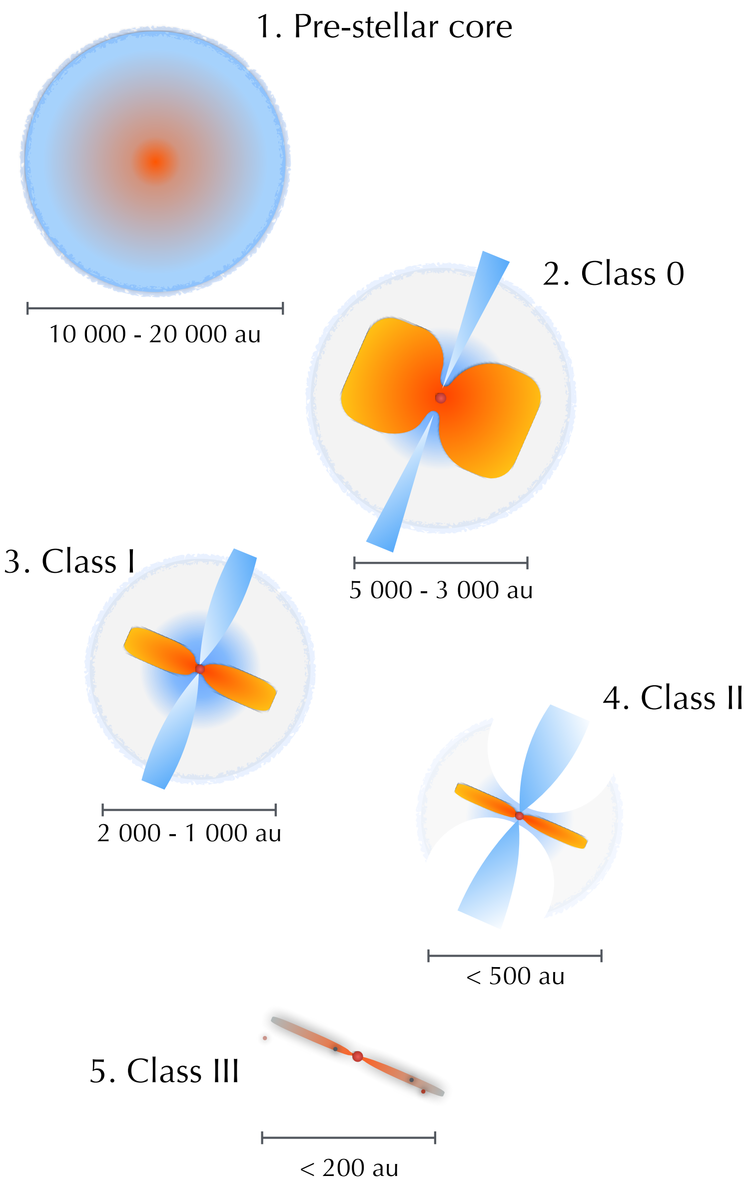

Figure 1.1: Schematic representation of the evolution of a low mass pre-stellar core into a Class III object. The numerical sequence indicate the phase.

of planet formation, since these are the ingredients from which planets will form.
This thesis will focus on the Class I stage, where millimeter observations from different interferometers arrays (SMA, NOEMA and ALMA) will shed light on a wide variety of topics, from dusty envelope characterization to how the dust grows in these components.
In the following sections an introduction to the dust emission, evolution and properties

are presented. These information are needed to understand the studies presented in the following chapters.

1.3 Grain growth: from ISM dust to planets

Dust represents 1% of the initial mass of protoplaneary disks and the only solid source material to form terrestrial planets and the cores of the giant planets.
In the diffuse interstellar medium (ISM), the dust grain sizes are of the order of $0.1\,\mu$m and mainly composed by silicates and a mixture of graphite grains and polycyclic aromatic hydrocarbons (Draine, 2003).
In the standard scenario of planet formation, these microscopic dust grains progressively grow following different mechanisms in order to cover the almost 13 orders of magnitude in linear size that separate sub-micron particles from terrestrial planets. See Figure 1.2.
In the very first step, aerodynamic forces maintain the sub-μm sized grains well coupled to the gas content in the disk. At this point, grains grow in size by coagulation (sticking after collisions with other grains), by van der Waals short interactions (Heim et al., 1999). While grains stick to each other, their surface-to-mass ratio decreases, they eventually decouple from the gas. Larger grains begin to move toward the mid-plane due vertical settling. This process accelerates grain growth and result in millimeter or even larger grains settling deeper into the disk. If the sticking probability is near unity, then the growth become exponential and only ceases when the particles reach the mid-plane as pebbles. The second phase of the core accretion model requires that cm-and-m-size grains grow up to bodies with 1-100 km radius. These planetesimals are the last stage of solid growth that may be directly observable before the formation of large, planetary-size bodies (Sallum et al., 2015; Isella et al., 2019). Their orbital evolution is dominated by gravitational interactions rather than by interaction with the gaseous disks but, the process through which planetesimals form is still unclear. There is a consensus that coagulation is not sufficient to form bodies larger than about a meter. The presence of gas affects the relative velocities of the dust grains. The different orbital rates between gas (sub-Keplerian velocity) and dust (Keplerian velocity) result in headwind and/or tailwind removing or adding angular momentum to the particles orbit. As a consequence, particles drift radially towards the star or close to local pressure maximum on times scales as short as 100 years per au (Weidenschilling, 1977).

Overcoming the problem known as the “meter-size barrier” is one of the biggest challenges for planet formation theories (Chiang & Youdin, 2010), but several possible solutions have been proposed. Vortices have the ability to sequester particles, with typical radii $\sim 1\,$mm to $\sim 10\,$cm, that are slightly decoupled from the gas. Vortex capture occurs on dynamical time-scales shorter than the time-scale of radial drift, $t_{drift} \sim 10^2\,\mathrm{yr}\,(\mathrm{r/au})$, therefore provide a way to trap these particles and to grow into larger ones ($\sim$ m to km) before they drift into the star (Heng & Kenyon, 2010). Another alternative for trapping particles within the disk are streaming instabilities, defined as the clumping of particles in a gaseous disk with pressure support (e.g. Goodman & Pindor 2000). For example, Youdin & Shu (2002) suggested that gravitational instabilities can concentrate millimeters-sized chondrules[2] in a gas-deficient disk in a few $\times\,10^6$ yr, which is consistent with the timescales of the dust disappearance around T Tauri stars. Other possibility for grain growth is in pressure traps. Pinilla et al. (2012) suggest that the presence of pressure bumps with width-sizes of the order of the disk scale-height and an amplitude of 30% of the gas surface density of the disk, provide the conditions for the dust to grow and to survive within the disk.

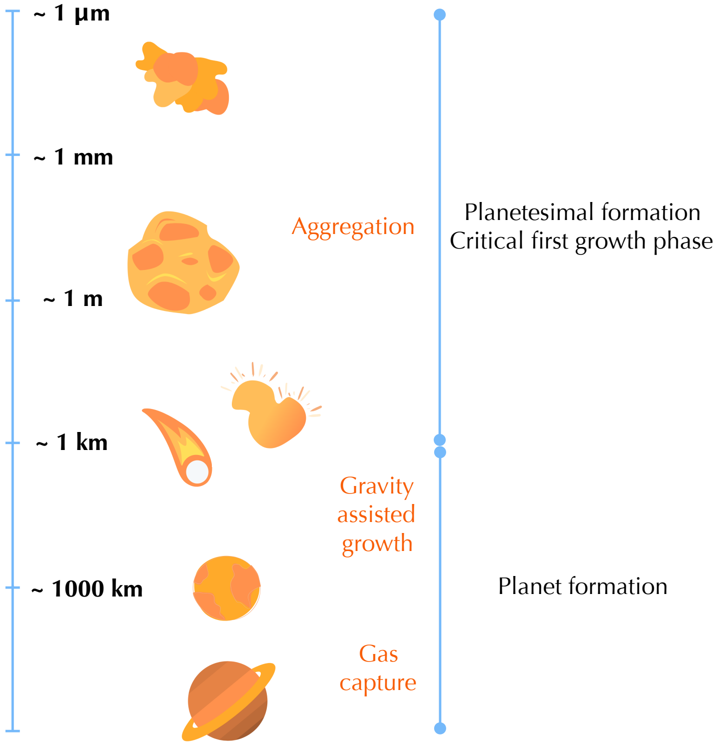

Figure 1.2: Summary of the core accretion model for planet formation. Planet formation starts with the coagulation of μm-sized grains to form solids up to $\sim 1\,$m, but further growth needs alternative mechanisms in which turbulence and gravity play fundamental roles. The planetary core is built from the planetesimals, bodies of 1-100 km in radius, through gravity-assisted two-body inelastic encounters. If the protoplanet core is of the order of $10\,\mathrm{M}_\oplus$, then a rapid gas accretion is triggered and a gaseous planet is formed. If the protoplanet has a lower core mass then a terrestrial planet with a rocky core and a tenuous atmosphere is formed. Sketch adapted from C. Dullemond lectures.

---

[2] Chondrules are typically millimeter sized particles found in meteorites with near-solar compositions unaltered by heating processes.

1.3.1 Observational evidence: From sub-micron to microns

As mentioned above, the ISM dust is composed by a mixture of materials. This includes solid carbon, for example, in the form of polycyclic aromatic hydrocarbons (PAHs), graphite, nanodiamonds, or in the form of complex organic compounds. Another major constituent of interstellar dust is amorphous silicates, where olivine and pyroxene are the most common. These silicates have features at 9.7 and 18.5 μm from SiO stretching and OSiO bending modes, that are very sensitive to the particle shape and size, which are typically in the range of r $\sim$ 0.1-5 μm.

In the last decades surveys, as those with the *Spitzer* space telescope, have revealed silicate features in many disks and in different star-forming regions (e.g. Furlan et al. 2006; McClure et al. 2010; Oliveira et al. 2010). These observations trace the warm upper layers of the disk, which are consistent with the presence of micron-sized particles and the absence of sub-micron dust grains. This implies either that grain growth is more efficient than fragmentation at these scales or that sub-micron grains are efficiently removed from the atmosphere of the disk via stellar winds or radiation pressure (Olofsson et al., 2009).

Even though many studies have searched for a correlation between disk properties and grain characteristics (sizes, shape), no conclusive evidence has yet been found. Infrared observations have been very important to probe the properties of the thin surface layers of the disk, but their strong dependency on the central star parameters, for example the spectral type of the star, makes it difficult to use spatially unresolved spectroscopy as a probe of global dust growth in disks. Nevertheless, most of these studies revealed that the dust producing these IR features contains a prominent fraction of crystalline material, indicating that the dust has been heated to temperatures of around 1000 K during the disk formation. This were detected by Ábrahám et al. (2009) and Juhász et al. (2012) suggesting that eruptive phenomena in young disks play a fundamental role in the processing and mixing of dust in protoplanetary disks.

1.3.2 Observational evidence: From microns to mm-sizes

Another independent evidence of grain growth in the early stages of star formation is found in the slope of the SED at sub-millimeter wavelengths, $\alpha_{\rm mm}$,, where dust emission is optically thin and the flux relates to the frequency as $F_\nu \propto \nu^{\alpha_{\rm mm}}$.

Weintraub et al. (1989); Woody et al. (1989); Adams et al. (1990); Beckwith & Sargent (1991) provided the first single-dish and interferometric observations that measured the sub-mm slope of the SED of young disks. These works revealed that the mm-slope is shallow in protoplanetary disks, $\alpha_{\rm mm} \approx 2$–3 and different from the typical values of the ISM, $\alpha_{\rm mm} \sim 4$ (Boulanger et al., 1996). If emission is optically thin then the SED shape (slope) reflects the spectral shape (slope) of the opacity. A common prescription for the dust opacity in disks at millimeter wavelengths is given by Beckwith et al. (1990):

$$\kappa_\nu = 0.1 \left(\frac{\nu}{10^{12}\,\rm Hz}\right)^\beta \,\rm cm^2\,g^{-1} \tag{1.2}$$

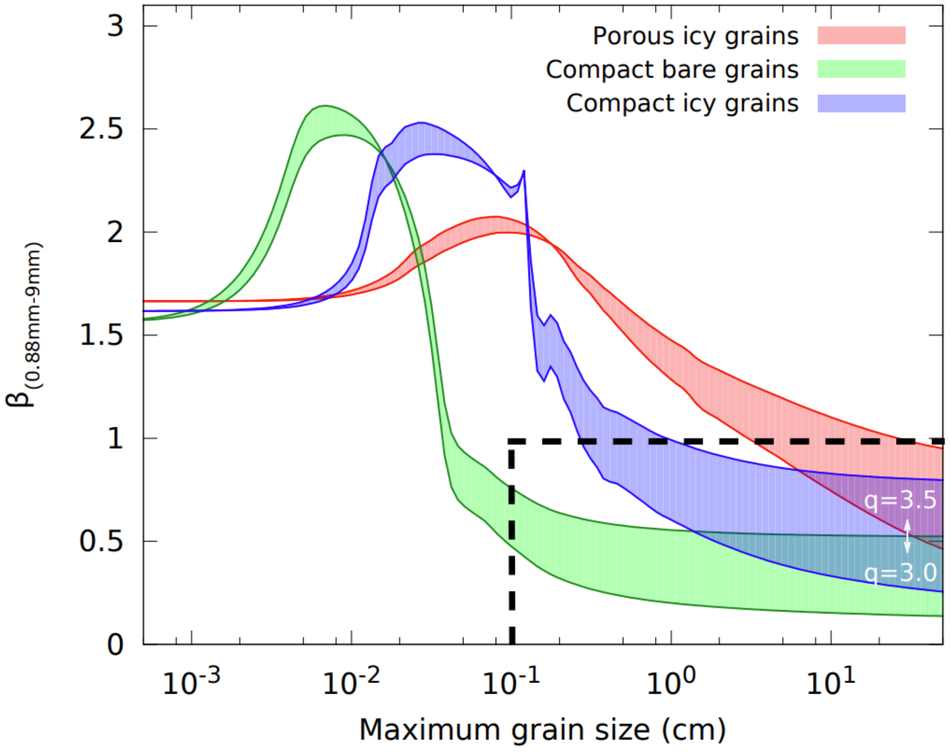

Figure 1.3: Spectral index β of the dust opacity calculated between the wavelengths of 0.88 mm and 9 mm as a function of the maximum grain size, for a grain size distribution $n(a) \propto a^{-p}$ characterized by a minimum grain size of 0.01 μm. The red line shows grains composed of astronomical silicates, carbonaceous material, and water ice, with relative abundances as in Pollack et al. (1994) and a porosity of 50%. The blue line represent compact grains with the same composition as above and in green are compact grains composed only of astronomical silicates and carbonaceous material. For each composition, the colored region shows how the slope $q = 3.0$ to $q = 3.5$ change the values of β. Despite the dependence of β on the grain composition and the value of q, maximum grain sizes larger than about 1 mm lead to values of β less than unity (black dashed lines). These opacities have been computed following the prescription in Natta & Testi (2004). Credit: Testi et al., 2014

where κ and the dust opacity index, β, are related to the size distribution and composition of the dust grains (Ossenkopf & Henning, 1994; Pollack et al., 1994). The normalization implicitly includes a gas-to-dust mass ratio of 100. The SED slope in the optically thin case relates to the β as, $\alpha_{\rm mm} = 2 + \beta$.

The possible explanation for the disks showing $\alpha_{\rm mm} \approx 2$–3 (or $\beta_{\rm mm} < 1$), is the presence of dust grains with sizes larger than ISM dust. The dust opacity spectral index β also depends on other factors, such as dust chemical composition, porosity, geometry, as well as on the the grain size distribution. Typically a power law distribution is assumed, $n(a) \propto a^{-q}$ (e.g. D'Alessio et al. 2001), characterized by a minimum grain size of $0.01\,\mu$m. An important conclusion from the dust models in Natta & Testi (2004) is that $\beta \approx 1.7$ when the maximum grain size is lower than $30\,\mu$m, while dust grains with sizes of the order of 1 mm or larger lead to β values lower than 1, using a grain size distribution slope of $q = 2.5$–3.5, see Figure 1.3.

Multiple efforts, that include models of dust evolution and the exploration of the submillimeter spectral index β, have been made to explain the dust grain growth. D'Alessio et al. (2006) explored the effect of changing the slope of the grain size distribution to $q = 2.5$. As a result, the dust opacity coefficient κ at 1 mm changes nearly 2 orders of magnitude from a dust population with $\beta \approx 0.2$ to $\beta \approx 1.0$–1.5.

Similar results on β and radial variation of grain growth are obtained with mm-observation on disks in different star forming regions (e.g. Ricci et al. 2010b; Pérez et al. 2015; Tazzari et al. 2016a).

There is also evidence that grain growth may start in earlier stages or before the disk formation. Pagani et al. (2011) showed evidence of grain growth already within dense core phase up to $\sim 1\,\mu$m, inferred from "coreshine". This IR emission is produced by strong scattering of background radiation due to μm-sized grains within the core. The multi-wavelength observations in Jørgensen et al. 2007; Kwon et al. 2009; Chiang et al. 2012a find $\beta \sim 1$ in Class 0 protostars, pointing to the presence of large (mm-size) grains.

These studies only place a lower bound on the size of the most massive grains, but cm-wavelength observations constrain the presence of larger grains. At longer wavelengths the flux decreases, therefore, the surface area of the dust decreases for a given mass and the free-free emission from an ionized stellar wind often dominates for wavelengths larger than 1 cm (Natta & Testi, 2004). The survey by Rodmann et al. (2006) in Taurus-auriga pre-main-sequence disks at 7 mm revealed that, after accounting for contributions from free-free emission and corrections for optical depth, β changes between 0.5 to 1.6, which suggests that mm-sized dust aggregates are present in circumstellar disks. Similar results are found in other regions observed at longer wavelengths (Cortes et al., 2009; Lommen et al., 2009; Banzatti et al., 2011; Pérez et al., 2012; Ubach et al., 2012). The implication is that centimeter sized particles are commonplace.

Even though the evidence of grain growth in evolved disks is very strong, its presence in earlier phases is still under debate. New mm-observations with better resolution and sensitivity have contradicted previous evidence of grain growth (Sadavoy et al., 2016). In the case of Class 0 protostars, the conclusions about dust disk properties are highly affected by the presence of significant accretion of material from the envelope and mass loss via jets (e.g. Evans et al. (2015)). Thus, large uncertainties affect measurements of the dust spectral index β toward Class 0 sources. Class I protostars represent a stage where the surrounding envelope is less massive, and allow for a cleaner analysis of the dust properties than in Class 0 sources because it is possible to separate the emission into disk and envelope components. Only a few Class I protostars have been studied to constrain the dust properties and this will be discussed in the following section.

1.3.3 Measuring dust grain sizes in Class I protostars

Class I YSOs are generally interpreted as protostars with typical ages of 0.1–0.2 Myr (Greene et al., 1994) surrounded by an accretion disk and embedded in a low-mass circumstellar envelope that is being rapidly dissipated. As mentioned before, only a few Class I protostars have been observed and modeled in order to study their dust properties. Miotello et al. (2014) found grains grown up to mm-size in the envelope of two Class I sources, Elias 29 and WL 12, obtaining values of β_{env} ∼0.6–0.8. These values are compatible with the suggestion by Chiang et al. (2012b) for Class 0s. This evidence may carry important information about the formation of large solids in protostars.

As we previously explained, grain growth is a very difficult process, and at envelope scales, there is no high enough density or sufficient time to allow for an efficient grain growth (Ormel et al., 2009). The confirmation of mm-size pebbles already in the envelope of Class I protostars questions the current knowledge on the grain growth process. While in Miotello et al. (2014) the dust grain size is constrained using dual-mm-wavelengths observations and radiative transfer models (cover in the next sections), the study by Sheehan & Eisner (2017) used another modeling approach: they combined 1.3 mm observations + SED data and a radiative transfer model. This work covers a sample of 10 Class I protostars in the Taurus molecular cloud, finding $\beta < 1.1$, in all the sources. Additionally, a median disk mass of 0.018 $M_{\odot}$ on average is found. This is more massive than the Taurus Class II disks, which have a median disk mass of ∼0.0025 $M_{\odot}$. The decrease in disk mass can be explained if dust grains have grown by a factor of 75 in size, indicating that by the Class II stage a significant amount of dust grain processing has taken place. However, extending the observations to longer mm-wavelengths is needed to really constrain the level of growth in the disk and the envelope of Class I protostars.

1.4 Interferometry

The first modern interferometric observation, using the Fizeau interferometer technique for measuring the shape of an optical surface, was made by Michelson & Pease (1921). They observed the angular size of the photosphere of the massive star Betelgeuse.

This section introduces the concept of interferometry, and describes the basic aspects of interferometric observations at sub-millimeter wavelengths.

Interferometry offers many advantages over using single dish telescopes. One of the most important is their spatial resolving power.

One of largest single dish telescopes has diameter, D, of 100 m and its angular resolution is diffraction limited to θ=1.2 λ/D. Assuming that the telescope is operating at a wavelength of λ=1 mm, we can use the Rayleigh criterion to define the highest angular resolution achievable for the telescope, which is 2.5 arcsec. If we seek to observe a typical circumstelar disk, assuming a diameter of 100 au (Andrews & Williams, 2007) at a distance of 100 pc, this translates into 1 arcsec angular size in the sky. If a high resolution observation is needed, for example to resolve features of 10 au (0.1 arcsec), a single dish telescope of 2500 meters would be required. This is 25 times larger than the 100 m single dish in Arecibo Observatory.

Thus, aperture-synthesis interferometers must be used in order to access smaller angular scales and to mitigate other problems related to single dishes, such as: vulnerability to fluctuations in atmospheric emission and receiver gain[3], radio-frequency interference[4], and pointing shifts caused by atmospheric refraction.

Multiple smaller dishes or antennas can be combined together in an array to simulate a larger telescope, an interferometer. The resolution of an individual telescope is given by their size, the larger the mirror, the larger collecting area and field of view. But this is not the case for an interferometer: instead of the telescope size it is the spacing between the telescopes, also known as the baseline length. To understand this, in the following section we provide a detailed account on how two-telescope interferometer work.

1.4.1 Two-Element Interferometer

The simplest radio interferometer is a pair of radio telescopes whose voltage outputs are correlated (multiplied and averaged). Even the most elaborate interferometers with $N \geqslant 2$ antennas, can be treated as $N(N-1)/2$ independent two-element interferometers.

Figure 1.4 shows two identical dishes separated by the baseline B. The two antennas point in the same direction, s, and θ is the angle between B and s. If a wave-front is coming from distant point source (orange arrows in Fig.1.4), the wave have to travel an extra distance, B·s, to reach the left antenna, so the output voltage v_1 of the left antenna is the same as the output v_2 of the right antenna, but with a difference in time given by the geometric delay $t_g = \mathrm{B}\cdot \mathrm{s}/\mathrm{c}$, where c is the speed of light. For simplicity, we consider a quasi-monochromatic interferometer that responds only to radiation in a very narrow band $\Delta\nu \ll 2\pi/t_g$ centered on a frequency $\nu = \omega/2\pi$, where ω is the angular frequency. Then the output voltages of antennas 1 and 2 at time t can be written as:

$$v_1 = vcos[\omega(t - t_g)] \qquad \text{and} \qquad v_2 = vcos(\omega t) \tag{1.3}$$

These voltages are amplified, multiplied and time averaged by the correlator to yield an output response whose amplitude R is proportional to the flux density of the point source and whose phase $(\omega\, t_g)$ depends on the delay and the frequency as follows

$$R = \left(\frac{v^2}{2}\right) cos(\omega t_g). \tag{1.4}$$

The correlator output amplitude $v^2/2$ is proportional to the flux density of the point source multiplied by $\sqrt{A_1 A_2}$, where A_1 and A_2 are the effective collecting areas of the two antennas. Notice that the correlator output voltage R, varies sinusoidally as the Earth's

---

[3] Receiver gain changes, erratic fluctuations in atmospheric emission, or confusion by the unresolved background of continuum radio sources usually limit the sensitivity of single-dish continuum observations.

[4] Radio frequency interference (RFI) mainly affects low frequency observations. Radiation from the Sun and artificial sources of RFI far from the observing direction will be mixed with the desired signal.

rotation changes the source direction relative to the baseline vector. These variations are called fringes, and the fringe phase

$$\phi = \omega t_g = \frac{\omega}{c}\, B\, cos\theta \tag{1.5}$$

depends on θ as follows:

$$\frac{d\phi}{d\theta} = \frac{\omega}{c}\, B\, sin\theta = 2\pi \left(\frac{B\, sin\theta}{\lambda}\right) \tag{1.6}$$

The fringe period $\Delta\phi = 2\pi$ corresponds to an angular shift $\Delta\theta = \lambda/(\mathrm{B}\sin\theta)$. The fringe phase is an exquisitely sensitive measure of source position if the projected baseline $\mathrm{B}\sin\theta$ is many wavelengths long. Additionally, the angular shift $\Delta\theta$ of the fringes is analogous to the resolution that the baseline pair is sensitive to. Therefore, an increase in baseline B leads to smaller angular scales, and thus the limiting factor that determines the angular resolution of an interferometer is not the size of the individual antenna, but rather the maximum baseline between the elements.

By using multiple antennas forming many different baseline pairs of varied lengths in an interferometric array we can obtain signals on a range of angular scales, and combine these signals to build up an image. However, because the antenna diameters D must be smaller than the baseline B (else the antennas would overlap), the angular frequency response cannot extend to zero and the interferometer cannot detect an isotropic source. Consequently, in order to recover emission from the largest scales that are filtered out by the interferometer, supplementary observations are required. The missing short spacings (B<D) can be provided by a single-dish telescope.

The following section will cover the main relationships behind the method of interferometry. This will provide a sound basis for the understanding of observations presented in further chapters.

1.4.2 The (u,v) plane

Each projected baseline (i.e. the baseline as seen from the source) traces out an ellipse with one antenna at the centre of the ellipse, and it can be specified using u-v coordinates: u gives the east-west component of the baseline. v gives the north-south component of the baseline. The projected baseline is given by, $\mathrm{B}\sin\theta = (u^2 + v^2)^{1/2}$. Placing measurements in the (u, v) plane is the standard method used to arrange the response of the interferometer.

1.4.3 The visibility

Observations using interferometers cannot directly measure the brightness across certain targets. Instead, interferometers measure the coherence of signals received by each antenna in the array. The visibility has two parts: amplitude and phase. The visibility amplitude

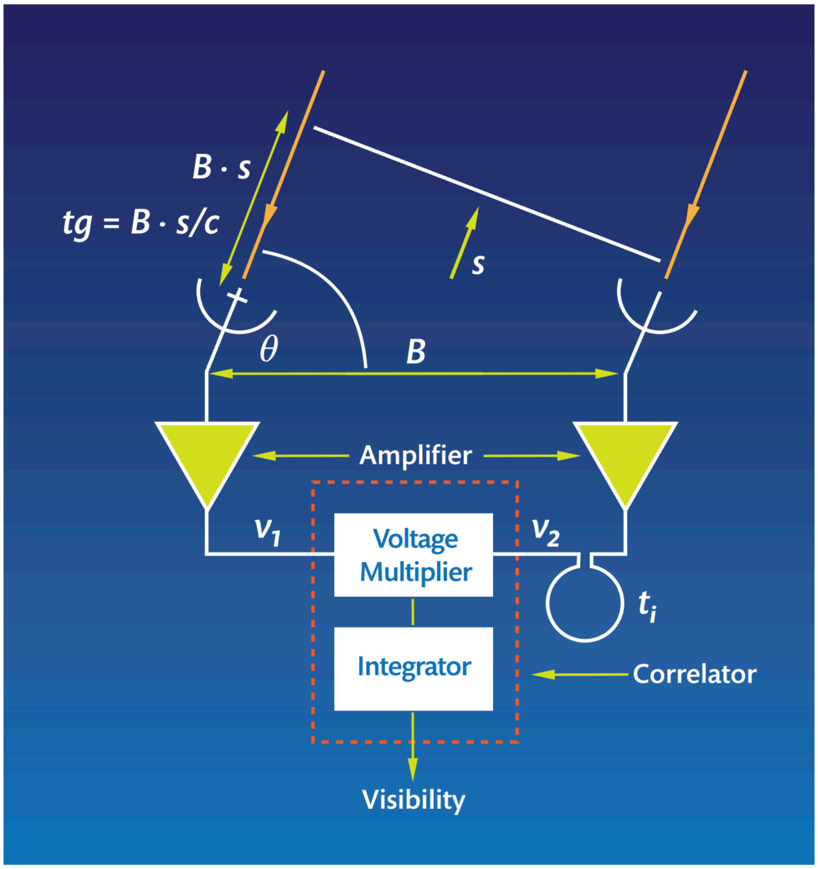

Figure 1.4: Scheme of a two element interferometer. This consists of individual antennas whose size D is small compared to their separation B (baseline), projected in the direction of the source. In this illustration, the inputs are amplified at each element then combined in the Voltage Multiplier. The result is the visibility, that is, the response of the instrument, as a function of the baseline. The output is summed over a short time in the Integrator. The time delay, t_i, is adjusted electronically in order to the waves reach the voltage multiplier aligned, therefore, in phase. (Credit: ALMA Newsletter n° 5.)

encodes source shape and flux density, while visibility phase encodes source position. In general, the visibility is usually expressed as a complex quantity given by

$$V = |V|e^{-i\phi}, \tag{1.7}$$

where V is known as the complex visibility, $|V|$ is the amplitude, and ϕ the phase. The visibility measured by the interferometer in baseline coordinates (u, v), can be related, to the sky brightness distribution in (x, y) coordinates with the spatial coherence function,

$$V(u, v) = \int\int I(x, y)\, e^{-2\pi i(ux+vy)} dx\, dy. \tag{1.8}$$

Then, the brightness distribution of a source is simply the two-dimensional Fourier transform of the measured visibilities, known as the van Cittert-Zernike theorem (van Cittert, 1934; Zernike, 1938).

$$I(x,y) = \int\int V(u,v)\, e^{2\pi i(ux+vy)} du\, dv \tag{1.9}$$

With the visibility amplitude it is possible to understand the structure of the source. For instance, the plot of the de-projected baseline b_{uv}, which is given by the addition in quadrature of u and v, $b_{uv} = \sqrt{u^2+v^2}$ versus amplitude, it will produces different visibility curves depending of their spatial distribution of emission. In Figure 1.5 examples with various brightness distributions are shown.

1.4.4 Aperture synthesis

V(u,v) can be measured on a discrete number of points. A good image quality requires a good coverage of the uv-plane. For this purpose, the Earth rotation is used to increase the uv-coverage. The first description and use of this technique was performed in the late 1960s involving the first observations of pulsars by Jocelyn Bell Burnell and Antony Hewish using the Interplanetary Scintillation Array at the Mullard Radio Astronomy Observatory (Hewish et al., 1968). To explain the technique, Fig. 1.6 shows two examples of uv-coverage obtained from the SubMillimeter Array (SMA) facility in the extended configuration, where the maximum distance between antennas is approximately 212 meters. The first example (left) shows the uv-coverage obtained after observing a source for ∼36 minutes. The second example (right) shows the uv-coverage obtained using the same antenna configuration, but after observing the target for 5.9 hours. Each visibility point corresponds to an effective integration time of 1.0 minute, and over time these begin to trace smooth arcs in uv-space, as the array moves with respect to the target due to the rotation of the Earth.

However, even tracking a source from rising to setting, there will still be gaps in the sampling. In order to fill these gaps, the antenna configuration can be changed, allowing previously unsampled uv-space to be covered.

1.4.5 Deconvolution basics

All deconvolution methods supply missing information. In practice, the full uv-space can never be completely recovered, and what is actually recovered is known as the dirty image, I^D, which by using the van Cittert-Zernike theorem can be described by

$$I^D(x,y) = FT^{-1}\, S(u,v)\ \times\ V(u,v), \tag{1.10}$$

where S(u,v) is the sampling function consisted of series of delta functions, which are unity in the sampled regions of uv-space and zero elsewhere. FT^{-1} is the inverse Fourier transform. The dirty image can be described as a convolution, ⊗, following:

$$I^D(x,y) = b(x,y) \otimes I(x,y), \tag{1.11}$$

where $b(x,y)$=$FT^{-1}\, S(u,v)$ is known as the dirty beam or the point spread function analog of a conventional telescope. Therefore, recovering the true intensity of the source, I(x,y),

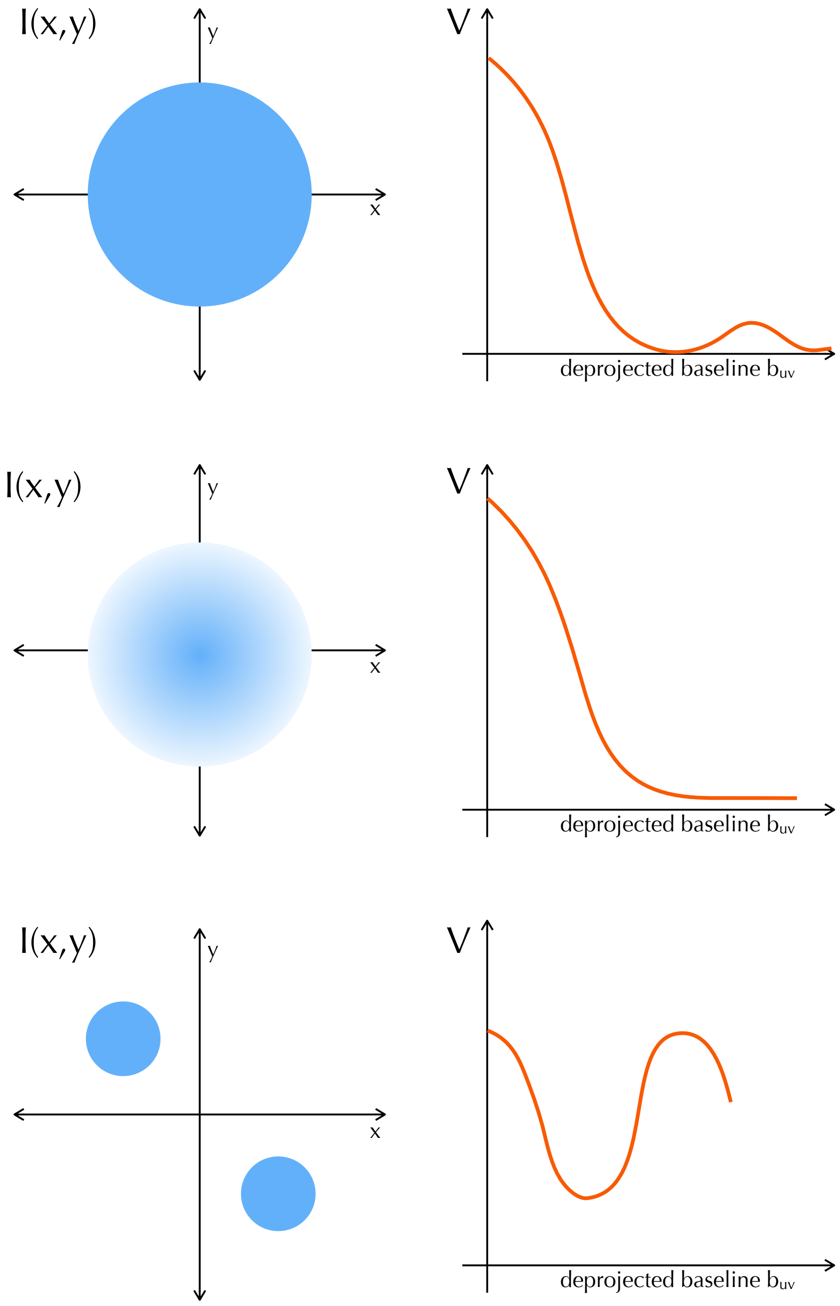

Figure 1.5: Visibility as a function of baseline for three examples of brightness distributions. Top: A uniform disk geometry produces a sinc-like function in visibility, due to the sharp edge of the disk. Middle: A Gaussian disk geometry produces a smoothly declining visibility curve. Bottom: A binary source produces a sinusoidal-like visibility curve. Adapted from EPJ Web of Conferences 102.

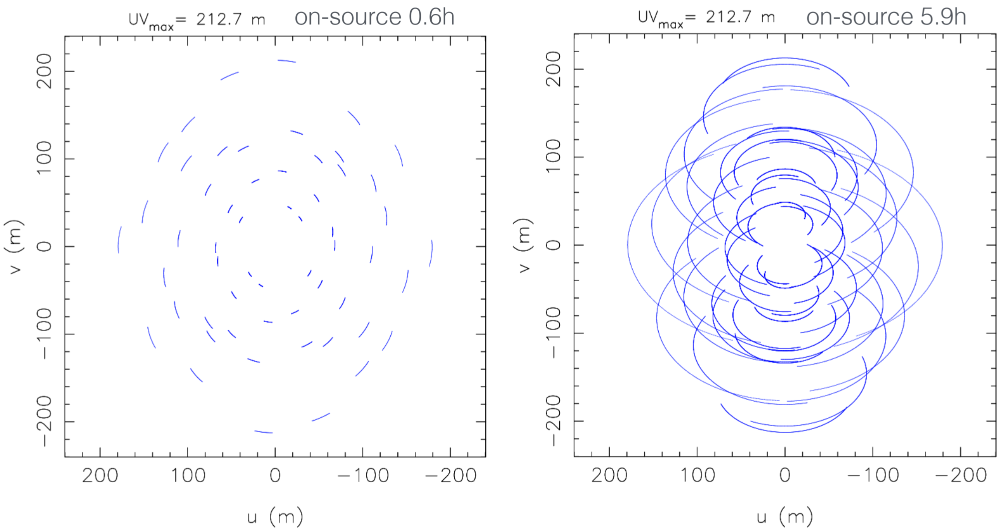

Figure 1.6: Examples of the uv-plane coverage for the Sub-Millimeter Array (SMA). Left: Example of a relatively sparsely sampled uv-plane, wit a time on-source of 36 minutes. Right: Example of a more complete uv-coverage, carried on over 5.9 hours, due to the rotation of the Earth.
Credit: SMA Beam Calculator & Sensitivity Estimator.

involves removing of the dirty beam $b(x, y)$ contribution from the dirty image, $I^D(x, y)$. The most successful deconvolution procedure is the CLEAN (Högbom, 1974) algorithm.

1.4.6 Visibility Weights

For optimal imaging performance, it is critical that each visibility in the data have the correct weight after calibration. Data with better sensitivity have more weight than data with less sensitivity. Formally, the post-calibration visibility weights should be equal to $1/\sigma_{ij}^2$ where σ_{ij} is the rms noise of a given visibility, i.e.

$$\sigma_{ij}(Jy) = \frac{2k}{\eta_q \eta c A_{eff}} \sqrt{\frac{T_{sys,i}\,T_{sys,j}}{2\Delta\nu_{ch} t_{ij}}} \times 10^{26} \tag{1.12}$$

where, k is Boltzmann's constant. A_{eff} is the effective antenna area which is equal to the aperture efficiency $(\eta_a)\times$ the geometric area of the antenna $(\pi\, r^2)$. The aperture efficiency depends on the rms antenna surface accuracy. For example, for an ALMA dish that is about 0.75. η_q and η_c are the quantization and correlator efficiencies, respectively. For ALMA, these values are 0.88 and 0.96, respectively. $T_{sys,i}$, $T_{sys,j}$ are the system temperature for an antenna pair. $\Delta\nu_{ch}$ is the effective channel frequency width and t_{ij} is the integration time per visibility.

1.4.7 Current facilities

Over the past decades, there has been much investment in the development and commissioning of a new generation of long wavelength interferometric facilities. This thesis is based on observations carried out in four important facilities that are described below and compared in Table 1.1.

SMA

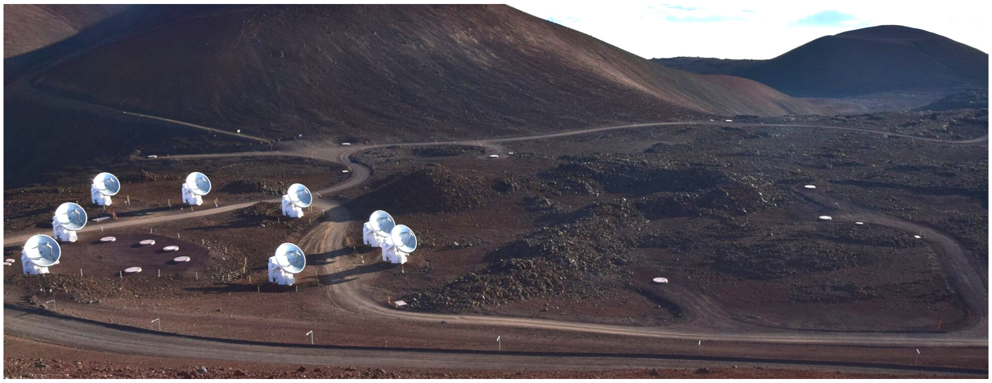

Figure 1.7: The eight antennas of the Submillimiter Array (SMA). Photo taken by the author.

The Submillimeter Array (SMA) is an 8-element radio interferometer located near the summit of Mauna Kea in Hawaii (see Fig. 1.7). The array operates at frequencies from 180 GHz to 420 GHz. The 6 m diameter dishes may be arranged into configurations with baselines long as 509 m, producing a synthesized beam of sub-arcsecond width. Each element can observe with two receivers simultaneously, with up to 8 GHz bandwidth in each sideband.
SMA now offers up to 32 GHz of processed bandwidth, which can be configured for 32 GHz of instantaneous on sky frequency coverage or 16 GHz of frequency coverage with dual polarization.

NOEMA

The NOrthern Extended Millimeter Array (NOEMA) is located in the South of the French Alps, near St Etienne in Dévoluy in the Départment Hautes Alpes (see Fig. 1.8). The interferometer is located at 2560 m altitude and comprises of ten 15 m diameter antennas with a maximum baseline of 760 m. The antennas are equipped with three receiver bands, observing in dual polarization and two sidebands in the 3, 2, 1 mm atmospheric windows. The ten antennas of the interferometer can be positioned on 32 stations along a “T” shaped track. The north-south arm is 368 m long, and the east-west oriented arm extends 216 m west and 544 m east of the intersection. The angle between the arms is 75°. The wide-band correlator, *PolyFiX*, in its low spectral resolution mode with a 2 MHz channel spacing, can

Figure 1.8: NOEMA (NOrthern Extended Millimeter Array). Ten of the future twelve 15-meter dishes. Credit: IRAM.

process a total instantaneous bandwidth of ∼31GHz for up to twelve antennas. The 31 GHz are thereby split up over the two sidebands and two polarisations.

VLA

Figure 1.9: The Very Large Array (VLA) is a collection of 27 radio antennas located at the NRAO site in Socorro, New Mexico. Credit: Alex Savello.

The Karl G. Jansky Very Large Array (VLA) is a 27–element interferometric array (see Fig. 1.9), arranged in a "Y" shape, which produces images of the radio sky at a wide range of frequencies and resolutions. The VLA is located at an elevation of 2100 meters on the Plains of San Agustin in southwestern New Mexico, and is managed from the Pete V. Domenici Science Operations Center (DSOC) in Socorro, New Mexico. The VLA can vary its resolution over a range exceeding a factor of ∼50 through movement of its component antennas, which have 25 m in diameter. There are four configurations, A, B, C and D. The A-configuration provides the longest baselines (36.4 km) and thus the highest angular resolution, but yields very limited sensitivity to surface brightness. The D-configuration provides the shortest baselines (1.03 km), translating to a high surface brightness sensitivity at the cost of angular resolution. All VLA antennas are outfitted with eight receivers providing continuous frequency coverage from 1 to 50 GHz. These receivers cover the frequency ranges of 12 GHz (L-band), 24 GHz (S-band), 48 GHz (C-band), 812 GHz (X-band), 1218 GHz (Ku-band), 1826.5 GHz (K-band), 26.540 GHz (Ka-band), and 4050 GHz (Q-band).

ALMA

Figure 1.10: 66 ALMA antennas installed in a clear compact configuration. In the background is the Licancabur Volcano and on the far right is Chajnantor hill. Credit: ALMA (ESO/NAOJ/NRAO)

The Atacama Large Millimeter/submillimeter Array (ALMA) is an interferometer located on the Chajnantor Plateau in the Atacama Desert in Chile (see Fig. 1.10). ALMA consists of a giant array of 12 m antennas with baselines up to 16 km, and an additional compact array of 7 m and 12 m antennas to image extended targets. Located at 5000 m altitude, the antennas can be placed in different locations on the plateau in order to form arrays with different distributions of baseline lengths. The frequency range available to ALMA is divided into different receiver bands. These bands range from band 3, starting at 84 GHz, to band 10, ending at ∼950 GHz. ALMA can deliver data cubes with up to 7680 frequency channels (spectral resolution elements). The width of these channels can range between 3.8 kHz and 15.6 MHz, but the total bandwidth cannot exceed 8 GHz.

Table 1.1: Examples of current interferometric facilities

Array	Location	Antennas	Maximum baseline (m)	Frequencies (GHz)
SMA	USA	8	519	180–418
NOEMA	France	10	760	82–264
VLA	USA	27	36400	1–50
ALMA	Chile	66	16000	84–950

1.5 RADMC-3D: A radiative transfer tool

In order to interpret millimeter observations of young stellar objects, it is necessary to translate the observable quantities (i.e. emission) to physical properties, such as geometry, density, temperature. To this aim, the understanding of the propagation of photons from the heating source to the observer is essential. This is known as "radiative transfer" or "radiation transport". This work relied heavily on radiative transfer modeling; therefore, the basic radiative transfer problem will be summarised in the following sections, as well as the numerical basis of the 3D MC radiative transfer code RADMC-3D.

1.5.1 Radiative transfer equations

The following summary on the basic radiative transfer problem is based on the books by Rybicki & Lightman (1979) and LeBlanc (2010), the lecture notes by Dullemond (2012)[5] and the RADMC-3D manual book[6].

Radiative transfer describes the interaction of the radiation with the medium. There are two main interactions: radiation being injected (emission) into a light ray and radiation being removed (absorption/scattering) from a light ray. These process are combined and play a role in the dust interaction within disks and envelopes in young protostars.

In the vacuum, the transport of radiation is trivial, since the intensity in any direction remains constant along a ray in that direction. Hoewever, e.g. in the ISM, the specific intensity I_ν at a frequency ν will not remain constant and it will vary along a specific ray. The change in intensity along a path with length s in direction $\vec{n}$ is described by the radiative transfer equation,

$$\frac{dI_\nu(\vec{n},s)}{ds} = -\alpha_\nu(s)\, I_\nu(\vec{n},s) + j_\nu(s), \tag{1.13}$$

where $\alpha_\nu(s)$ is the extinction (or absorption) coefficient and $j_\nu(s)$ is the emissivity. In the following sections a variety of solutions for equation 1.13 are presented. To solve the equations, the geometry in Fig. 1.11 are considered as reference.

In the case of a medium with α_ν=0, equation 1.13 is reduced to:

$$\frac{dI_\nu}{ds} = j_\nu, \tag{1.14}$$

which has the solution

$$I_\nu(s) = I_\nu(s_0) + \int_{s_0}^{s} j_\nu(s')ds'. \tag{1.15}$$

The interpretation of this equation is simple: The increase in brightness is equal to the emission coefficient integrated along the line of sight.

---

[5] `http://www.ita.uni-heidelberg.de/~dullemond/lectures/radtrans_2012/index.shtml`

[6] `http://www.ita.uni-heidelberg.de/~dullemond/software/radmc-3d/radmc-3d_v0.41.pdf`

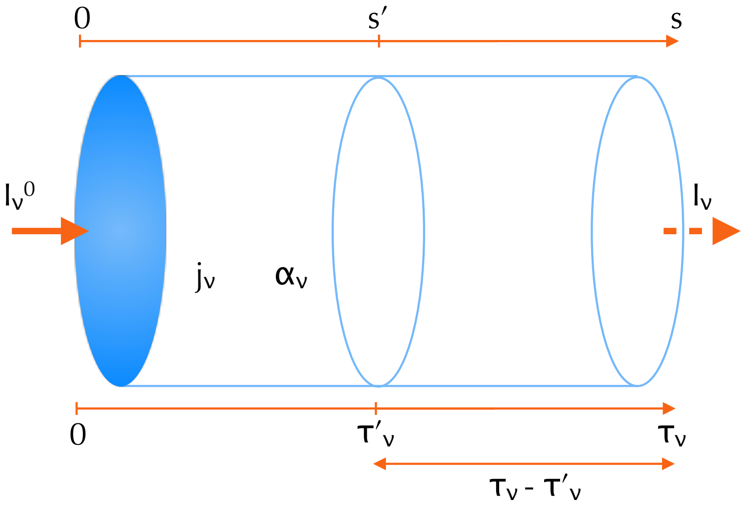

Figure 1.11: Geometry used to solve the radiative transfer equation. Adapted from "An Introduction to Radiative Transfer: Methods and Applications in Astrophysics" book (Peraiah, 2001).

Another case is when there is no emission (j_ν=0). Then Eq.1.13 becomes

$$\frac{dI_\nu}{ds} = -\alpha_\nu I_\nu, \tag{1.16}$$

which has the solution,

$$I_\nu(s) = I_\nu(s_0)exp\left[-\int_{s_0}^{s} \alpha_\nu(s')ds\right]. \tag{1.17}$$

The interpretation of this results is the following: The brightness decreases along the ray by the exponential of the absorption coefficient integrated along the line of sight.
Now, instead of s, we can use another variable called optical depth. The optical depth between s_0 and s along a ray can be expressed as the following integral:

$$\tau_\nu(s) = \int_{s_0}^{s} \alpha_\nu(s')\,ds'. \tag{1.18}$$

From this equation, we can distinguish two regimes. If a medium has a high optical depth, that is $\tau \gg 1$ when integrated along a typical path through the medium, it is said to be *optically thick* or opaque. On the contrary, when $\tau \ll 1$, only a small fraction of the photons are absorbed and the medium is said to be *optically thin* or transparent. Often the density-dependence of the extinction coefficient is explicitly written as:

$$\tau_\nu(s_0, s_1) = \int_{s_0}^{s_1} \kappa_\nu(s)\rho(s)\,ds, \tag{1.19}$$

where κ_ν(s) is the mass-weighted opacity with CGS units of cm^2 g^{-1} and ρ(s) the mass density of the absorbing medium with CGS units of g cm^{-3}.
The transfer equation can now be written, after dividing by α_ν as

$$\frac{dI_\nu}{d\tau_\nu} = -I_\nu + S_\nu. \tag{1.20}$$

The source function S_ν is defined as the ratio of the emissivity to the extinction coefficient:

$$S_\nu \equiv \frac{j_\nu}{\alpha_\nu}. \tag{1.21}$$

S_ν is often a simpler physical quantity than the emissivity, so Eq.1.13 can be rewritten in terms of I_ν and S_ν, and be integrated to obtain the formal solution of the radiative transfer equation in the geometry of Figure 1.11:

$$I_\nu(\tau_\nu) = I_\nu^0 e^{-\tau_\nu} + \int_0^{\tau_\nu} e^{-(\tau_\nu - \tau_\nu^{'})} S_\nu(\tau_\nu^{'}) d\tau_\nu^{'}. \tag{1.22}$$

As an example, consider S_ν=constant. The equation 1.22 is reduced to:

$$I_\nu(\tau_\nu) = I_\nu^{\tau_\nu,0} e^{-\tau_\nu} + S_\nu \int_{\tau_\nu,0}^{\tau_\nu} e^{-(\tau_\nu - \tau_\nu^{'})} d\tau_\nu^{'} = I_\nu^0 e^{-\tau_\nu} + \left(1 - e^{-\tau_\nu}\right) S_\nu, \tag{1.23}$$

where I_ν^0=$I_\nu^{\tau_\nu,0}$. This case shows that I_ν is a weighted sum of the incoming specific intensity and the source function. The important factors to analyze in this solution are the exponential of the optical depth, $e^{-\tau_\nu}$, and the complement (1 - e^{τ_ν}).

For small optical depth inside a cloud, $\tau_\nu \sim 0$, then (1 - e^{τ_ν})~ 0, therefore $I_\nu \sim I_\nu^0$. This result implies that initially, the specific intensity which propagates from left to right (see Figure 1.11) inside the cloud is simply the incoming intensity. Moreover, for high optical depths, $e^{-\tau_\nu} \sim 0$, then (1 - e^{τ_ν}) ~ 1 and $I_\nu \sim S_\nu$. In other words, the mean free path of photons is relatively small and therefore the radiative field depends mostly on the local conditions.
In the case of local thermodynamic equilibrium (LTE), that considers that scattering can be neglected, Kirchoffs law applies and the source function is simply equal to the Planck function, $S_\nu = B_\nu(T)$. With Eq. 1.23 is also possible explain how spectroscopic emission features and absorption features are formed. In the optically thin case we observe that the outgoing emission is equal to the background intensity plus the emission from the cloud between s_0 and s_1. In the case of a transparent cloud where usually the background is dark, the spectral feature will be notorious and it will have the same shape as the feature in the emissivity function. In a optically thick cloud, in addition to emission features, absorption features are produced. This emission/absorption features depends strongly on the temperature gradient. Assuming that the optically thick background is a perfect blackbody and Eq. 1.23, we can understand that if a hot layer is in front of a cool layer, we get emission features, and if a cool layer is in front of a hot layer, we get absorption features.

In the case of $\tau \gg 1$, the feature becomes optically thick and saturates. This is because the intensity wants to approach the Planck function of the foreground layer. Once it has arrived at that Planck function, it will not change any further. Another case, for an optically thick cloud with a constant temperature, then it would not observe any features in the spectrum.

1.5.2 Monte Carlo method

Multiple dust continuum radiative transfer packages have been developed and applied to young objects (e.g., MCFOST (Pinte et al., 2006), HYPERION (Robitaille, 2011) and RADMC-3D (Dullemond et al., 2012)). The numerical method used in all these codes is a probabilistic one called *Monte Carlo* method. In the following paragraphs will briefly introduce this method in the context of RADMC-3D.

Radiative transfer is an inherently three-dimensional problem. The full radiative transfer equation can only be solved analytically in special cases and simple geometries: in general it must be approximated, or solved numerically. However, that the difficulty of radiative transfer is that it is inherently non-local. (photons emitted at one location will effect the emission at an other often distant location). As we showed in the previous examples, it is difficult to know how a single photon will behave in a medium. An easier approximation is to constrain how a group of N photons behave in terms of their statistical properties. The basic procedure of a Monte Carlo method is as follows:

1. Photon packages are released successively from a luminosity source
2. The paths between absorption, re-emission and scattering events are tracked
3. A random number generator is used to find the optical depth τ that the photon will travel until the next scattering event
4. The photon travels along the ray cell-by-cell, where each segment of ray corresponds to some $\Delta\tau$
5. Each time a photon package enters a cell of the grid increases the energy of this cell and thus increases the temperature of the dust of this cell.
6. The next scattering event will happen when $\Delta\tau$ is larger that the remaining τ
7. Every step along the segment of ray, $\tau \leftarrow \tau$ - $\Delta\tau$ is evaluated
8. The journey of each photon ends when it eventually escapes the cloud
9. Once it escapes, a new photon package is launched, until also it escapes
10. After all photon packages have been launched and escaped, the dust temperature that remains is the final temperature result.

One must keep in mind that the final temperature is an equilibrium dust temperature. It assumes that each dust grain acquires as much energy as it radiates away. This is a very good approximation, because the heating/cooling time scales for dust grains are typically very short compared to any time-dependent dynamics of the system.

1.5.3 Dust opacity calculation

RADMC-3D requires dust opacities as a basic model input. Composition and size distributions can be modified as the taste of the user. In this thesis BHMIE code of Bohren & Huffman (1983) modified by Bruce T. Draine is used for the opacity calculation. In this section the opacity κ_ν theory and computation will be described.

First, the optical constants are calculated for mixed-composition particles using the Bruggeman (1935) mixing theory, that allows us to compute the optical properties of dust grains made of different chemical components. The composition of the grains is: water, carbon and silicate mixture in a 6:3:1 volume fractional ratio respectively. The average density $\bar{\rho}$ of the composite grain in the dust model is 1.36 g cm^{-3}.

A typical dust grain is made out of dielectric material, so it reacts to the oscillating electromagnetic field of the radiation. Using Bruggeman (1935) theory is possible to derive an effective dielectric function ϵ_{eff} for a composite material by solving the following mixing rule:

$$\sum_{j=1}^{N} f_j \frac{\epsilon_j - \epsilon_{\mathrm{eff}}}{\epsilon_j + 2\epsilon_{\mathrm{eff}}} = 0, \tag{1.24}$$

where f_j is the volume fraction of the j-th component, and the dieletric function[7] is defined as $\epsilon_j = m_j^2$. In order to to convert the dielectric function into an opacity, the Mie theory (Mie, 1908) is used. This theory solves the Maxwells equations. For a single grain, the opacity follows:

$$\kappa_{\mathrm{abs}}(\nu, a) \equiv \frac{C_{\mathrm{abs}}}{m} = \frac{Q_{\mathrm{abs}}\pi a^2}{m} = \frac{3}{4a\bar{\rho}} Q_{\mathrm{abs}}(\nu, a), \tag{1.25}$$

where C_{abs} is the absorption cross section and m is the grain mass. $Q_{\mathrm{abs}}(\nu,a)$ is normalized absorption cross section for a grain of radius a. In the case of a dust grain population with size distribution n(a), the overall opacity is obtained by mass-averaging κ_{abs} over the population:

$$\kappa_\nu = \frac{1}{M}\int_{m_{\mathrm{min}}}^{m_{\mathrm{max}}} \kappa_{\mathrm{abs}}(\nu, m)\, n(m)\, m\, dm = \frac{4\pi\bar{\rho}}{3M}\int_{a_{\mathrm{min}}}^{a_{\mathrm{max}}} \kappa(\nu, a)\, n(a)\, a^3\, da, \tag{1.26}$$

where the mass of a grain is given by m=$4/3\pi\bar{\rho}a^3$ and M is the total mass of the dust population. Concerning the grain size distribution used in this work, a power law, $n(a) \propto a^{-q}$ is assumed. Where an index of q=3.5 (Mathis, Rumpl and Nordsieck (MRN) distribution, (Mathis et al., 1977) and q=3.0 are used.

---

[7] m_j is the complex refractive index of the material given by m_j=n_j+ik_j

At mm/sub-mm wavelengths, the frequency dependence of κ can be approximated with a power law following:

$$\kappa(\nu) = \kappa_0 \left(\frac{\nu}{\nu_0}\right)^{\beta}, \tag{1.27}$$

where κ_0 is a normalization factor and β is the dust opacity spectral index.
Figure 1.12 shows the size-dependency of opacity and the effect of change the slope q. For grain sizes of, a=0.1μm and a=100μm) the opacities beyond 100μm do not depend on a_{max}. But when the grain size becomes bigger a=1000μm) the opacity does change, and becomes nearly flat at longer wavelengths.

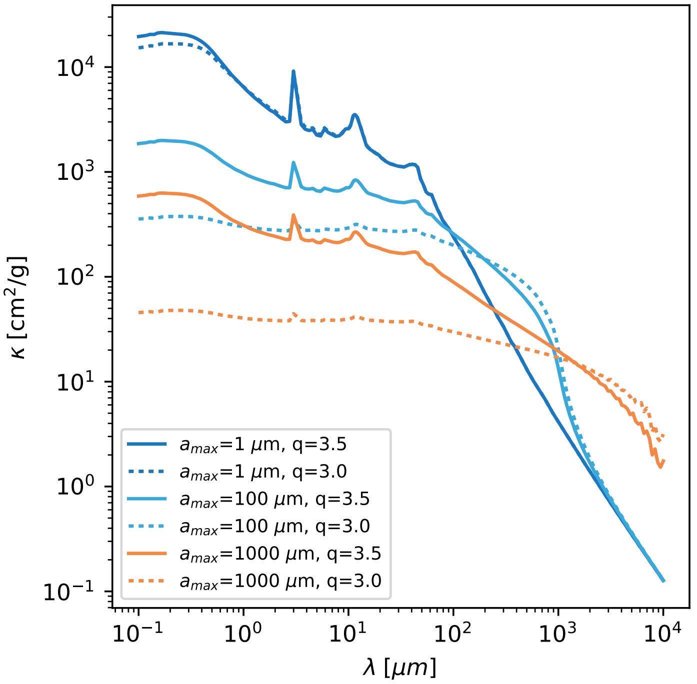

Figure 1.12: Dust absorption opacity as a function of wavelength for grain size distributions characterized by $n(a) \propto a^{-3.0,-3.5}$ and increasing maximum grain size from 1μm to 1000μm.

1.5.4 Making synthetic images

Images and spectra are typically made after the dust temperature has been determined using the thermal Monte Carlo run. At given wavelength, inclination and position angle (PA) an image can be calculated with the ray-tracing capability of RADMC-3D. In order to compare those images or model results with the sub-mm observations visibilities, an extra step is needed. For that purpose we used GALARIO (GPU Accelerated Library for Analysing Radio Interferometer, Tazzari et al. (2018)). GALARIO is a library that computes synthetic visibilities given a model image (or an axisymmetric brightness profile) and then compare to the observations. In this study we use GALARIO code in two procedures: (1) to compute the synthetic visibilities of a model image at the specified *uv*-locations; the 2D surface brightness in image is Fourier transformed and sampled in the *uv*-locations given in the u and v datasets. (2) To compute the χ^2 of a model image given the observed visibilities. The χ^2 is computed from the observed and synthetic visibilities as:

$$\chi^2 = \sum_{j=1}^{N} w_j * [(ReV_{obs\ j} - ReV_{mod\ j})^2 + (ImV_{obs\ j} - ImV_{mod\ j})^2], \tag{1.28}$$

where V_{mod} are the synthetic visibilities, which are computed in the previous step, w_j are the weights associated to the dataset and Re/Im are the real and imaginary part of the observed visibilities respectively.

1.6 Motivation

As already mentioned in the previous sections there are many uncertainties and questions related to the process of star formation. The key questions I seek to address are: **Does grain growth occur in the early stages of protostellar disks?**

Are Class I protostars the key stage to understand the grain growth and dust coagulation in protoplanetary disks?

The assembly of the first millimeter size solids during the protostellar evolutionary phase would have important implications, because it would suggest an efficient and earlier planetesimal formation phase in disks. In fact, if large (from mm to cm-sized) dust particles from the inner envelope are deposited in the disk at large radii during the disk formation stage, the dust grains would be much less affected by the transport and fragmentation processes that prevent the growth from sub-micron particles.

Nevertheless, the growth of solids in cores and envelopes to millimeter or centimeter sizes is not straightforward. Ormel et al. (2009) studied the grain growth in cores finding that while it is easy to grow dust to micron size particles, the growth to millimeter or centimeter size pebbles requires high densities and relatively long timescales; and it is being unclear how to overcome this size barrier. Observational constraints on the grain growth process in protostellar envelopes and disks are thus needed to test our understanding of dust evolution. **Especially critical is to map the level of grain growth in the various regions of the protostellar system: disk, inner in-falling envelope and outer envelope, in order to understand whether in these regions the dust growth starts and how these process are connected to the growth of dust required to form future planetesimals.**

To investigate these unknowns I studied the dust continuum emission at millimeter wavelengths, which allows us to test the presence of mm-sized dust grains. This is due to the fact that the emission at these wavelengths is expected to be mostly optically thin, and therefore at any line of sight the emission is $F_\nu \propto \kappa_\nu B_\nu$. A simple parametrization of the dust opacity $\kappa_\nu \propto \nu^\beta$ allows us to asses the level of grain growth. Moreover, since the emission is in the Rayleigh-Jeans regime, $F_{\nu} \propto \nu^{2+\beta}$, the variation in the flux between different frequencies is a good proxy for the spectral index β. Values of $\beta \sim 1$ indicate that mm-sized particles have been formed, while values around $\beta \sim 1.7$ represent the sizes of interstellar medium (ISM) particles.

The evidence of grain growth up to mm-sizes in early stages of star formation is not totally conclusive.

Classical protoplanetary disks (around Class II objects) show $\beta \leqslant 1.0$ interpreted as clear signs of dust coagulation and an increased in grain size of the order of $\geqslant 1$ mm, regardless the composition (Pérez et al., 2015; Tazzari et al., 2016a).

Toward pre-stellar cores the evidence is less clear: at near-to mid-IR wavelengths sign of the existence of ~1 μm dust grains related with the coreshine effect (Pagani et al., 2010) has been recently questioned by (Jones et al., 2013; Ysard et al., 2016), who suggest that the coreshine effect could be explained with aliphatic-rich ice-mantled grains instead of evolved micrometer-sized grains. Additionally, Chacón-Tanarro et al. (2017) by using analytical models of grain growth in cores found that dust grains reach sizes of ~ 3-4 μm in the central 2000 au of L1544. Some evidence of grain growth has been collected towards a few Class 0 sources (e.g Jørgensen et al., 2007; Kwon et al., 2009; Chiang et al., 2012a), but at these early stages the analysis of disk properties are complicated by the presence of significant accretion of material from the envelope and jets (e.g. Tobin et al., 2010). Thus, large uncertainties affect measurements of the dust spectral index β toward Class 0 sources.

Analyzing dust properties in Class I protostars it is more straightforward to Class 0 sources because the surrounding envelope is less massive, and it is possible to separate the disk from the envelope contribution in the visibility domain.

However, **only a few Class I protostars have been studied to constrain the dust properties**, finding grains grown up to mm size in the envelope of two Class I protostars (Miotello et al., 2014). Additionally, Sheehan & Eisner (2017, 2018) studied a sample of Class I protostars in Taurus and GY 91 in ρ Ophiuchus, finding similar grain sizes. They derived a $\beta \approx 1$, which is consistent with the results for Class II sources.

The previous mentioned measurements of the spectral index β in Class I/II disks that are located in different star forming regions suggest: **1)** the grain growth process efficiently produces grains with sizes up to ~ 1mm (timescales of 1-3 Myr; Ricci et al. 2010a) and **2)** there must be a mechanism to retain ~1-100 μm size dust grains in more evolved disks.

Class I protostars represent therefore an intriguing and key phase to study the first stages of grain growth. Furthermore, this stage sets the initial conditions for the evolution of the protoplanetary disks.

1.7 Goal of this Thesis

The main goal of this Thesis is to study in depth the dust and physical properties of a Class I protostars, in order to provide evidence on the initial conditions for planet formation. In particular, we will study in detail the Class I protostars Per-emb-50. Per-emb-50 is a

single source and the brightest Class I protostar located in the NGC 1333 complex in the Perseus star forming region.
Per-emb-50 was observed at 1.29 mm with the Submillimeter Array (SMA) within the legacy program MASSES (Mass Assembly of Stellar Systems and Their Evolution) (Stephens et al., 2018). Our study combines 1.29 mm MASSES data from the SMA interferometer with new longer wavelength observations with NOEMA (Agurto-Gangas et al., 2019) and high resolution data from the VLA Nascent Disk and Multiplicity (VANDAM) survey (Tobin et al., 2015; Segura-Cox et al., 2016). The observations at 8.1 mm allow us to study the compact disk in Per-emb-50 at a resolution of ∼20 au while the 2.72 mm and 1.29 mm datasets, that nicely overlap on large physical scales, permit the examination of the inner envelope region.

In the following, I briefly summarize the content of all the next chapters.

- **Chapter 2** - I present the analytical and radiative transfer modeling of Per-emb-50 using two millimeter continuum datasets at 1.29 and 2.72 mm, obtained with SMA and NOEMA arrays. In the first method, I model the observed emissions in the visibility plane as an analytic unresolved disk and an envelope. Its simplicity allows us to disentangle the emission of the disk and the envelope components and determine the spectral index for each component as well. For this analysis I found a spectral index of α=3.3±0.3 (β=1.3±0.3) in the envelope of Per-emb-50 consistent with ISM dust ($\beta \sim 1.7$), contrary to other findings than in average are close to $\beta \sim 0.7$ and related to dust grains up to millimeter sizes (Miotello et al., 2014). I also analyzed Per-emb-50 with more detailed dust radiative-transfer models. We compared a grid of models following (Miotello et al., 2014) analysis, that use a partial radiative transfer model and the analysis used in this work that create a full radiative tranfer model for the envelope and disk together. Using these methods I revealed that the envelope of Per-emb-50 is consistent with a maximum grain size of $a_{\max} < 100\,\mu$m. In addition, I found that the effect of the envelope's thermal emission on the disk (i.e. backwarming), often ignored for those objects, may significantly affect the gas phase chemistry and the dust mantle chemistry in young sources. The degree of the warming effect depends on the envelope density profile. In the collapsing envelope model (i.e. Ulrich (1976) profile), the temperature effect on the outer regions of the disk is weak, but if a power-law envelope is used, (Tafalla et al., 2002), the effect is more obvious. The results of this project were published in Agurto-Gangas et al. (2019).

- **Chapter 3** - I analyzed the disk properties of Per-emb-50. I combined the previous SMA and NOEMA observations of Per-emb-50 with the high resolution data from the the VLA Nascent Disk and Multiplicity (VANDAM) survey (Tobin et al., 2015; Segura-Cox et al., 2016) in order to study the compact disk of Per-emb-50 at a resolution of ∼20 au, as well as the inner-envelope on scales of ∼3000 to 1000 au. I used the 8.12 mm VLA data in addition to our 1.3 and 2.7 mm data in order to compare with the dust and disk properties assumed in Chapter 2. The detailed radiative transfer modelling of the disk allow us to determine new estimates of the disk, with a dust mass of $468\,M$ and outer disk radius of 38 au. We put constraints on the level of grain growth between 25 and 38 au in the disk, finding a lower limit for the maximum grain size of $\geqslant 735\,\mu$m with a power law grain size distribution of q=3.5. The level of grain growth in the innermost disk zone remains unconstrained given that it is optically thick, requiring optically thin multi-wavelength observations to determine this. Additionally, we provide a better fit and constraints for the envelope using an Ulrich profile. We find an envelope rotational radius of 113 au, and an envelope maximum grain size of 26 μm, which is in agreement with the findings in previous envelope models of Agurto-Gangas et al. (2019).

- **Chapter 4** - In order to improve the analysis of millimeter multi-wavelength observations of young sources, we develop a fitting framework that it uses Markov Chain Monte Carlo to guide radiative transfer models. `SiDE` (Simple Disk-Envelope) framework produce synthetic dust maps using the radiative transfer tool RADMC-3D and fit the synthetic observations to the true data-set using a Markov Chain Monte Carlo (MCMC) fitting routine. For the development and testing of this framework Per-emb-50 SMA/NOEMA/VLA data-sets and Elias 29 Miotello et al. (2014) observations were used. The future goal of this framework is to be use in the analysis of high resolution multi-wavelength observations of large samples of disks with ALMA that will allow us to spatially resolve the early growth of solids.

- **Chapter 5** - Finally, I summarize the conclusions of this Thesis, highlighting the main findings. Future follow-up work and prospective lines of research are also outlined.

Chapter 2

Revealing the dust grain size in the inner envelope of the Class I protostar Per-emb-50

The content of this chapter has been published in :

`"Revealing the dust grain size in the inner envelope of the Class I protostar Per-emb-50"`
`C. Agurto-Gangas,` `J.E. Pineda, L. Szűcs, L. Testi, M. Tazzari, A. Miotello, P. Caselli, M. Dunham, I.W. Stephens, T.L. Bourke, 2019, A&A`

2.1 Previous studies on dust grain growth in YSOs

Disks and envelopes around protostars play a fundamental role in the process of planet formation since they contain the ingredients out of which planets are formed (Testi et al., 2014).

Thanks to detailed studies of protoplanetary disks at several sub-millimeter and millimeter wavelengths such as HL Tau (Carrasco-González et al., 2016), CY Tau, DoAr 25, and FT Tau (Pérez et al., 2015; Tazzari et al., 2016b) it is now well established that the radial profiles of their grain-size distributions are compatible with millimeter-sized grains. However, it is not yet clear at which stage of the star and planet formation process dust grains start to efficiently coagulate and evolve from micrometer-sized particles to macroscopic dimensions.

Ormel et al. (2009) studied in detail the possibility of grain growth in pre-stellar cores and found that while it is easy to grow to micron-sized particles, the growth to millimeter- or centimeter-sized pebbles requires high densities and relatively long timescales of $\sim 10^7$ yr, much longer than the lifetimes of dense cores. This is also explored recently in Chacón-Tanarro et al. (2017), where they calculate the grain size in the center of the pre-stellar core L1544, finding that only in the central 300 au, can grain size grow to about 200μm.

In the earliest protostellar phases, for example during the Class 0 stage, the protostar is fully embedded in the parent envelope, while in the Class I phase, the envelope is partially dissipated and the disk emission can be better separated from the envelope. Therefore, Class I protostars can more easily address the start of planetesimal formation and constrain the initial conditions of the evolution of protoplanetary disks.
The possibility for the first large solids to assemble during the early phases of disk evolution would have important implications. If the process starts already in the Class I stage, this would imply a much more effective and rapid planetesimal formation phase in the disks. In fact, if large (mm to cm-size) dust particles from the inner envelope (Chiang et al., 2012a; Tobin et al., 2013; Miotello et al., 2014) are deposited in the disk at large radii during the disk-formation stage, they would be much less affected by the radial transport and fragmentation processes, which adversely affect the growth from sub-micron particles, and large dust aggregates could form (Birnstiel et al., 2010). The advantage of studying protostars at millimeter wavelengths is that the dust emission from the envelope and the disk is mostly optically thin. In this wavelength range, the dust opacity coefficient κ_ν, can be approximated by a power law $\kappa_\nu \propto \nu^{\beta_{\rm mm}}$, where $\beta_{\rm mm}$ is the millimeter dust opacity spectral index, and is directly related to the maximum size of the grain (Natta et al., 2007). In the presence of very large grains, much larger than the observing wavelength, the opacity becomes gray (only the geometrical cross section of the grains is relevant) and $\beta_{\rm mm} = 0$. Values of $\beta_{\rm mm}$ can be estimated by measuring the slope $\alpha_{\rm mm}$ of the sub-millimeter spectral energy distribution (SED), $F_\nu \propto \nu^{\alpha_{\rm mm}}$. When the Rayleigh–Jeans approximation is applicable, the spectral index of the observed flux densities, $\alpha_{\rm mm}$, would translate to a power-law index of the dust opacity $\beta_{\rm mm} = \alpha_{\rm mm} - 2$. While values around $\alpha_{\rm mm} \sim 3.7$ represent size distribution similar to interstellar medium (ISM) particles (Natta et al., 2007; Testi et al., 2014). Classical protoplanetary disks around Class II objects, present clear signs of dust coagulation, with $\alpha_{\rm mm} \leqslant 3$ (Testi et al. 2014, and references therein).
Previous observations of Class 0 protostars by Chiang et al. (2012a), Jørgensen et al. (2007) and Kwon et al. (2009) indicate spectral indexes $\alpha_{\rm mm} \sim 3$, which is shallower than the ISM, but not quite as steep as Class II disks. However, Class 0 objects, are affected by the presence of powerful accretion of material from the envelope and jets [e.g.], (Tobin et al., 2013), making them difficult to observe and model. In contrast, Class I protostars have less-massive envelopes, which provides a cleaner analysis of the dust properties since the envelope and disk emission can be separated.

Here we present a dual-wavelength analysis and modeling on the Class I protostar Per-emb-50, in the Perseus star forming region. Observations and data reduction are described in Sect. 2.2 In Sect. 2.3 we present our observational analysis. The modeling and discussion are presented in Sects. 2.4 and 2.5 respectively. Conclusions and future work are in Sect. 2.6.

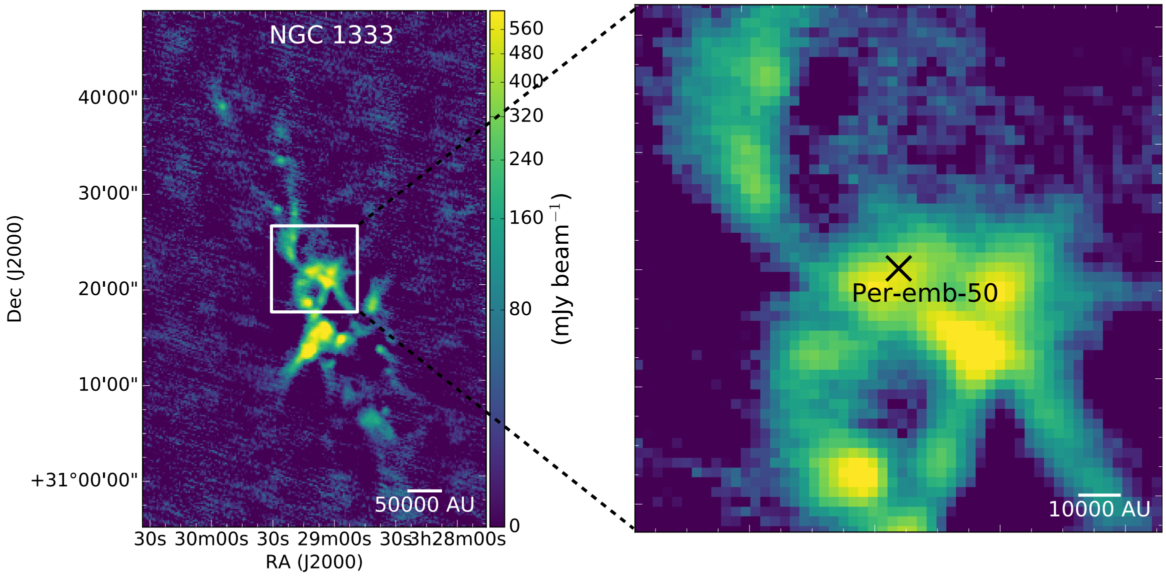

Figure 2.1: (Left) Continuum map of the NGC1333 complex at 1.1mm wavelength. (Right) Zoom-in to the direct environment of Per-emb-50. The map is adapted from the Bolocam survey at the Caltech Submillimeter Observatory (CSO) by Enoch et al. (2006).

2.2 Observations

2.2.1 The source

Per-emb-50 is a protostar located in the active cluster forming region NGC1333 in the Perseus cloud (see Figure 2.1), at a recently revised distance of 293 pc (Ortiz-León et al., 2018; Zucker et al., 2018). It is classified as a Class I protostar from the slope of its SED in the near- and mid-infrared ("Cores to Disks" or c2d Spitzer Legacy project from, Evans et al. 2003). Based on Bolocam 1.1mm data, the bolometric temperature is T_{bol}=254±23 K. The rescaled bolometric luminosity is L_{bol}=13.7±3 $L_{\odot}$, making it one of the brightest Class I sources in Perseus.

High-angular-resolution observations conducted at 8 mm in the VLA Nascent Disk and Multiplicity (VANDAM) survey, provide a lower limit for the disk mass and outer disk radius. The rescaled values from Segura-Cox et al. (2016) for mass and radius are: M_{disk}=0.28–0.58 $M_{\odot}$ and r_{out}=27–32 au, respectively.

Literature values for envelope mass, disk mass, disk inclination, and other parameters are presented in Table 5.1. We note that some of these physical parameters were calculated using the 230 pc from Hirota et al. (2008) or 250 pc in the case of Bolocam observations. Therefore, we rescale the limits taking into account the different distance adopted.

Even though Per-emb-50 presents a small disk at 8 mm, it is the perfect candidate for studying the growth in the inner envelope and their dust properties.

Table 2.1: Parameters from literature.

Source	Per-emb-50	New value	Ref
RA_{J2000}	03:29:07.76	–	1
Dec_{J2000}	+31:21:57.2	–	1
L_{bol} ($L_\odot$)	10±3.0	13.7±3.0	1
M_{env} ($M_\odot$)	1.62±0.16	2.2±0.16	1
PA (deg)	170±0.3	–	2
i (deg)*	67±10	–	2
M_{disk} ($M_\odot$)	0.18 – 0.36	0.28 – 0.58	2
R_{disk} (au)	21.9 – 25.7	27.3 – 32.1	2
$F_{1.1mm}$ (mJy)	612 ± 18	–	3

(1) Enoch et al. (2009); (2) Segura-Cox et al. (2016);
(3, single dish observation) Enoch et al. (2006)
Notes. $*i = 0$ is a face-on disk.

2.2.2 Submillimeter Array data

The Submillimeter Array (SMA) data shown in this paper are from the MASSES legacy program (Mass Assembly of Stellar Systems and their Evolution with the SMA, PI: I.W. Stephens, M. Dunham; e.g.,Stephens et al. (2018)).

Per-emb-50 was observed at 1.3 mm with the receiver centered at 220.69 GHz, in the Extended (eight antennas) and Subcompact (seven antennas) configuration with the ASIC (Application Specific Integrated Circuit) correlator during September 2015 and November 2014, respectively. Additionally, Per-emb-50 was observed during October 2015 with the SWARM (SMA Wideband Astronomical ROACH2 Machine) correlator at 1.3mm in extended configuration (see Table 2.2 for more details). Weather conditions were good, with zenith optical depths at 220 GHz of $\tau_{220} = 0.07 - 0.15$.

Calibration was done in MIR software package[1], while imaging was done in MIRIAD software package (Sault et al., 1995), using the standard calibration procedure. We inspected the amplitudes and phases of the calibrators on each baseline in order to look for variations or noisy data, which were manually flagged. Corrections for system temperatures were applied in order to calibrate the atmosphere attenuation in the visibility amplitudes. Detailed information of the calibration can be found in Stephens et al. (2018).

The quasars 3C454.3 and 3C84 were used as bandpass and phase calibrators. The absolute flux was calibrated on Uranus, with ∼20% flux calibration uncertainty. For the purpose of this work, we use the 1.3 mm data in the Subcompact and Extended array configurations, with projected baselines in the range of 23-119 kλ. The resulting combined beam was $1.''72 \times 1.''40$ at P.A. 50.80°.

---

[1] https://www.cfa.harvard.edu/ cqi/mircook.html

2.2.3 NOEMA data

The 2.7 mm data presented in this work were obtained with NOEMA, the IRAM[2] NOrthern Extended Millimeter Array. The observations were performed on November 6 and 12, 2016. The array was in the C compact configuration, with eight antennas (8C) in operation during the first track, and six antennas (6C) in operation for the second. Antennas were based on stations E10, W20, W10, N20*, E18, N11*[3], N17 and E04. The projected baselines were from 7.8 kλ and 102 kλ.
Per-emb-50 was observed for hour angles from -5.8 to 1.5 h for 8C, and from -5.3 to 1.4 h for 6C. In total we spent 9 hours on source. The source 0333+321 was used as phase/amplitude calibrator. The sources LkHa101 and MWC349 were used for the flux calibration, while the quasars 3C84 and 3C454.3 were used for the bandpass calibration. We consider an absolute flux uncertainty of 10%. The total bandpass for the 110 GHz continuum measurement was 2 GHz. Data reduction and image synthesis were carried out using the GILDAS software (Guilloteau & Lucas, 2000) with the procedure of MAPPING> Selfcal. The continuum map (Fig. 2) was produced using natural weighting and the resulting beam size is $2.''1 \times 1.''6$ at P.A. 34.84°. The clean map has a *rms* noise level of 2.1 mJy beam^{-1}.

2.3 Observational analysis

Since we are working with interferometric data, the best way to analyze our source is by working on the visibility domain. This is to avoid biases in the model–data comparison that are introduced by the CLEAN algorithm, u–v sampling, and the imaging process.
In Fig.2.2 we plot the real visibility as a function of the deprojected baseline length (uv-distance). The deprojected uv-distances are given by $R = \sqrt{d_a^2 + d_b^2}$, where $d_a = \sqrt{u^2 + v^2}\sin\phi$ and $d_b = \sqrt{u^2 + v^2}\cos\phi\cos i$, $\phi = \arctan(v/u) - PA$ (Lay et al., 1997). The values for inclination i, and position angle, PA, are presented in Table5.1.
In Fig.2.3, we show images of the SMA and NOEMA observations. Per-emb-50 appears as a point source in these two images, so we do not resolve the embedded disk. Consequently, since the disk is unresolved, then it contributes as a constant component at all baselines. At long baselines, we expect that the amplitude of the visibility is dominated by the disk component, while in shorter baselines the resolved envelope dominates.
For Per-emb-50, the value of the amplitudes start becoming constant above 47 kλ (see Fig.2.2) for both wavelengths. We assume that the emission from those baselines belongs to the embedded disk, where the average values at 2.7 mm and 1.3 mm are: $F_{\rm disk}^{\rm 2.7mm} = 18.82 \pm 0.13$ mJy and $F_{\rm disk}^{\rm 1.3mm} = 63.85 \pm 4.2$ mJy.

The spectral index $\alpha_{\rm mm}$ can be calculated through the flux ratio between two wavelengths,

$$\alpha_{\rm mm} = \frac{\ln \mathrm{F}_1 - \ln \mathrm{F}_2}{\ln \nu_1 - \ln \nu_2} \tag{2.1}$$

---

[2] http://www.iram-institute.org/

[3] Stations with * correspond to antennas not available for the second day track

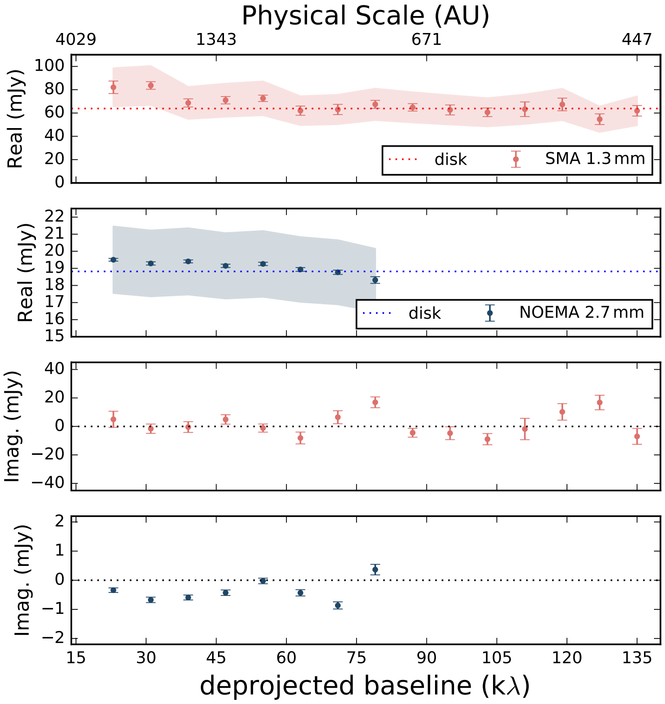

Figure 2.2: Real and imaginary parts of the measured visibilities of Per-emb-50 as a function of the deprojected baseline, assuming the PA and i from Table 1. The data are averaged in 8 kλ bins. The error bars in the real parts show the statistical standard errors of visibilities in each bin. Red and blue shaded areas show the 20% and 10% flux calibration uncertainties of the SMA and NOEMA data, respectively. Red and blue dashed lines are the disk average fluxes using baselines larger than 47 kλ.

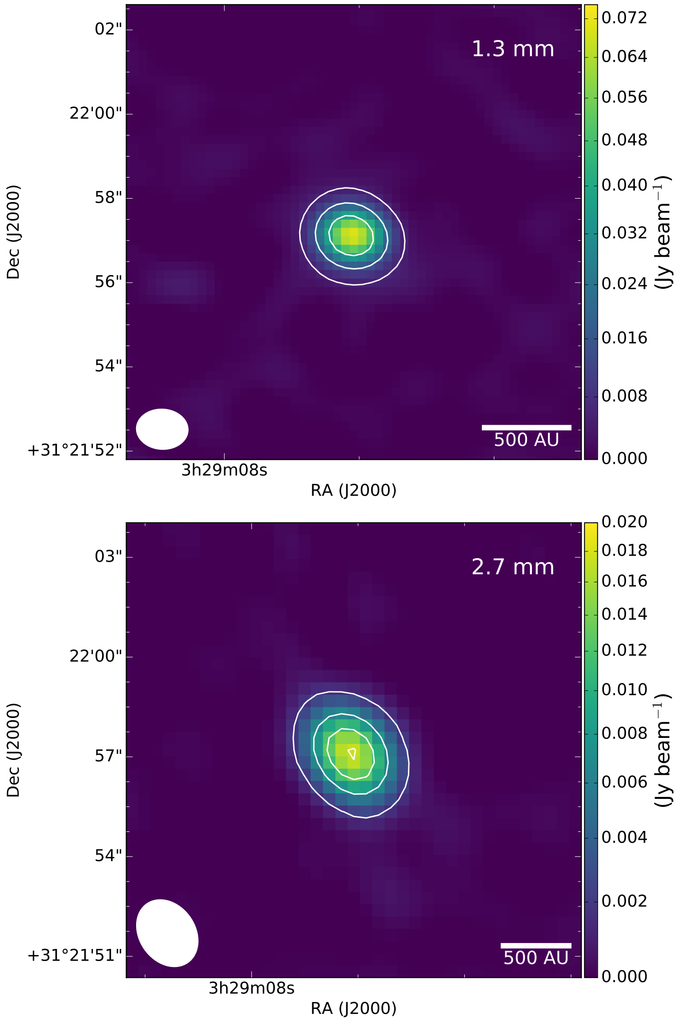

Figure 2.3: Continuum map of Per-emb-50 at 1.3 mm (SMA) and 2.7 mm (NOEMA) wavelengths. The synthesized beam FWHM is represented as a white ellipse in the bottom-left corner of each map. For SMA and NOEMA data, the contours start at 76 mJy beam^{-1} and 20 mJy beam^{-1}, respectively, and both increase in 25% intervals.

Table 2.2: Summary of observations

Observatory	Representative Frequency (GHz)	Date	Flux Calibrator	Bandpass Calibrator	Flux (Jy)	Array Configuration	Synthesized Beam (″)	P.A. (°)
SMA	220	Nov 27 2014	Uranus	3c84	11.64	Subcompact	1.2×0.96	86.9
				3c454.3	16.71	Subcompact		
		Sep 15 2015	Uranus	3c84	11.64	Extended		
		Oct 29 2016	Neptune	3c84	13.8	Extended		
				3c454.3				
NOEMA	109	Nov 6 2016	0333+321	3c454.3	14.03	8C	2.2×1.7	35
		Nov 12 2016	0333+321	3c84	24.80	6C		

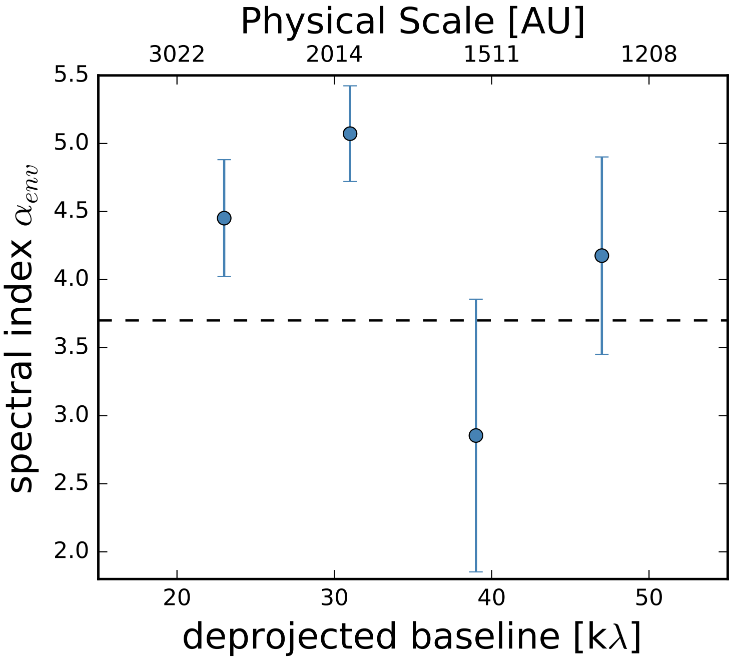

Figure 2.4: Spectral index of the envelope as a function of deprojected baseline. The black dashed line represents the typical value of $\alpha\sim3.7$ related to grain properties in the diffuse interstellar medium.

Using the fluxes between the u-v ranges 47–80 kλ at 1.3 and 2.7 mm, we obtain the average value $\alpha_{\rm mm}$ in the unresolved disk, which is $\alpha_{\rm disk}$=1.71±0.3.
As shown in the Fig.2.2, an excess of emission is present at short baselines (<47 kλ) at 2.7 mm and 1.3 mm, which correspond to physical scales of 1500–3000 au. The excess values at these baselines, after subtracting the disk visibilities, are $F_{\rm ex}^{2.7\rm mm}$=0.52 ± 0.1 mJy and $F_{\rm ex}^{1.3\rm mm}$=10.1 ± 5 mJy. The excess, even if not very pronounced at 2.7 mm, is detected at 1.3 mm, therefore this indicates the presence of extended emission related to the inner envelope. Considering the average fluxes at these very short baselines, and using the same u-v distances ranges at both wavelengths, we recover a greater average value for $\alpha_{\rm env}$ than the typical ISM values, $\alpha_{\rm env}$=4.0 ± 0.8.

The uncertainties in $\alpha_{\rm disk}$ and $\alpha_{\rm env}$ are estimated following the procedure shown in Appendix A, with the absolute flux uncertainty of 10% for 2.7 mm data and 20% for 1.3 mm data added in quadrature. We present $\alpha_{\rm env}$ and its change as a function of deprojected baseline in Fig.2.4. If we translate this value to the spectral index of the dust opacity, we obtain $\beta_{\rm env}\sim2.0$, which is similar to the values found in the ISM.

These preliminary results are showing a discrepancy with previous studies on spectral indexes in Class I protostar or even younger sources with dust opacity indexes $\alpha_{\rm mm}<3$ (Miotello et al., 2014; Kwon et al., 2009; Chiang et al., 2012a). To investigate possible explanations, we performed a partial and full radiative-transfer modeling on envelope and disk to take into account possible deviations from the optically thin and Rayleigh Jeans regimes, which can affect the values of α_{mm}.

2.4 Modeling

In order to model the Class I protostar and compare with the observations, we consider appropriate physical structure and conditions of the source, including the envelope structure, density, properties of the dust grains, and we predict the 1.3 and 2.7 mm emission with a u–v modeling described below.

In the first step, we fit the Per-emb-50 data with a parametric modeling in uv space (Section 4.1) in order to address the α values, as well as visibility comparisons. Afterward, we use the radiative-transfer tool RADMC-3D (Dullemond et al., 2012) in two ways: (a) to apply the modeling approach of Miotello et al. (2014), where the disk and envelope are modeled separately (Section 4.2) and (b) to compute the emission for the new modeling presented in this work, including a self-consistent radiative-transfer model for the disk and the envelope (Section 4.3). In the following sections, we discuss and compare the details of the results of each modeling case.

2.4.1 Parametric model

We implement a model that consists of an extended envelope described by a Gaussian, and an unresolved disk (point source) that has constant flux at all baselines. Therefore, the combined amplitude profile, which depends on the uv distance, defined as $\sqrt{\mathrm{u}^2 + \mathrm{v}^2}$, and frequency, ν, is described by:

$$f(uv, \nu) = F_e \left(\frac{\nu}{\nu_{1.3\mathrm{mm}}} \right)^{\alpha_e} \exp \left(\frac{-(uv)^2}{2\sigma^2} \right) + F_d \left(\frac{\nu}{\nu_{1.3\mathrm{mm}}} \right)^{\alpha_d}, \tag{2.2}$$

where F_{e} and F_{d} are the flux density from the Gaussian emission (extended envelope) and point source emission (unresolved disk) respectively, α_{e} and α_{d} are the spectral indexes of the two components, and σ is the width of the Gaussian given by $\sigma \approx$ FWHM/2.355. In this simple model, we first set the flux from the disk at 1.3 mm based on the average value reported in Sect. 3, F_{d}=63 mJy. Then, four parameters are explored: F_{e}, α_{e}, α_{d} and σ. The Markov chain Monte Carlo (MCMC) method, implemented as a python package *emcee* (Foreman-Mackey et al., 2013a), is used to calculate the posterior probability distributions of each of these parameters. For each model we used the 750 steps after the burn-in and 400 walkers (see Appendix B for more details). The results from this simple model are discussed in the following section.

Parametric model results

In Fig. 2.5, model visibilities are compared with observational data at each u−v sample and wavelength. In Table 2.3 we present the best-fit parameters found for this parametric model. The values of the flux spectral index in the disk and envelope are consistent with

Table 2.3: Best parametric model

Fit parameters	
$F_{\rm e}$ (mJy)	17.0±1.1
$\alpha_{\rm e}$	3.3±0.3
$\alpha_{\rm d}$	1.7±0.3
σ (kλ)	43.1±0.5

Table 2.4: Derived parameters from parametric model

$F_{\rm d}^{\textit{2.7}\rm mm}$ [mJy]	18.4 ± 0.7
$F_{\rm zero}^{\textit{2.7}\rm mm}$ [mJy]	19.8 ± 2.2
$F_{\rm zero}^{\textit{1.3}\rm mm}$ [mJy]	81.3 ± 2
$F_{\rm zero}^{\textit{1.1}\rm mm}$ [mJy]	127.4 ± 2

the observational analysis (see Section 3), but their errors are highly dominated by the systematic error of absolute fluxes and the statistical error of the data. We estimate that the uncertainty on $\alpha_{\rm mm}$ for the envelope and disk using a simplistic approximation for noncorrelated errors is ±0.3.
Additionally, from this simple model we can constrain the size of the region where the envelope emission arises, which has a 1-sigma width (from Table 2.3) of 43 kλ (1405 au). From the model we can derive the flux from the disk at 2.7 mm and the prediction of the total flux at baseline=0 kλ or zero spacing flux, $F_{\rm zero}^{\textit{2.7}\rm mm}$ and $F_{\rm zero}^{\textit{1.3}\rm mm}$. The results are shown in Table 2.4.

We use the derived parameters from our parametric model (Table 2.4) to estimate the zero-spacing flux at 1.1 mm, $F_{\rm zero}^{\tt 1.1mm}$. We find the flux is only 127.4 mJy beam^{-1} which is much lower than the single dish flux of 612±18 mJy reported by Enoch et al. (2006). This discrepancy is related to the resolution of the observations. While our interferometric data are sensitive to the inner envelope of this source, the 31″ beam size of Bolocam recovers the extended emission, which is affected by blending effects, especially in a crowded region such as NGC 1333 (see Fig. 1).

Since this simple model is not taking into account properties of the dust grains and density profiles for both the envelope and disk, we also analyze Per-emb-50 with more detailed dust radiative-transfer models.

2.4.2 Two-step model

For this model, we adopted the procedure described by Miotello et al. (2014), where they analyzed two Class I protostars with a two-step model. The disk is modeled adopting the two-layer model by Dullemond et al. (2001), whose output spectrum is taken as the central source of illumination in the envelope model. The envelope, on the other hand, is modeled

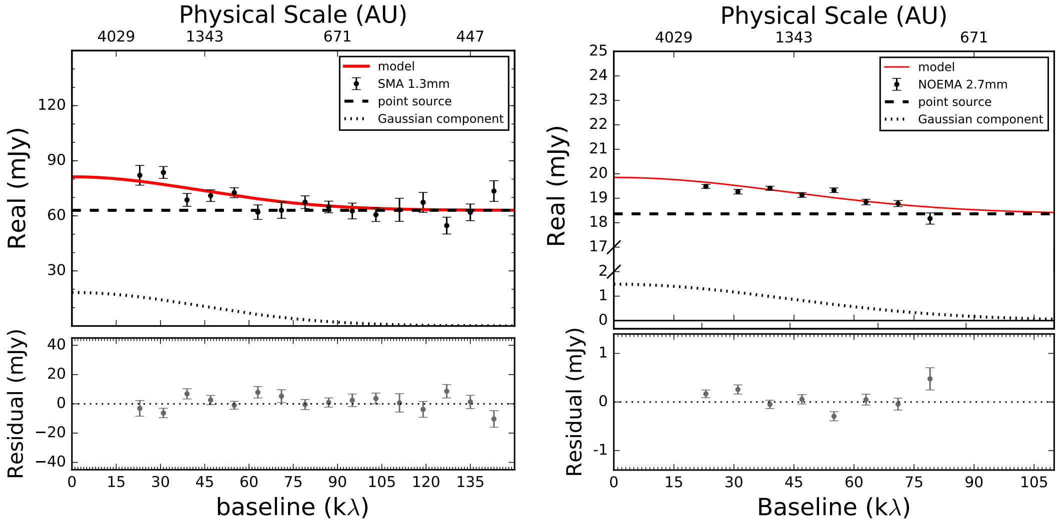

Figure 2.5: Black points are the real part of the visibilities as a function of the baseline length. Red curves show the best-fit model, while the dashed and dotted lines indicate its point source and Gaussian components, respectively. Bottom panels show the residual between the model and data.

Table 2.5: Two-step model grid parameters

Parameter	Description	Values	Parameter Use
Stellar model parameters			
d (pc)	Distance	293	fixed
$L_\star$ ($L_\odot$)	Photosphere luminosity	13.7	fixed
$T_\star$ (K)	Effective temperature	5 011	fixed
$R_\star$ (au)	Stellar radius	0.025	fixed
$M_\star$ ($M_\odot$)	Stellar mass	2.9	fixed
Disk model parameters			
$R_{\rm in}$ (au)	Disk inner radius	0.1	fixed
$R_{\rm out}$ (au)	Disk outer radius	25 27 30 32 34 36	varied
$M_{\rm disk}$ ($M_\odot$)	Disk mass	0.05 0.1 0.15 0.2 0.3 0.4	varied
$\Sigma_{\rm disk}$ (gr cm^{-2})	Disk surface density	54.7–908	varied
$a_{\rm max}^{disk}$ (μm)	Disk maximum grain size	500 1 000 5 000 10 000 20 000	varied
RADMC-3D / Envelope parameters			
$r_{\rm in}$ (au)	Envelope inner radius	25 27 30 32 34 36	varied
$r_{\rm out}$ (au)	Envelope outer radius	8 800	fixed
$R_{\rm rot}$ (au)	Centrifugal radius	100–1000	varied
ρ_0 (gr cm^{-3})	Density in the equatorial plane at $R_{\rm rot}$	0.5×10^{-20}–20.0×10^{-20}	varied
$a_{\rm max}^{env}$ (μm)	Envelope maximum grain size	0.1–1 000	varied

Each model is calculated with 1×10^6 photons for the thermal Monte Carlo.

using RADMC-3D (Dullemond et al., 2012).

Modeling protostar and disk

We adopt a simple disk model heated by protostellar radiation. We calculate the properties of the central protostar, assuming that it emits black body radiation, characterized by a radius $R_\star$, effective temperature $T_{\rm eff}$, and mass $M_\star$. To obtain $T_{\rm eff}$ we assume that Per-emb-50 lies along the birthline for intermediate mass stars by Palla & Stahler (1990). Given the rescaled bolometric luminosity $L_{\rm bol}$ reported in Table 5.1, we estimate $T_{\rm eff}$=5011 K. With $L_{\rm bol}$ and $T_{\rm eff}$, we can estimate $R_{\rm eff}$ using the Stefan-Boltzmann law:

$$R_{\rm eff} = \left(\frac{L_{\rm bol}}{4\pi\sigma T_{\rm eff}^4}\right)^{1/2}, \tag{2.3}$$

Subsequently, with $R_{\rm eff}$=5.01 $R_\odot$, we use the mass-versus-radius relation for a spherical protostar accreting at a rate of 10^{-5} $M_\odot$ yr^{-1} from Palla & Stahler (1991), to deduce an effective mass of $M_{\rm eff}$=2.9 $M_\odot$ (Table. 2.5). Additionally, we add a disk structure defined by an inner and outer radius, $r_{\rm in}$ and $r_{\rm out}$, an inclination angle i, and a dust surface density profile that follows a simple power law,

$$\Sigma(R) = \Sigma_0 \left(\frac{r_{out}}{r_{\Sigma_0}}\right)^{-p}, \tag{2.4}$$

where Σ_0 is the surface dust density fixed at r_{Σ_0}= 1 au from the central protostar, and where p=1 since the quality of the data is not sensitive enough to discriminate between different values of p. The disk inclination i is fixed to 67° as found by Segura-Cox et al. (2016). Since the millimeter-SED is not sensitive to $r_{\rm in}$, we set $r_{\rm in}$=0.1 au. $r_{\rm out}$ and M_{disk} can be constrained by our observations assuming a dust opacity (see Section 4.2.3) and gas-to-dust mass ratio of 100.

Modeling the envelope

We adopted the rotating and collapsing spheroid structure by Ulrich (1976) to model the envelope. The density of this envelope structure is given by,

$$\rho_{\rm env}(r,\theta) = \rho_0 \left(\frac{R_{\rm rot}}{r}\right)^{3/2} \left(1+\frac{\cos\theta}{\cos\theta_0}\right)^{-1/2} \left(\frac{\cos\theta}{2\cos\theta_0}+\frac{R_{\rm rot}}{r}\cos^2\theta_0\right)^{-1}, \tag{2.5}$$

where ρ_0 is the density in the equatorial plane at the centrifugal radius $R_{\rm rot}$ of the envelope, and θ_0 is the solution of the parabolic motion of an infalling particle given by:

$$\frac{r(\cos\theta_0 - \cos\theta)}{(R_{\rm rot}\cos\theta_0\sin^2\theta_0)} = 1 \tag{2.6}$$

The outer radius of the envelope is fixed at 8 800 au, which is equivalent to the 30″ aperture of Bolocam. In this case we use the envelope mass derived by Bolocam to compare with

the models. We computed $\rho_0$by imposing a total envelope mass $\mathrm{M}_{\mathrm{env}}$, and R_{rot}, which can have a significant influence on the amplitude as a function of baseline, it was left free to vary. Outflow cavities are not included in this model.
RADMC-3D is used to compute the temperature of the envelope, with the implementation of Eq. (5) to describe the density structure. The protostar and disk system presented in the previous subsections are used as the heating source of the envelope, whose emission is calculated using the two-layer model by Dullemond et al. (2001), and then the output spectrum is used in the 2D radiative-transfer calculation for the envelope structure.

Dust opacity

We adopt the dust opacity model used in Ricci et al. (2010a). A dust population characterized by a distribution of grains with different sizes was implemented. We used a truncated power-law distribution $\mathrm{n}(a) \propto a^{-q}$, between a minimum and a maximum grain size, a_{min} and a_{max} respectively. We fixed the chemical composition to a silicate, carbonaceous material and water ice in a 1:2:3 volume fractional ratio. Additionally, we set a_{min}=0.01 μm and we use q=3.0. We varied $a_{\mathrm{max}}^{\mathrm{disk}}$ and $a_{\mathrm{max}}^{\mathrm{env}}$ according to the range presented in Table 5.

Model fitting

To compare the model with the interferometric observations, we have to create images at the exact wavelengths of our observations. Subsequently, those model images have to be transformed to model visibilities. For that we used the computational library GALARIO (Tazzari et al., 2018). The model image is convolved with the primary beam patterns of the antennas and then Fourier transformed into visibilities.
The first step in this modeling is to fit the disk emission. We created a grid of parameters varying $\mathrm{M}_{\mathrm{disk}}$, R_{out} and a_{max} to reproduce together $F_{\mathrm{disk}}^{1.3\mathrm{mm}}$ and $F_{\mathrm{disk}}^{2.7\mathrm{mm}}$. Once we found the three parameters that match $\mathrm{F}_{\mathrm{disk}}^{1.3\mathrm{mm}}$=63.97 mJy and $\mathrm{F}_{\mathrm{d}}^{2.7\mathrm{mm}}$=18.8 mJy, we implement these output fluxes (output spectrum) as the heating central source of the envelope.
Using RADMC-3D (Dullemond et al., 2012), we then vary M_{env} and $a_{\mathrm{max}}^{\mathrm{env}}$ in order to reproduce the interferometric fluxes at 1.3 and 2.7 mm. Table 2.5 gives a complete list of model parameters and indicates whether they are fixed or varied. In Fig. 2.6 we present the best fit for the observed visibilities at both wavelengths. The set of parameters that provided the best match with the observations is presented in Table 2.6. The two best fits are discussed in the following section.

Results from the two step model

The parameters that provide a good fit respect to the disk emission at both wavelengths are reported in Table 2.6. The model M1 with a 32 au disk radius and $M_{\mathrm{disk}} = 0.4\mathrm{M}_{\odot}$ is consistent with the rescaled values reported by Segura-Cox et al. (2016). While all the disk models match the long baseline 1.3 mm data, the disk emission at 2.7 mm is 15% lower than the data. On the other hand, the disk model M2, with a 34 au disk radius and $M_{\mathrm{disk}} = 0.2\mathrm{M}_{\odot}$ matches very well the observations at both wavelengths, but compared

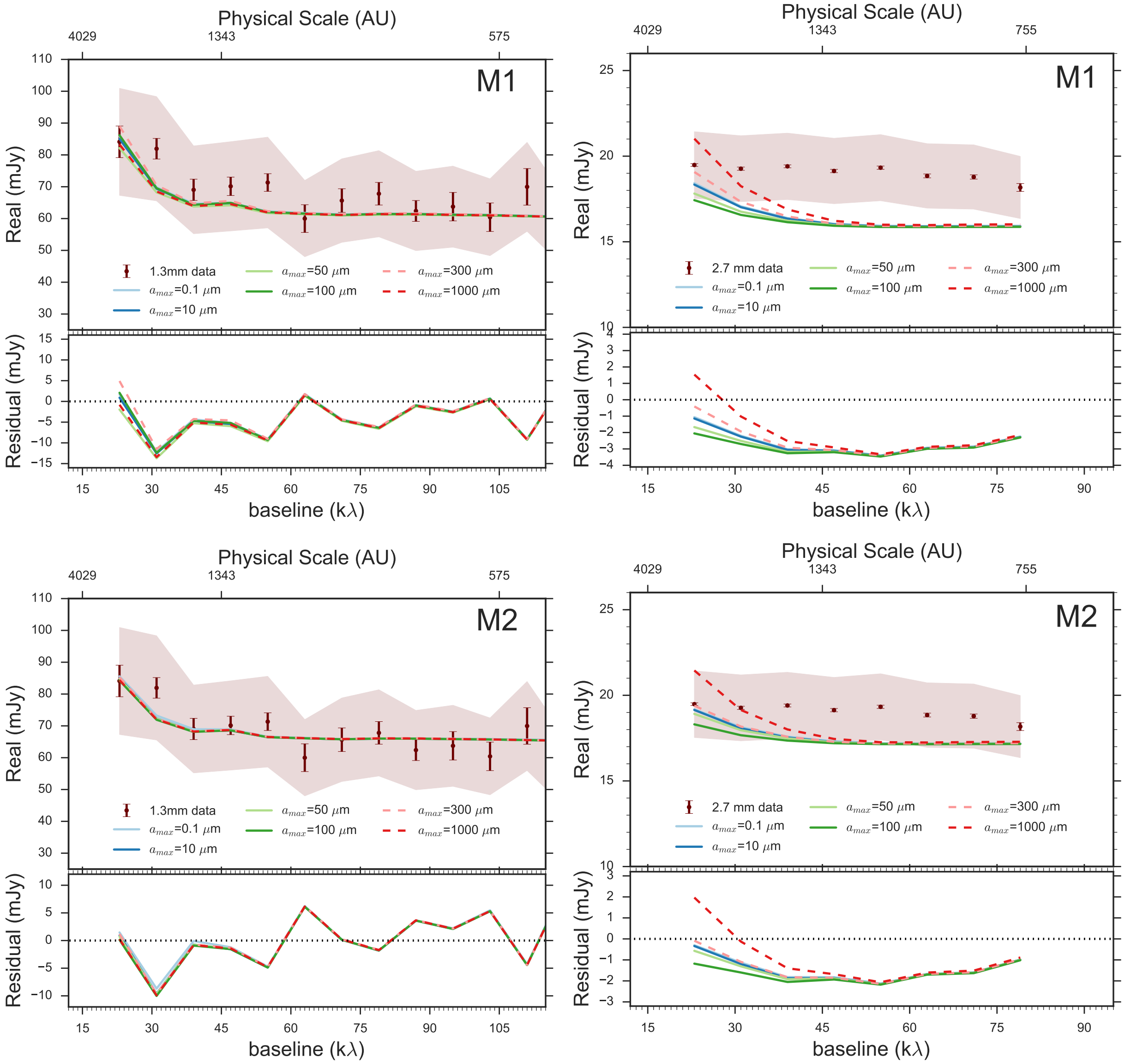

Figure 2.6: Real part of the visibilities as a function of baseline. Left panels are 1.3 mm data while right panels are 2.7 mm data. The two upper panels are models with the disk model M1 while the bottom panels present the models using disk model M2 (see Table 2.6). In solid lines we present models with grain sizes of $a_{\max} \leqslant 100$ μm. In dashed lines are models with grain sizes of $a_{\max}$ =300,1000 μm. The best fits are the models with a distribution of grain sizes with $a_{\max} \leqslant 100$ μm. The red shaded region is the uncertainty on the data due to flux calibration. The bottom of each panel shows the residuals between the data and the model with different $a_{\max}$.

with values of Table 5.1, the disk radius is slightly larger.

The differences in the disk models may be due to the assumed values of κ_ν= 0.00146 cm^2

Table 2.6: Two–step model best-fit parameters

Parameter	Description	Best–fit M1	Best–fit M2
Disk model parameters			
R_{out} (au)	Disk outer radius	32	34
M_{disk} ($M_{\odot}$)	Disk mass	0.4	0.2
Σ_{disk} (gr cm^{-2})	Disk surface density	554.13	245.38
$a_{\mathrm{max}}^{\mathrm{disk}}$ (μm)	Disk maximum grain size	10 000	10 000
RADMC-3D / Envelope parameters			
R_{rot} (au)	Centrifugal radius	600	600
ρ_0 (gr cm^{-3})	Density in the equatorial plane at R_{rot}	$<8.5\times10^{-20}$	$<6.0\times10^{-20}$
$a_{\mathrm{max}}^{\mathrm{env}}$ (μm)	Envelope maximum grain size	<100	<100

g^{-1} and disk temperatures of 20 K and 40 K in Segura-Cox et al. (2016). Therefore, higher-resolution millimeter observations that resolve the disk are needed to put much stronger constraints on Per-emb-50.

For the envelope, we explore the effects of changing R_{rot}, $a_{\rm max}$ and ρ_0. The envelope inner radius is fixed at the outer radius of the disk model. We tested different R_{rot} between 100 and 1000 au to accommodate the total enclosed envelope mass. As mentioned in Crapsi et al. 2008, decreasing the centrifugal radius results in more peaked and spherical envelopes. Using a small centrifugal radius has a significant influence on the amplitude at short baseline length. For example varying the centrifugal radius by a factor of two changes the first amplitude point of the model by 20%. We found that a $R_{\rm rot}$ of 600 au is consistent with the slope at short baselines in both wavelengths.
We can constrain the level of grain sizes in the envelope within the framework of the collapsing rotating envelope model. For example, in Fig. 2.6, if we consider a dust grain size distribution in the envelope with a maximum size of 1 mm, we can reproduce the 1.3 mm observations, but we underestimate the total envelope mass by a factor of six. In the case of models with $0.1\,\mu$m $< a_{\rm max} < 100\,\mu$m, the flux at 1.3 mm and 2.7 mm matches the observations very well, but the derived envelope masses differ from those derived from observations. The best match with the $2.2{\rm M}_{\odot}$ envelope mass derived by Enoch et al. (2009) are those derived from models with dust grain sizes of $a_{\rm max} \leqslant 50\mu$m (see Table 2.6). The models with $a_{\rm max} = 100\ \mu$m recover almost 60% of the envelope mass. Table 2.7 presents the derived masses for the envelope using different $a_{\rm max}$ in M1 and M2.
A distribution of grains with $a_{\rm max}\leqslant 50\ \mu$m provides a good match with the observations since the flat emission at 2.7 mm matches the observations well and is consistent with the systematic errors due the flux calibration.
Based on this model, the maximum grain sizes in the envelope are unlikely to be larger than a hundred microns. This would imply that the envelope may have gone through a process of grain growth, but there is no evidence that a substantial fraction of grains are large millimeter-sized dust aggregates.
As we mention before, the observed flux and spectral index of Per-emb-50 are consistent with a small optically thick disk, in which case, we cannot constrain the spectral index α. For the envelope we can use our dust model to infer the value of β, which is $\beta_{\rm env}$=1.46 and $\beta_{\rm env}$=1.63 for $a_{\rm max}$=10 and $a_{\rm max}$=50 μm, respectively. In Fig. 2.7 we compare the different β values for each a_{max} with the value obtained from the parametric model. The β values for $0.1\mu{\rm m} < a_{\rm max} < 100\mu$m are consistent, within the uncertainties, with the β calculated using the parametric model. In the case of grains larger than 100 μm, the total envelope mass is underestimated.

2.4.3 Full radiative-transfer model

In this model we used a system that consists of disk, protostar, envelope and outflow cavity. We used the radiative-transfer tool RADMC-3D from Dullemond et al. (2012) to compute the emission from all the contributions. The details of each contribution will be discussed

Table 2.7: Derived envelope masses

Model	$a_{\rm max}$ (μm)	$M_{\rm env}$ ($M_\odot$)
M1	0.1,10	1.73
	50	1.53
	100	1.15
	300	0.23
	1000	0.34
M2	0.1	1.22
	10,50	1.38
	100	0.85
	300	0.16
	1000	0.29

Note. Envelope mass calculated within 8 800 au radius

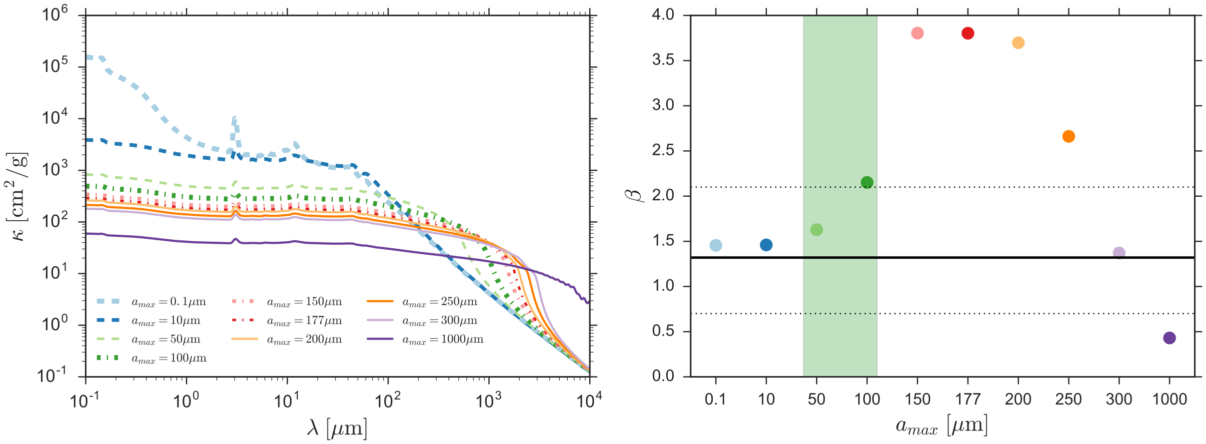

Figure 2.7: Left panel shows the dust absorption opacity as a function of wavelength for grain size distributions characterized by $(a) \propto a^{-3.0}$ and increasing maximum grain size ($a_{\rm max}$). Right panel shows the dust opacity spectral index (β) calculated between 1.3 mm and 2.7 mm wavelengths as a function of the maximum grain size. Black solid line is the $\beta_{\rm env}$ value from the parametric model and the black dashed lines are the uncertainties. Green region shows an upper limit for $a_{\rm max}$ in the envelope of Per-emb-50.

in the following sections.

Disk model

We adopt a disk model heated by its protostellar radiation. The surface density profile $\Sigma(R)$ was modeled as a truncated power law as in Eq. 4, with a power exponent of the surface density distribution p=1; Σ_0 is scaled to accommodate the total mass of the disk

$M_{\rm disk}$. The 2D volume density with an exponential vertical profile is defined by

$$\rho(r,z) = \frac{\Sigma(r)}{H_p\sqrt{2\pi}} \exp\left(-\frac{z^2}{2H_p^2}\right) , \tag{2.7}$$

where H_p is the pressure scale height and is defined as H_p/r=0.1(r/r_{h_p})$^{\phi}$, r_{h_p} is the reference radius set at 25 au, and ϕ is the flaring index of the disk, which in this case is set to 1.14, as an average value according to previous studies on young sources (Pineda et al., 2011; Tobin et al., 2013). We used the disk inclination angle, disk radius, and disk mass presented in Table 5.1.

Envelope model

For the envelope model we adopted a density profile by Tafalla et al. (2002), which combines a power-law behavior for large radius and a central flattening profile at small radius, that is,

$$n(r) = \frac{n_0}{1 + (r/r_0)^{\alpha}} , \tag{2.8}$$

where n_0 is the central density, r_0 is the radius of the flat region or truncation radius, and α is the asymptotic power index. The outer radius of the envelope is fixed at 8 800 au to match the beam of Enoch et al. (2009) observations, in which the rescaled envelope mass is 2.2 $M_{\odot}$. Additionally, since we have evidence of an outflow in this source (Stephens et al., 2017), we included an outflow cavity with an opening angle of 30° (M. Dunham, priv. comm.) and a lower density of 1.0×10^{-30} gr cm^{-3} for the region inside the cavity and the background.

Backwarming effect

The effects of the envelope thermal emission on disk (i.e., backwarming) have been studied in different environment, as in the case of the heavily embedded source L1551 IRS 5 (Butner et al., 1994).

In the case of an envelope around a disk, the millimeter emission of the disk increases. This is because the envelope acts as a thermal cavity, preventing the temperature within the cavity from falling below the temperature of the envelope wall. Therefore, a substantial backwarming effect on the disk can be present depending on the optical depth and geometry of the cavity.

In the previous envelope modeling following Miotello et al. (2014), this effect was ignored due the geometry of the envelope. Different profiles might heat the disk to a different degree. To explore the effects of backwarming we have computed new models which attempt to take it into account. The net effect of the envelope on the disk temperature is discussed in the Appendix B.4.

Table 2.8: Full radiative-transfer model grid parameters

Parameter	Description	Values	Parameter Use
Stellar model parameters			
$M_\star$ ($M_\odot$)	Stellar mass	2.9	fixed
$R_\star$ ($R_\odot$)	Stellar radius	5.0	fixed
$T_\star$ (K)	Effective temperature	5011	fixed
Disk parameters			
Σ_{bkg} (gr cm^{-3})	Background density	1.0×10^{-30}	fixed
$M_{\rm dust}/M_{\rm gas}$	Dust-to-gas mass ratio	0.01	fixed
R_{H_p} (au)	Reference radius at which H_p/R is taken	25	fixed
$m_{\rm disk}$ ($M_\odot$)	Mass of the disk	0.18–0.36	varied
ϕ	Flaring index	1.14	fixed
p	Power exponent of the surface density distribution	1.0	fixed
$r_{\rm out}$ (au)	Disk outer radius	25,27,30,32	varied
$r_{\rm in}$ (au)	Disk inner radius	1.0	fixed
$a_{\rm max}^{\rm disk}$(μm)	Disk maximum grain size	10000	fixed
Envelope parameters			
$R_{\rm out}$ (au)	Envelope outer radius	8,800	fixed
α	Power exponent of the radial density distribution	-1.1,-1.5,-1.8	varied
n_0 (gr cm^{-3})	Central density	$1.0, 1.5, 2.0 \times 10^{-16}$	varied
r_0 (au)	Within this radius the density profile is flat	25,27,30,32	varied
θ (°)	Opening angle of the outflow	30	fixed
$a_{\rm max}^{\rm env}$(μm)	Envelope maximum grain size	0.1–1000	varied

Note. Each model is calculated with 1×10^6 photons for the thermal Monte Carlo.

Dust opacity

We used two kinds of dust opacities in order to test the model. Firstly, we used the opacity computed in Ossenkopf & Henning (1994) based on a coagulated grain size distribution. In this model, a truncated power law is adopted for the initial dust distribution, n(a) $\propto a^{-q}$, where the minimum size of the grain is $a_{\rm min}$=5 nm, the maximum size is $a_{\rm max}$=250 nm and the power index q is set to 3.5. The dust distribution is calculated after 10^5 years of coagulation with a gas density of $n_{\rm H}$=10^5 cm^{-3} expected in a prestellar core. Secondly, we used the previous dust opacities presented in Section 4.2.3.

Since the second dust opacity approach covers maximum grain sizes from small grains of 0.1μm, to big grains of 1 cm, we decided to present here the results with those opacities to compare consistently with the previous modeling.

Model fitting

The free parameters for the disk are the outer radius, $r_{\rm out}$ and the disk surface density Σ_0. The free parameters for the envelope are its mass M_{env}, its power-law density profile α, its flattening envelope radius r_0, and its dust opacity, characterized by $a_{\rm max}^{\rm env}$. The truncation radius of the envelope is set at the outer radius of the disk parameter.

Since the disk parameters estimated by Segura-Cox et al. (2016) are not solid constraints, we test our model using their mass and outer radius values as an upper and lower limit on Σ_0. The grid of parameters that we test and set are presented in Table 2.8. Once the dust temperature of the system is calculated from the input parameters of Table 2.8, we compute the synthetic images, for 1.3mm and 2.7mm, following the same procedure reported in Section 4.2.4. We simultaneously fit the 1.3 mm and 2.7 mm visibilities by calculating χ^2 values for each model using the equation

$$\chi^2 = \sum_{i=1}^{N} \frac{(F_{\nu,{\rm observed},i} - F_{\nu,{\rm model},i})^2}{\sigma_i^2}, \qquad (2.9)$$

for the entire set of visibility points between 20 and 110 kλ. The uncertainty in the data, σ_i, includes the statistical uncertainty and the absolute flux uncertainty of 10% for 2.7 mm data and 20% for 1.3 mm data, both added in quadrature. Since our observational constraints are dominated by the errors of the data sets, it is possible that the disk and/or envelope structure could be inaccurate at some level. Therefore, our χ^2 value is simply an indicator of an acceptable model, not a best fit. After performing a visual inspection of the models, we report the best match with the observations in the following paragraph and in Table C.4.

A sample of models with different a_{max} and derived envelope masses is presented in the Appendix B.3.

Results from the full radiative-transfer model

From our interferometric observations, we are limited to studying the inner regions of the envelope, from 4 000 to 600 au. Therefore, we examine a power-law density profile following

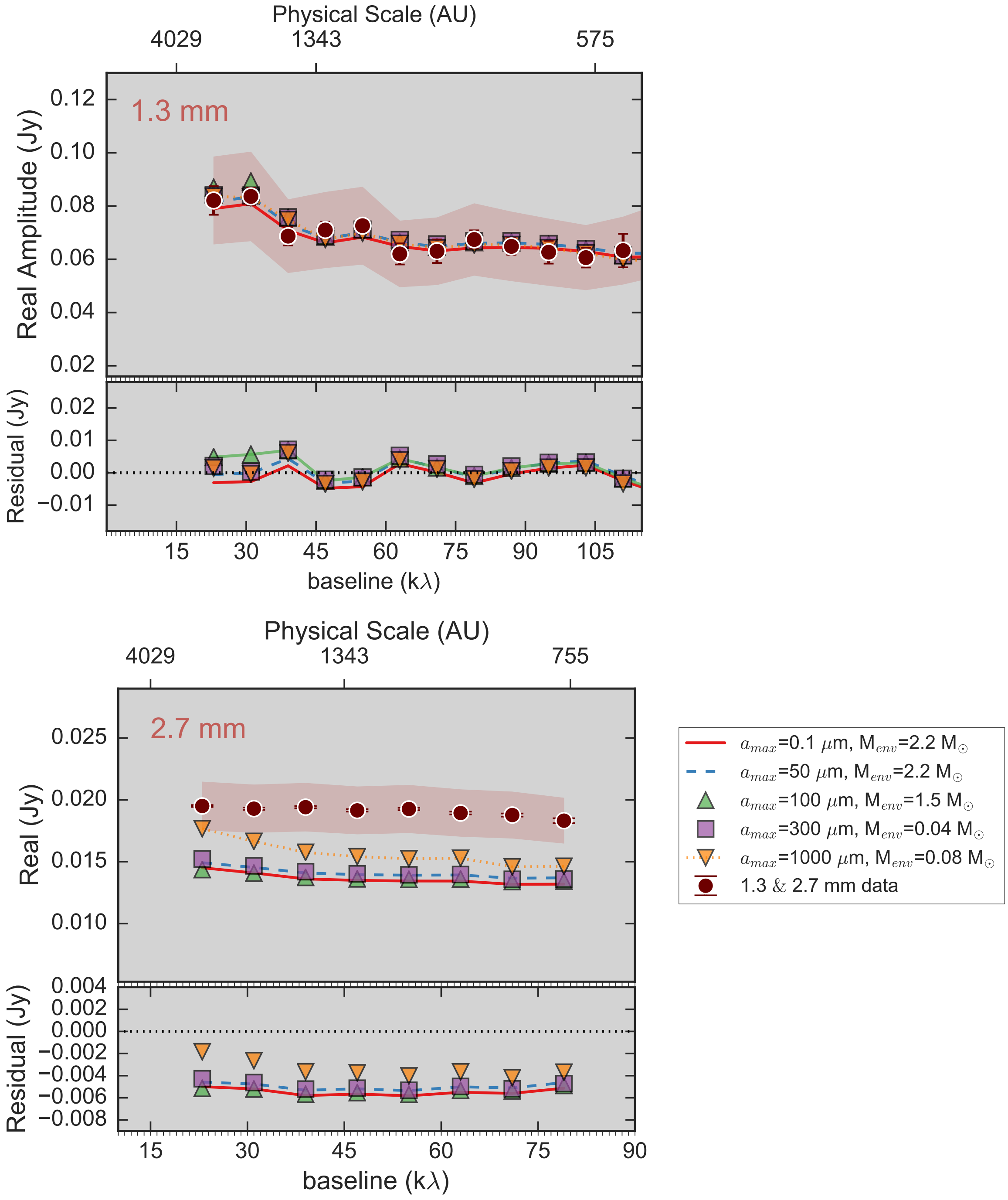

Figure 2.8: Real part of the visibilities as a function of the deprojected baseline. Upper panel shows 1.3 mm data while bottom panel shows 2.7 mm data. Red shaded regions are the uncertainties due the flux calibration. We show a variety of models with a maximum grain size in the envelope of $a_{\max} = 0.1, 50, 100, 300, 1000\ \mu$m. At the bottom of each panel are the residuals between the data and the best model.

Table 2.9: Full radiative-transfer best fit models

Parameter	Description	Best-Model 1	Best-Model 2
Disk parameters			
$\mathrm{m}_{\mathrm{disk}}$ ($M_\odot$)	Mass of the disk	0.20	0.24
Σ_{disk} (gr cm^{-2})	Disk surface density	362.2	364.2
r_{out} (au)	Disk outer radius	25	27
$a_{\mathrm{max}}^{\mathrm{disk}}(\mu\mathrm{m})$	Disk maximum grain size	10 000	10 000
Envelope parameters			
α	Power exponent of the radial density distribution	-1.1	-1.1
ρ_0 (gr cm^{-3})	Central density	2.0×10^{-16}	1.5×10^{-16}
M_{env} ($M_\odot$)	Envelope mass	2.24	1.54
r_{trun} (au)	Truncation radius	25	27
r_0 (au)	Within this radius the density profile is flat	25	27
$a_{\mathrm{max}}^{\mathrm{env}}(\mu\mathrm{m})$	Envelope maximum grain size	50	100

Tafalla et al. (2002). An unresolved component is included to represent a compact disk structure. In the envelope we used a constant dust grain population, in which we vary the maximum grain size from 0.1 to 1 000 μm. To study the impact of the maximum grain size in the envelope, $a_{\rm max}^{\rm env}$, the central density, n_0, and the density power law index, α, we used the range of parameters reported in Table 2.8.

Table 9 shows the model parameters that provides the best fits to the observations. For the disk properties, we compare our results with the values reported in Table 5.1. Our disk mass and radius are consistent with the rescaled values reported by Segura-Cox et al. (2016). Both disk models in Per-emb-50 are consistent with a small optically thick disk, but do not allow us to probe if there is grain growth throughout the disk since we are missing very long baselines to resolve the disk.

Similar to the results of the two-step model, the full radiative-transfer models suggest a distribution of dust grains in the envelope with maximum size $a_{\rm max}^{\rm env} = 50, 100$ μm and a resulting envelope mass within 8 800 au radius of $M_{\rm env}$~2.24, 1.54 M$_\odot$, respectively. In Fig. 8, we present a variety of models with different $a_{\rm max}$ in the envelope that match the visibility data. While all the models match the 1.3 mm data within the flux uncertainty (red region), the 2.7 mm data allow us to determine a good model because of the shape of the short-baseline emission.

Models with $a_{\rm max}^{\rm env} < 100$ μm follow the flat emission of the 2.7 mm data, while models with $a_{\rm max}^{\rm env} > 300\mu$m overestimate the short baseline emission at 2.7mm and underestimate the envelope mass of Table 5.1. These results are consistent with our previous modeling and in agreement with the spectral index β that we calculated in Fig. 2.7. We also reported the 1.1 mm single dish flux (see Table 2.10) for each model.

Table 2.10: Derived 1.1 mm fluxes and envelope mass

$a_{\rm max}$ (μm)	$M_{\rm env}$ ($M_\odot$)	$F_{1.1\,{\rm mm}}$ (Jy)
0.1	2.24	1.87
50	2.24	1.76
100	1.54	3.18
300	0.04	0.37
1000	0.08	0.35

Note. Each mass model is calculated within a 8 800 au envelope radius. The 1.1 mm fluxes are calculated using an aperture of 30", simulating the diameter aperture of Bolocam.

As discussed by many authors (Draine, 2006; Banzatti et al., 2011; Testi et al., 2014), it is quite difficult to explain values of β of less than 1 without invoking the presence of millimeter size grains, regardless of the chemical composition, porosity, or grain geometry. In the case of Per-emb-50, the high value of β is compatible with grains no larger than 100 μm, and with values found in Class 0 sources by I-Hsiu Li et al. (2017). The fact that we find grains that have not reached millimeter sizes in the envelope of Per-emb-50 is discussed in the following section.

2.5 Discussion

2.5.1 Grain sizes in Class I protostellar envelopes

The presence of millimeter-sized grains in envelopes of young protostars as Class 0/I, has been studied and modeled by many authors (e.g., Kwon et al. 2009; Chiang et al. 2012b; Tobin et al. 2013; Miotello et al. 2014), but current models cannot easily explain growth at that level (Ormel et al., 2009). This is because the models require high number densities, $n_{\rm H} > 10^6$ cm^{-3}, to form such large grains on timescales of 1 Myr.
Miotello et al. (2014) found that dust grains start to aggregate up to millimeter sizes already in the envelope of two Class I protostars, producing a change in the spectral index with values of β_{env}=0.6±0.3 for Elias 29 and β_{env}=0.8±0.7 for WL 12. Those values are smaller than the spectral index for the envelope of Per-emb-50, β_{env}=1.4±0.3, by a factor of two. The differences between these studies may be associated with the properties of the star-forming region. In our case, Per-emb-50 is in the NGC1333 region in Perseus, which is a very crowded region with young stellar objects, while the sources of Miotello et al. (2014) are isolated and embedded in L1688 in Ophiuchus. With this study on Per-emb-50, we suggest the possibility that: (a) millimeter grains in envelopes of young protostars may not be a common result, or (b) the dust grain growth is not a homogeneous process. Finally, the environment within which a protostar forms could also play a role in the amount of dust coagulation, which significantly affects the future formation and structure of the protoplanetary disk, as shown by Zhao et al. (2016, 2018).

The possibility that grains can grow up to millimeter sizes in the envelope of Class 0/I protostars was studied by Wong et al. (2016). They proposed another mechanism to explain the existence of millimeter-sized grains in the envelopes of young protostellar sources that consists of transport of millimeter-sized grains from dense regions close to the protostar to the envelope via the outflow. This scenario is quite plausible before the central mass of the protostar reaches a mass of 0.1 $M_\odot$ with a mass-loss rate of 10^{-6} $M_\odot$ yr^{-1}. This could be the case for Per-emb-50, but high-resolution data are needed to model the inner regions of this source.
The results of our analysis show that dust grains may have grown as large as $\sim$100 μm in size in the envelope of Per-emb-50 at scales of 4000-2000 au. This implies that there is a degree of grain growth with respect to the ISM sizes, but not significant enough to lower the value of α. This is also in agreement with the work of Chacón-Tanarro et al. (2017), where they predict grain sizes of a few hundred μm in the central 300 au of the prestellar core L1544.

Taking this into account, it is crucial to perform surveys for Class I protostars embedded in different environments and at different physical scales to determine the variation of α spectral index and the corresponding amount of grain growth.

2.5.2 The effects of backwarming

We find that backwarming is important for modeling Per-emb-50. From the previous analysis, using the two-step modeling, it was straightforward to fit the nearly constant emission at long baselines with an unresolved disk. For the full radiative-transfer modeling, however, this was not the case. Considering the full radiative-transfer model, the use of a Tafalla et al. (2002) density profile combined with a power-law behavior for large radius and a central flattening profile at small radius shows that backwarming is important since the disk emission is completely affected by the addition of the envelope. This change in emission is discussed in Butner et al. (1994) and in the Appendix B.7. To study the effects of different envelope geometries on disk emission is beyond the scope of this work.

However, backwarming can have other consequences. The change of temperature between a backwarmed disk (∼100 K) and a nonbackwarmed disk with ∼20 K, would significantly affect the gas phase chemistry and the dust mantle chemistry in young disks and envelopes (Butner et al., 1994). Finally, the backwarming in Class I protostars could have an important effect on the thermal history of the outer disks of planetary systems. Detailed studies using proper physical structures and radiative-transfer models are necessary to address the backwarming effect present in most young embedded sources.

2.6 Conclusions

We present new 1.3 mm data from SMA and 2.7 mm data from NOEMA of the brightest Class I protostar Per-emb-50 in the NGC 1333 cluster in the Perseus star-forming region. In the u–v plane it is possible to distinguish the presence of a large-scale envelope at short baselines and an unresolved and optically thick disk at longer *u*-*v* distances. From the data analysis and the different modeling approaches on this source we can make the following conclusions:

- For the envelope uv analysis we find a spectral index similar to the typical (α_{mm}=3.7) ISM values, $\alpha_{\mathrm{mm}}=3.3\pm0.3$.

- The current observations on Per-emb-50 and the radiative-transfer modeling reveal a Class I envelope consistent with maximum sized grains of $< 100\ \mu$m. This suggests that grain growth has proceeded within the envelope, but not far enough to produce changes in α as the presence of millimeter-sized grains does.

- The presence of grains with a size range of $<100\ \mu$m in envelopes of Class I protostars may have an impact on our understanding of protostellar evolution. Following the prediction from Chacón-Tanarro et al. (2017), who find that dust grains are expected to grow to sizes of a few hundred micrometers in the central 300 au of a pre-stellar core, we could suggest that the larger grains found in the envelope of Per-emb-50 may be inherited from the prestellar phase.

- These results show for the first time no evidence of grain growth to millimeter sizes in the inner regions of the envelope of a Class I protostar, providing an interesting case for future studies of the efficiency of the grain-growth process in these stages.

- We also explore the effects of backwarming. The analysis shows that the envelope geometry highly affects the disk temperature. In the collapsing envelope model, the effect is weak, but if a power-law envelope is used, the effect is more obvious.

Future high-sensitivity data will be needed to allow us to conclude on whether or not there are spectral index variations between the disk and the envelope. Moreover, the study of a larger sample of Class I sources in different star-forming regions is important to understand how general this process is for grain growth.

Chapter 3

Dust grain size constraints in envelope-disk scales of the Class I protostar Per-emb-50

The content of this chapter has been submitted to A&A

C. Agurto-Gangas, L. Szűcs, Dominique M. Segura-Cox, J.E. Pineda, P. Caselli. L. Testi

3.1 Overview

The growth of millimeter or centimeter size solids in cores and envelopes is not straightforward. Ormel et al. (2009) studied the grain growth in cores, finding that little coagulation can be expected within the free-fall time and only if additional support mechanisms are present (e.g. ambipolar diffusion, freezeout of ice) dust aggregates of a few hundreds microns may be produced. However, while it is easy to grow dust to micron size particles, the growth from millimeter and centimeter size dust to meter size pebbles is currently under debate. Observational constraints of the grain growth process in protostellar envelopes and disks are thus needed to test our understanding of dust evolution. Especially critical is to map the level of growth in the various regions of a protostellar system: outer core, inner infalling envelope and disk. Understanding the process of dust accretion from the envelope to the inner regions may help us to reveal which regions lead the growth of dust to form grains beyond mm sizes and the building blocks of future planetesimals.

From an observational point of view, young stellar objects (YSOs) can be divided into three classes. Lada & Wilking (1984) define two classes by their IR-slope in the spectral energy distribution (SED), Class I YSOs and Class II YSOs. This SED slope classification can be interpreted as an evolutionary sequence, in which the Class I phase is a protostar surrounded by an accretion disk plus an envelope that is being rapidly dissipated, while the Class II stage consists of a pre-main sequence star in the optical, a dissipated envelope and a dense disk, which is optically thick in the IR but optically thin in (sub-)mm wavelengths. Class 0 sources were added later by André et al. (1993) based on their (sub-)mm continuum morphology and characterized by low ratios between bolometric and (sub-)mm luminosities.

Classical protoplanetary disks (in Class II YSOs) present clear signs of dust growth, with evidence of millimeter-size grains. Changes in the millimeter spectral index $\beta_{\rm mm}$ of the dust opacity ($\kappa_\nu \propto \nu^\beta$, can be used as a tracer for grain growth. In this context, large β-values are associated with the presence of small grains (μm to mm size), while values of $\beta \leqslant 1$ are a signature of grains larger than 1 mm (Natta & Testi, 2004). In Pérez et al. (2015) and Tazzari et al. (2016a), where protoplanetary disks have been studied as a function of the distance from the star, a value of $\beta_{\rm mm} < 1$ has been found in the inner disk (<100 au) and $\beta_{\rm mm} \sim 1.7$ towards larger radii. This is part of the radial drift effect Birnstiel et al. (2010), which means that large grains ($>$ mm sizes), less coupled with the gas than small grains ($< 1\,\mu$m), migrate inwards more quickly. In terms of dust dynamics, a small particle with a small Stokes number ($\mathrm{St} \ll 1$) will be coupled or tight to the gas, while a large particle with large Stokes number ($\mathrm{St} \gg 1$) will be less affected by the gas drag (small surface to mass ratio) and therefore move on Keplerian orbits (Schräpler & Henning, 2004). While evidence of dust grain growth is clear in the evolved Class II phase, properties of dust grains in the early stages of star formation remains unknown.

Toward pre-stellar cores, the evidence is less clear: recent studies (e.g. Chacón-Tanarro et al., 2019) predict dust grains of 3–4 μm in size within the central 2000 au of L1544. These sizes are about ten times bigger than standard interstellar medium (ISM) grains (average size of $\sim$0.1 μm in radius (Mathis et al., 1977)). Nevertheless, this is still under debate. Pagani et al. (2010) found evidence of large (micrometer-sized) grains through observations at 3.6 μm in dense cloud cores, via the coreshine effect. This interpretation has been discussed by Jones et al. (2013) and Jones et al. (2016), suggesting that amorphous hydrocarbon material could actually produce the observed coreshine without the need of large, micrometer-sized grains.

Some evidence of grain growth has been collected towards Class 0 envelopes (e.g Jørgensen et al., 2007; Kwon et al., 2009; Chiang et al., 2012a; I-Hsiu Li et al., 2017; Galametz et al., 2019). In these studies an average value of dust emissivity index of 1.0 is observed, but at these early stages the analysis of dust properties are complicated by the presence of both significant mass in the envelope and jet emission (e.g. Tobin et al., 2010). In addition, I-Hsiu Li et al. (2017) shows that for their sample of 9 Class 0 sources, different analyses exhibit alternative interpretations. While a single-component modified blackbody fits 4 of their 9 SEDs with spectral index $\beta < 1.0$, a radiative transfer model assuming $\beta = 2.0$ shows that their same 4 SEDs with lower spectral indexes can be interpreted by the presence of hot inner dust components that are obscured by the cooler and optically thicker outer components at short mm wavelengths. Thus, large uncertainties affect measurements of the dust spectral index β toward Class 0 sources.

Analyzing dust properties in Class I protostars is easier compared to Class 0 sources because the surrounding envelope is less massive, and it is more straightforward to separate the disk from the envelope contribution in the visibility domain. However, only a few Class I protostars have been studied to constrain the dust properties from envelope to small scales. Miotello et al. (2014) found grain growth up to millimeter sizes in envelope and disk of two Class I protostars. They derived a value of $\beta \approx 1$, implying the presence of millimeter grains, which is consistent with the values found in protoplanetary disks. Additional studies as Sheehan & Eisner (2017) and Sheehan & Eisner (2018), with a sample of 11 Class I protostars in Taurus and in ρ Ophiuchus, have found that dust can grow until cm-sizes in the disk.

There has been recent debate about grain sizes in the Class I phase and whether they are always consistent with Class II grain sizes; moreover, the question of the relation between envelope and disk grain populations is yet to be addressed.

Recently we studied the dust emission of the Class I protostar Per-emb-50 (Agurto-Gangas et al., 2019), finding that grains have grown to a maximum grain size of 100 μm in the inner envelope (3000–1000 au). We fitted observations taken at two wavelengths with three models of increasing complexity. We first tested a simple model where the observed emission in the visibility plane is treated as an unresolved disk and a Gaussian envelope. This allows us to disentangle the emission of the disk and the envelope components and determine the spectral index for each component. We found a spectral index in the envelope of β=1.7, that is consistent with ISM dust. We also analyzed Per-emb-50 with more detailed dust radiative-transfer models. Both radiative transfer based models, one of which is comparable to the modelling approach of Miotello et al. (2014), suggest that the maximum grain size in the envelope, $a_{\max}$, is less than 100 μm. Although these sizes are consistent with grain growth compared to the ISM dust, they are significantly smaller than the millimeter-size grains deduced toward two Class I sources in Ophiuchus by Miotello et al. (2014). While we could constrain relatively well the envelope parameters with the physical scales of our observations, the disk properties could not be constrained.

In this study we complement the previous observations on Per-emb-50 with the high angular resolution data from the VANDAM survey (Segura-Cox et al., 2016, 2018) to determine disk properties and to further separate disk and envelope emission in order to obtain information on the grain size distribution in the two components.

The work we present here combines interferometric data that probe both the disk and envelope with radiative transfer methods to form a holistic picture of the continuum properties of Per-emb-50. The observational data used in this work are briefly introduced in Section 2. The modeling is described in Section 3. In Section 4 we report the results from the model for the disk and envelope. In Section 5 we discuss the best models and physical properties compared with previous studies, and in Section 6 we present our conclusions.

3.2 Observations

The multi-wavelength continuum maps available for Per-emb-50 are presented in Fig. 3.1. The observations were obtained with the SMA (Submillimeter Array), NOEMA (Northern

Table 3.1: Observing information at 1.29

Source Name	SMA track name	Array configuration
Per-emb-50	141127_02:21:26	SUB
	150224_04:47:03	EXT
	150224_05:33:03	EXT
	150915_10:07:22	EXT

Per-emb-50 observations from the MASSES legacy program (Mass Assembly of Stellar Systems and their Evolution with the SMA, PI: I.W. Stephens, M. Dunham; e.g., Stephens et al., 2018, 2019).

Extended Millimeter Array) and VLA (Jansky Very Large Array) observatories.

3.2.1 SMA and NOEMA observations

In this analysis of Per-emb-50 ASIC (Application Specific Integrated Circuit) tracks are used. In Table 3.1 details about the SMA observations are presented. A combination of subcompact and extended array configurations are used to create a line free continuum, with projected baselines in the range of 3–160 kλ. The reported 1.29 mm continuum synthesized beam is 1.2" × 0.9" at position angle, P.A. 85°. We consider an absolute flux uncertainty of 15% Andersen et al. (2019).

Additionally we use 2.72 mm data[1] that were obtained with NOEMA, the IRAM[2] NOrthern Extended Millimeter Array. The continuum visibilities were generated from the WideX (Wideband Express) correlator units, avoiding channels in which line emission was detected. The continuum map was produced using natural weighting and the resulting synthesized beam size is 2.1" × 1.6" at P.A. 34.84°. The 2.72 mm data has an absolute flux uncertainty of 10%.

We also check for any free-free emission that can significantly contribute to the continuum at 2.72 mm. For that purpose we used the fluxes at 4.1 cm and 6.4 cm reported in Tychoniec et al. (2018). The extrapolated flux at 2.72 mm from the 6.4 cm is given by:

$$F_{2.72\mathrm{mm}}^{\mathrm{extr}} = F_{6.4\mathrm{cm}} \left(\frac{109\,\mathrm{GHz}}{4.7\,\mathrm{GHz}} \right)^{0.462} \quad . \tag{3.1}$$

The contribution of the free-free emission at 2.72 mm is 0.47 mJy, which is close to 2.3% of the average flux value of the disk visibilities (~ 20 mJy).

---

[1] Based on observations carried out under project number S16AT with the IRAM NOEMA Interferometer. IRAM is supported by INSU/CNRS (France), MPG (Germany) and IGN (Spain).

[2] http://www.iram-institute.org/

Table 3.2: Extrapolated free-free flux contamination at 2.72

Source	$F^{extr}_{2.72mm}$ (mJy)	$F^{extr}_{8.12mm}$ (mJy)
Per-emb-50	0.47±0.3	0.28±0.1

The extrapolated fluxes are calculated using the integrated 6.4 cm flux, resulting from a 2D Gaussian fit to the source and the spectral index, reported in Table 3 of Tychoniec et al. (2018). The error of the flux extrapolations are calculated using standard error propagation and considering the error associated with the spectral index.

3.2.2 VLA observations

Per-emb-50 was observed within the VLA Nascent Disk and Multiplicity (VANDAM) survey at 8.12 mm and 10.5 mm (Tobin et al., 2015; Segura-Cox et al., 2016). The resolution of the survey is 65 au for B-array and 12 au in the A-array configuration. For the aim of this work we are using the 8.12 mm data for the model fitting procedure and the 10.5 mm data as a comparative wavelength for the best model. The projected baselines used in this work are in the range of 50–2000 kλ, which translates in physical scales of ∼1200 au to 30 au. The 8.12 mm data-set is produced by merging both A- and B-configuration observations using the *concat* task of CASA[3] and then multi-frequency synthesis imaging mode was used. More details are in Tobin et al. (2016). The observations were performed during 2013 and 2015 and were made in three-bit correlator mode, with a total bandwidth of 8 GHz divided into 64 sub-bands. Each sub-band has 128 MHz bandwidth, 2 MHz channels, and full polarization products. The two 4 GHz basebands are centered at 36.9 GHz (∼8.12 mm) and 29.0 GHz (∼10.5 mm). The quasar 3C48 was used as the flux calibrator, while 3C84 was the bandpass calibrator. J0336+3218 was observed to perform the complex gain calibration. The expected uncertainty in the absolute flux calibration is 10 %. The observations were calibrated using the VLA calibration pipeline within CASA (version 4.1.0) and the VLA pipeline version 1.2.2.

The free-free emission contamination was estimated at 8.12 mm as described above (Section 2.1, see Table 3.2). In this analysis we do not model the 10.5 mm data-set due the large uncertainties presented in the visibilities.

3.3 Modeling

The modeling is separated into two steps. First, the disk is modeled using the VLA and SMA data-sets, because these cover resolved and unresolved disk emission. In the second step of the modeling, we use the best disk fit parameters from the first step and then the envelope model is fitted. For that purpose, we use the data-sets that cover the envelope region (SMA & NOEMA). The method and the model grid are described below.

The modeling presented here, including the envelope density profile and the dust distri-

---

[3] `https://casa.nrao.edu/`

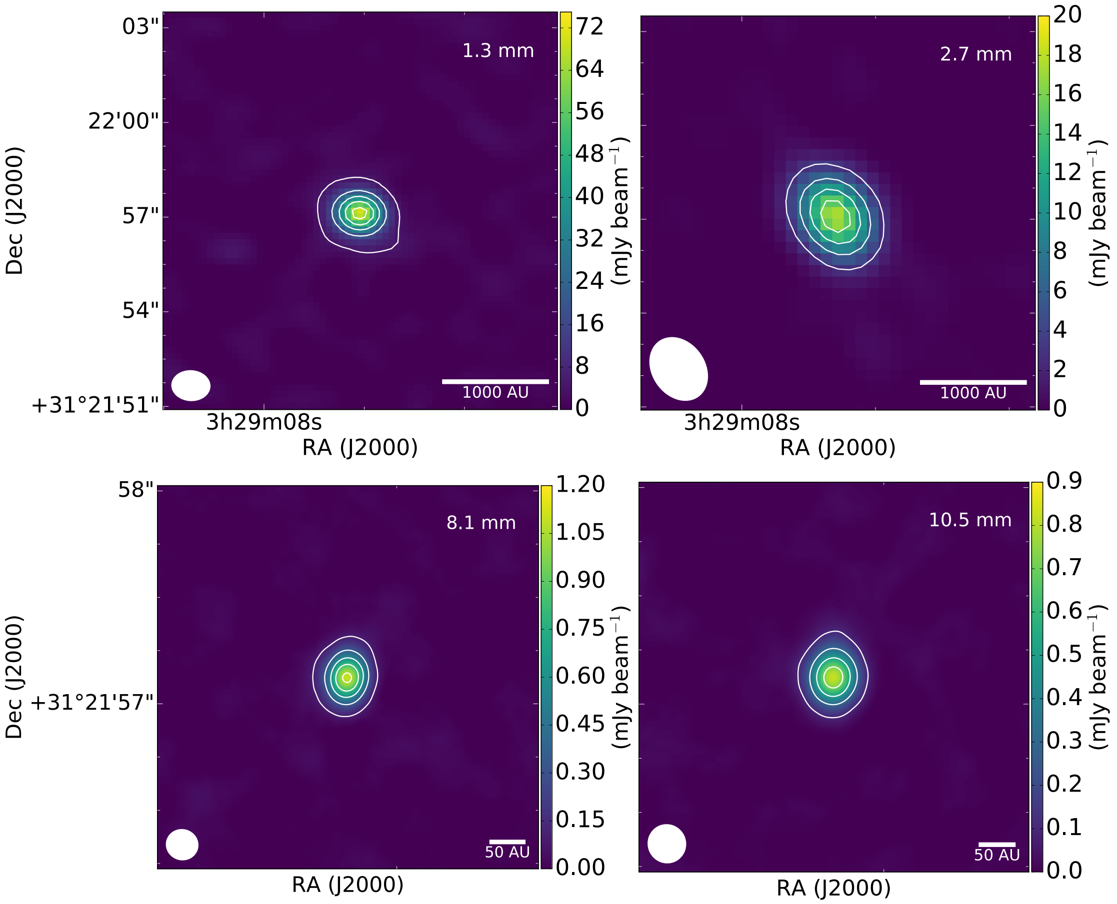

Figure 3.1: Continuum map of Per-emb-50 at 1.29 mm (SMA), 2.72 mm (NOEMA), 8.12 and 10.5 mm (VLA) wavelengths. For SMA and NOEMA data, the contours start at 76 and 20 mJy per beam, respectively, and both increase in 25% intervals. The contours in the 8.12 mm and 10.5 mm images start at 1σ and increase in $[3,5,8] \times \sigma$, where σ=0.1 mJy. The synthesized beam FWHM is represented as a white ellipse in the bottom-left corner of each map.

bution power law, are slightly different from Agurto-Gangas et al. (2019), and it will be discussed and compared in the following sections.

3.3.1 Model components

The model includes a central protostar surrounded by a disk and an envelope with an outflow cavity. Details of the structure of each component and the parameters that were varied to create our grid of models are presented bellow.

Protostar

We adopt the protostellar parameters presented in Agurto-Gangas et al. (2019), with a central protostar with an effective temperature of 5000 K and with a photosphere luminosity of 13.7 $L_\odot$. The majority of Class I sources are low-mass protostars which will evolve into K- or M-type spectral types (White & Hillenbrand, 2004), so a temperature of 5000 K is a reasonable assumption.

Envelope

For the envelope model, we adopt the density profile for a rotating collapsing envelope from Ulrich (1976),

$$\rho_{\mathrm{env}}(r,\theta) = \rho_0 \left(\frac{R_{\mathrm{rot}}}{r}\right)^{3/2} \left(1 + \frac{\cos\theta}{\cos\theta_0}\right)^{-1/2} \left(\frac{\cos\theta}{2\cos\theta_0} + \frac{R_{\mathrm{rot}}}{r}\cos^2\theta_0\right)^{-1} , \tag{3.2}$$

where ρ_0 is the density in the equatorial plane at the centrifugal radius R_{rot} of the envelope, and θ_0 is the solution of the parabolic motion of an infalling particle given by:

$$\frac{r(\cos\theta_0 - \cos\theta)}{(R_{\mathrm{rot}}\cos\theta_0\sin^2\theta_0)} = 1 \, . \tag{3.3}$$

At large radii the density distribution tends towards spherical symmetry, while within the rotational radius the density is enhanced along the plane perpendicular to the rotational axis. Inside R_{rot}, the envelope radial density profile is proportional to $r^{-1/2}$, while outside R_{rot}, $\rho_{env} \propto r^{-3/2}$.
Additionally, since there is evidence of an outflow in this source (Stephens et al., 2017), we included an outflow cavity with an opening angle of 30° (M. Dunham, priv. comm.), and the cavity is assumed to be empty. The outer radius of the envelope is given by the size of 1.1 mm Bolocam observations (Enoch et al., 2006) and is fixed at 4400 au. The inner radius of the envelope is set to the radius of the disk.

Disk

We adopt a surface density profile given by a flared power-law disk defined by:

$$\rho(r,z) = \frac{\Sigma(r)}{H_{\mathrm{p}}\sqrt{2\pi}} \exp\left(-\frac{z^2}{2H_{\mathrm{p}}^2}\right) , \tag{3.4}$$

where $\Sigma(r)$, the surface mass density profile, is modeled as a truncated power law given by:

$$\Sigma(r) = \Sigma_0 \left(\frac{r_{\mathrm{disk}}}{r_{\Sigma_0}}\right)^{-p} , \tag{3.5}$$

with a power law of the surface density distribution p. The central density, Σ_0, is scaled to accommodate the total mass of the disk. r_{disk} is the outer disk radius and r_{Σ_0} is the radius at which the surface density normalisation Σ_0 is given. H_p is the pressure scale height and is defined as $H_\mathrm{p}/r = 0.1(r/r_{\mathrm{H_p}})^{\phi}$, $r_{\mathrm{H_p}}$ is the reference radius set at 25 au, and ϕ is the flaring index of the disk, which in this case is set to 1.14, as an average value according to previous studies on young sources (Pineda et al., 2011; Tobin et al., 2013). The inner radius of the disk is fixed at 1.0 au.

3.3.2 Opacity

The optical properties of the dust grains are calculated using the Bruggeman mixing rule. We fixed the chemical composition to a mixture of water, carbonaceous material and silicate in a 6:3:1 volume fractional ratio (Natta & Testi, 2004; Ricci et al., 2010c). Following Miotello et al. (2014) setup we set the minimum grain size, a_min, to 0.1 μm, for envelope and disk dust. As long a_min is lower than 1μm (Testi et al., 2014) the dependence of the millimeter dust opacity is very weak. Absorption and scattering opacities are determined assuming that the grains are spherical and using the radmc3dPy implementation based on the BHMIE code (Bohren & Huffman, 1983). We assume a power-law grain size distribution with a slope of $q = 3.5$ for both the disk and envelope dust populations.

3.3.3 Free model parameters

Our radiative transfer model includes a large number of free parameters. Specifically, four and three parameters for the disk and envelope, respectively. Section 3.3.1 describes the parameters that are fixed, while the ranges of parameters explored for the disk and envelope are based on previous studies that include physical information on Per-emb-50 (Agurto-Gangas et al., 2019; Stephens et al., 2019; Andersen et al., 2019).
The VANDAM data (Segura-Cox et al., 2016, 2018) reveal some disk properties, such as radius and mass at small scales; however, a study that combines multi-wavelength mm observations and multi-scale analysis in this source has yet to be done. We create two model grids, one for the disk and one for the envelope. For the disk component we varied disk density power law (p), disk mass (M_disk), disk radius (r_disk) and the disk maximum grain size ($a_\mathrm{max}^\mathrm{disk}$). In the case of the envelope fit, rotational radius (R_{rot}), central density (ρ_0) and envelope maximum grain size ($a_\mathrm{max}^\mathrm{env}$) are free parameters. We also set the inner radius of the envelope equal to the radius of the disk.

3.3.4 Radiative transfer model and synthetic visibilities

We use the Monte Carlo radiative transfer modeling code RADMC-3D (Dullemond et al., 2012). The radiative transfer code calculates the dust temperature in our model by propagating photon packets and updating the temperature when a photon is absorbed and then re-emitted. We compute a synthetic image of the model, one per wavelength, and then we sample their Fourier transform at the u locations of the observed visibilities. We use GALARIO for this purpose (Tazzari et al., 2017). Additionally, to speed-up the raytracing of the large images, we modify the image sizes suggested by GALARIO. Since the image size is usually larger than the physical scales that we are interested in modeling and is inefficient, a new image is created in order to conserve the original image resolution in terms of au and pixel size (au/px), but it will cover a smaller image size, requiring less computational time. This modification translate to a reduction of image time calculation of 20% for 1.29 and 2.72 mm data-sets and 80% for the 8.12 mm data-set. More details about this implementation are presented in Appendix C.1.

3.3.5 Fitting procedure

The fitting procedure is divided into two steps. First, the disk parameters (p, M_{disk}, r_{disk} and $a_{\mathrm{max}}^{\mathrm{disk}}$) are explored with a grid size of 6×16×16×17 models, respectively. We explored the power exponent of the surface density distribution, p, which allow us to vary the amount of mass within the disk. Usually this parameter is fixed to 1.0 while in our discrete grid we use values between 1.0 and 4.0. A total of 26,112 models were created for the disk parameter space exploration. Secondly, with the best disk model a second grid of models is computed for the envelope parameters (R_{rot}, ρ_0 and $a_{\mathrm{max}}^{\mathrm{env}}$). The size of the envelope grid is 16×16×12, giving a total of 3,072 models.
We select the best model by binning the data and model synthetic visibilities and then calculating the χ^2 as:

$$\chi^2 = \sum_{j=1}^{N} w_j \left\{ \left[\mathrm{Re}\left(V_{\mathrm{obs}\,j}\right) - \mathrm{Re}\left(V_{\mathrm{mod}\,j}\right)\right]^2 + \left[\mathrm{Im}\left(V_{\mathrm{obs}\,j}\right) - \mathrm{Im}\left(V_{\mathrm{mod}\,j}\right)\right]^2 \right\} \tag{3.6}$$

where V_{mod} are the synthetic visibilities of a model image at the specified $(u,)$ locations of the observations and V_{obs} are the real and imaginary components of the data. w_j are the weights associated to the observed visibilities and re-scaled to be consistent with the real observed average dispersion in the measurements. More details about the weights are presented in Appendix C.2. The limits for each parameter in the grid are presented in Table 3.3. The limits were chosen creating radiative transfer models with those values and performing a visual inspection of the model visibilities, and following previous parameters exploration in Agurto-Gangas et al. (2019); Segura-Cox et al. (2016, 2018).

3.4 Results

The criterion used to find the best set of disk and envelope parameters to match small and large scale emission simultaneously is described below. The comparison between the best model and the models created with the upper and lower limits of Table 3.3 is in Appendix C.4.

3.4.1 Disk results

For the disk model fit we considered the 8.12 mm and 1.27 mm data-sets. The disk emission and size is well covered at VLA wavelengths while the SMA data-set probes the unresolved

Table 3.3: Model set up exploration

Grid	Parametera	Unit	Limits
Disk			
	M_{disk}	($\mathrm{M}_{\odot}$)	5×10^{-5} – 0.005
	r_{disk}	(au)	20 – 100
	$a_{\mathrm{max}}^{\mathrm{disk}}$	(μm)	100 – 10000
	p		1.0 – 4.0
Envelope			
	ρ_0^{env}	($\mathrm{g\,cm^{-3}}$)	1×10^{-19} – 1×10^{-17}
	R_{rot}	(au)	38 – 1000
	$a_{\mathrm{max}}^{\mathrm{env}}$	(μm)	5 – 200

aParameter description: (p) disk density power law, (M_{disk}) disk dust mass, (r_{disk}) disk outer radius, (ρ_0^{env}) envelope central density, (R_{rot}) envelope rotational radius, ($a_{\mathrm{max}}^{\mathrm{disk}}$) disk maximum grain size and ($a_{\mathrm{max}}^{\mathrm{env}}$) envelope maximum grain size.

disk emission at shorter wavelengths. Both data-sets are needed to calculate the dust spectral index, and therefore, to constrain dust properties. The use of both data-sets is also supported by the results of Andersen et al. (2019) who found a strong linear correlation between the data sets, suggesting that disk masses can be measured from unresolved observations. All the models at 8.12 mm take into account a freefree point-source component of 0.28 mJy and a provisional set of fixed envelope parameters of $\rho_0^{\mathrm{env}}= 1\times10^{-19}\,\mathrm{g\,cm^{-3}}$, $R_{\mathrm{rot}}=r_{\mathrm{disk}}$ and $a_{\mathrm{max}}^{\mathrm{env}} = 25\,\mu$m based on Agurto-Gangas et al. (2019).
The best disk parameters are calculated using:

$$\chi^2_{\mathrm{red}} = \frac{\chi^2_{\mathrm{VLA}} + \chi^2_{\mathrm{SMA}}}{(N_{\mathrm{bin,VLA}} + N_{\mathrm{bin,SMA}}) - N_{\mathrm{free}}} \tag{3.7}$$

where χ^2_{SMA} and χ^2_{VLA} are the χ^2 for each data-set, $N_{\mathrm{bin,VLA}}$ and $N_{\mathrm{bin,SMA}}$ are the number of binned data, which is 35 and 57, respectively. N_{free} is the number of free parameters. The 2.72 mm data-set is used as comparison wavelength, being the model that deviates less from the long baseline emission at 2.7 mm is considered a best match. Further discussion about NOEMA data-set can be found in section 3.5.3.

We discuss the effect of p surface density power law. The best models with different p values are presented in Figure 3.2. To complement the visibility models, the 2D density maps of each model with the same color scale are presented in Fig. 3.3. The figures show that a higher p value results in a denser disk inner region. The best fit parameters for each p value are indicated in the legend. The overall best fit model was found with p=1.5 (χ^2=2.01). In Table 3.4 we have two models with the same χ^2; in order to distinguish them, we used the model that best matches the NOEMA data-set. The best model has a dust disk mass of 0.0014 $M_{\odot}$, which is within the mass range of Segura-Cox et al. (2016) and Andersen et al. (2019). The best fit disk radius is 38 au. This radius is slightly higher than the range reported by Segura-Cox et al. (2016), which is (27.3–32.1 au) but still consistent with the size range of Class I disks in Perseus. The maximum grain size for the disk is 735 μm. The disk model is optically thick in the inner 25 au, therefore we only constrain the grain size in the outer regions of the disk. The fact that we found a collection of models with an upper limit for the maximum grain size in the disk lower than 2 mm and lower than the value assumed in Agurto-Gangas et al. (2019) is discussed in the following section. We summarized the best 10 disk models with p=1.5 in Table 3.4. Additionally we have highlighted the 5 models that best match the 2.72 mm data-set and in which the residuals are less than 4 mJy in average taking into account the long baseline flux within 30–80 kλ.

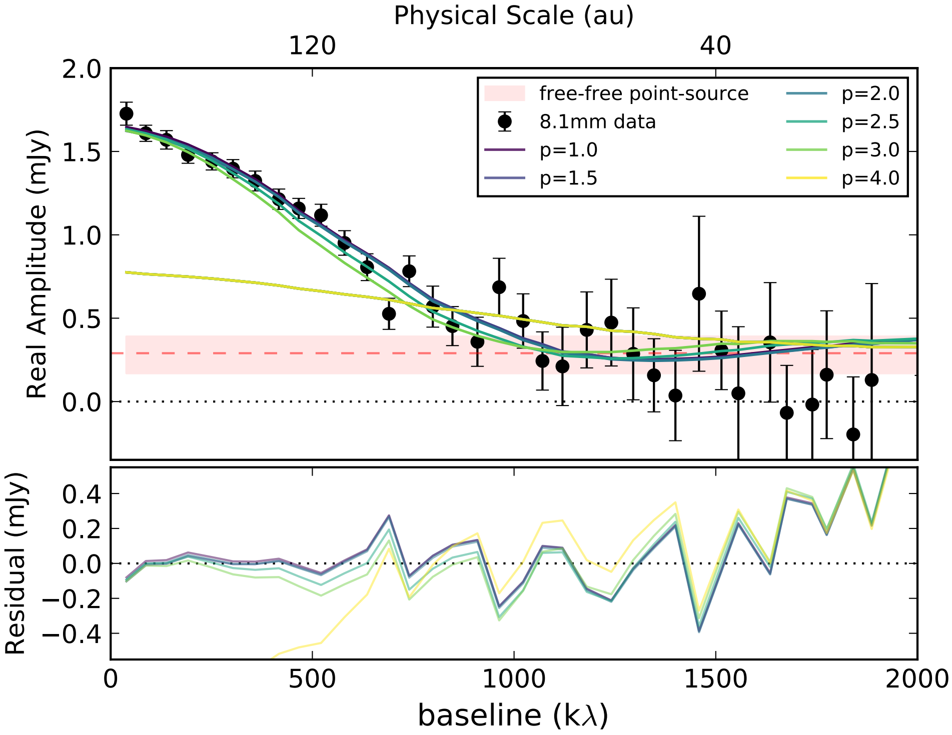

Figure 3.2: The real part of visibilities at 8.12 mm as a function of baseline. The black dotted line shows the zero flux. The colored lines are the best disk models for different p-values. The red dashed line indicates the freefree component of the emission. The bottom panel shows the residuals between the data and the models.

3.4.2 Envelope results

Using the best set of parameters for the disk model ($M_{\rm disk}$=0.147 M, $r_{\rm disk}$=38 au and $a_{\rm max}^{\rm disk}$=735 μm), the three free envelope parameters are explored. We present the best 10 visibility models at 1.29 mm and 2.72 mm in Figure 3.4 and the parameters in Table 3.5. The best model for the envelope was chosen by the lowest reduce χ2 given by the SMA

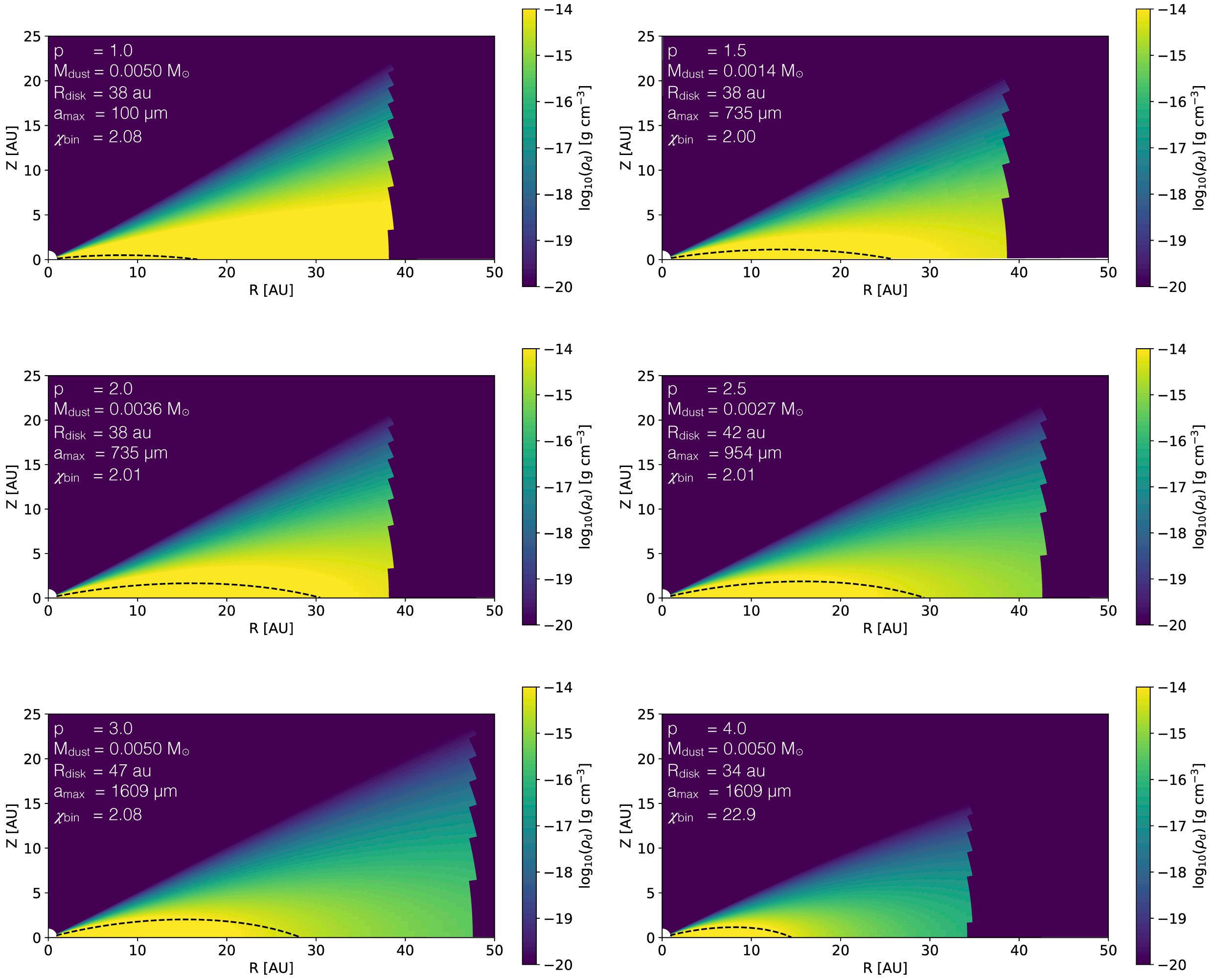

Figure 3.3: 2D disk density maps. Each panel shows the dust density structure of the best models with different p-values. The y-axis is the scale height of the disk in au, while the x-axes indicates the radius in au. Black dashed curves represents the $\tau = 1$ layer at 8.12 mm. The set of best disk parameters and $\chi^2_{\rm bin}$ are presented in the left corner of each panel.

data-set, which has a significant emission at short baselines associated to envelope scales, and using the NOEMA data-set as a flux reference. The bright emission at 2.72 mm, uncertainties and caveats are discussed in section 3.5.3. From the best radiative transfer model, we derive a total envelope mass of 0.074 $M_{\odot}$ within 8800 au. The discrepancies in mass lie in previous assumptions of dust temperatures that we discuss in section 3.5.2. Additionally, our best fit reveals a maximum grain size in the envelope of 26 μm which is

Table 3.4: Best disk parameters from the grid for p=1.5

$\chi^2_{\rm red}$	$M_{\rm disk}$ ($M_\odot$)	$r_{\rm disk}$ (au)	$a^{\rm disk}_{\rm max}$ (μm)
2.01	0.147	38	735
2.01	0.032	42	1609
2.05	0.043	42	2089
2.05	0.043	42	4570
2.06	0.032	42	1239
2.08	0.043	42	1239
2.08	0.032	42	2089
2.08	0.058	42	10000
2.08	0.043	42	3521
2.09	0.043	42	954

Parameter description: ($\chi^2_{\rm red}$) reduced χ^2, (M$_{\rm disk}$) total disk mass, ($r_{\rm disk}$) disk outer radius and ($a^{\rm disk}_{\rm max}$) disk maximum grain size. The highlighted values of $\chi^2_{\rm red}$ are the models with a residual at 2.72 mm less than 4 mJy considering the flux at long baselines.

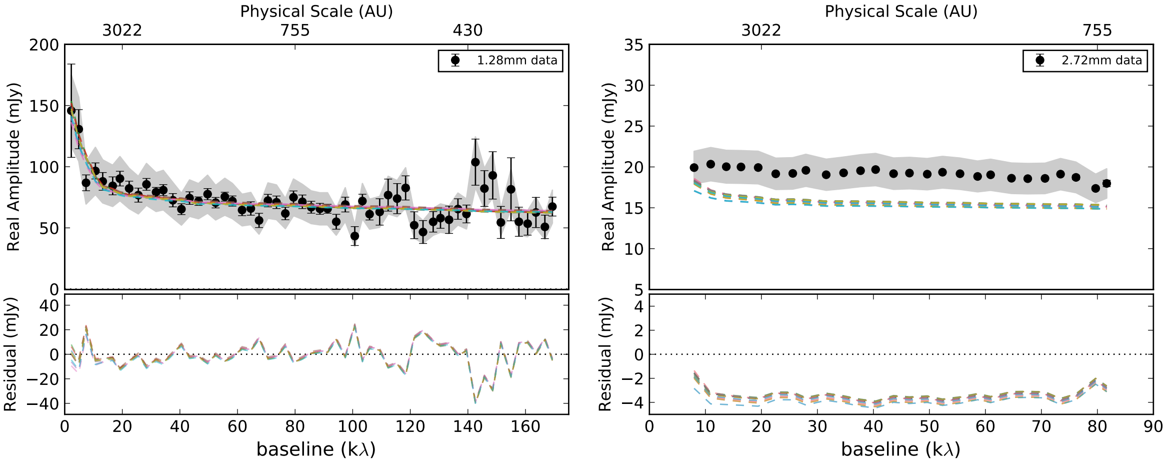

Figure 3.4: Best results of the envelope fitting, holding the disk parameters constant. Real part of the visibilities as a function of baseline. Left panel: 1.29 mm data. Right panel: 2.72 mm data. In dashed lines we present the best 10 models, which follow a range of envelope parameters of: envelope dust mass of 5.5–7.1$\times$ $10^{-4}\,M_\odot$, a rotational radius of 38–174 au and a maximum grain size of 5–102 μm. The gray region is the uncertainty of the data due to flux calibration. The bottom of each panel shows the residuals between the data and the models.

Table 3.5: Best envelope parameters from the grid

$\chi^2_{\rm red}$	$\rho_0^{\rm env}$ $\times 10^{-19}$ (g cm^{-3})	$M_{\rm env}$ $\times 10^{-4}$ (M$_\odot$)	$R_{\rm rot}$ (au)	$a_{\rm max}^{\rm env}$ (μm)	$F_{1.1\,\rm mm}$ (Jy)
1.998	2.51	7.35	113	26	0.278
1.999	3.41	7.17	90	37	0.272
2.000	1.85	7.53	140	19	0.288
2.004	4.64	7.01	73	73	0.305
2.007	1.26	5.54	140	7	0.257
2.008	4.64	7.01	73	52	0.276
2.012	1.85	5.41	113	10	0.249
2.013	3.41	7.17	90	52	0.277
2.015	8.58	4.81	38	102	0.360
2.018	0.99	5.68	174	5	0.261

Parameter description: ($\chi^2_{\rm red}$) reduced χ^2, ($\rho_0^{\rm env}$) envelope central density, ($M_{\rm env}$) envelope dust mass within 4400 au radius, ($R_{\rm rot}$) envelope rotational radius, ($a_{\rm max}^{\rm env}$) envelope maximum grain size and ($F_{1.1\,\rm mm}$) model calculated flux at 1.1 mm.

consistent with the range proposed in Agurto-Gangas et al. (2019), where we found a constraint on the envelope $a_{\rm max}$ of $<$100 μm. The absorption opacity per unit of dust from our model is $\kappa_{1.3\,\rm mm}$= 3.53 cm^2 g^{-1}, significantly larger than the value assumed in the previous studies ($\kappa_{1.3\,\rm mm}$= 0.899 cm^2 g^{-1}) (Sheehan & Eisner, 2018; Andersen et al., 2019). The best fit for the rotational radius $R_{\rm rot}$ of the Ulrich profile is 113 au.
To have an estimate of the flux missing at short baselines, we calculate the 1.1 mm flux and compare it to the single dish Bolocam measurement (Enoch et al., 2006). For the best model, we derive a flux that is $F^{\rm model}_{1.1\,\rm mm}$=278 mJy, 2.2 times fainter than the value reported by Enoch et al. (2006) ($F_{1.1\,\rm mm}$=612 mJy). The complete table of parameters of the best model and fixed parameters is presented in Appendix C.3.

3.5 Discussion

Here we discuss and compare the properties derived in this study with previous analyses of Per-emb-50. Additionally, we place the Per-emb-50 dust and physical properties in the context of Class I protostars.

3.5.1 Disk properties

Here we summarize the disk properties derived from the full radiative transfer of Per-emb-50 compared with previous studies and observations.

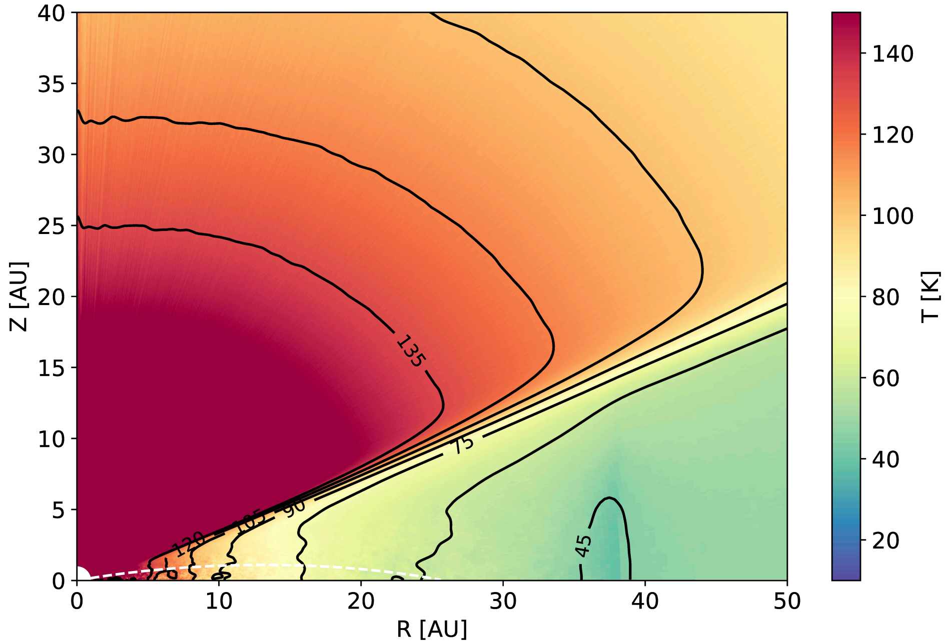

Figure 3.5: Temperature structure in cylindrical coordinates of the best disk model. The y-axis is the scale height of the disk in au and the x-axis is the radius in au. 2D temperature contours are presented as black lines. The white dashed curve represents the $\tau = 1$ layer at 8.12 mm.

Disk mass and radius

Per-emb-50 disk mass and radius are reported in Segura-Cox et al. (2016) and Andersen et al. (2019). We translate those values to the updated distance of Perseus, 293 pc, (Ortiz-León et al., 2017). The disk mass and radius range reported by Segura-Cox et al. (2016) are 0.27–0.56 $M_\odot$ and 27–32 au, respectively. The Andersen et al. (2019) total disk mass is 0.255 $M_\odot$. To estimate the disk mass in these studies, the Hildebrand (1983) equation is used. Segura-Cox et al. (2016) assume a dust temperature of 20 and 40 K, while Andersen et al. (2019) fixes it 30 K. The absorption opacity used in Segura-Cox et al. (2016) is $\kappa_{8.12\,\mathrm{mm}} = 0.146\,\mathrm{cm}^2\,\mathrm{g}^{-1}$, while Andersen et al. (2019) adopts $\kappa_{1.3\,\mathrm{mm}} = 0.899\,\mathrm{cm}^2\,\mathrm{g}^{-1}$, which is the dust opacity for coagulated dust grains with thin ice mantles at 1.3 mm calculated by Ossenkopf & Henning (1994).

In this work, the opacities and dust temperature are calculated consistently from the radiative transfer model. The opacity attributed to the $a_{\max}$ in the disk is $\kappa_{8.12\,\mathrm{mm}} = 1.289\,\mathrm{cm}^2\,\mathrm{g}^{-1}$. Fig. 3.5 shows the dust temperature through the disk best model. The 2D map shows vertical temperature distribution of the disk versus radius. While the inner temperatures of the disk are order 80 K, the outer regions are cooler, with an average value of 45 K.

Additionally, Fig.3.6 compares the previous disk models. The disk radius obtained in this work is slightly larger than the results coming from the Two-step model ($r_{\mathrm{disk}} \sim 33$ au), the full radiative transfer model ($r_{\mathrm{disk}} \sim 27$ au) (Agurto-Gangas et al. (2019), see Table C.4) and the Segura-Cox et al. (2018) analytic model, 27–32 au. The derived total disk mass is 50% lower than previous studies. This discrepancy may be caused by the opacity variation among the different studies or due the fact that Per-emb-50 disk is optically thick in the innermost regions. Another interesting comparison for the dust mass is to compare with the mass of solids in exoplanetary systems. Recently, Tychoniec et al. (2020) estimated dust disk masses for several Class 0 and Class I in Perseus, revealing that the medians of the distributions is 158 and 52 $M_\oplus$, respectively. For Per-emb-50 they estimate a dust mass of 535±91 $M_\oplus$, which is comparable with our value of 468 $M_\oplus$. However, their mass estimation assumes a 30 K dust temperature and an opacity that considers large grains up to 1 cm, while we have properly modelled the temperature profile with a radiative transfer model exploring different dust sizes.

In this analysis we also have varied the power law in the disk density. This is a parameter that can be varied from the typical value assumed in Class II disk (p=1), and can be constrained using multi-wavelengths observations. We also noticed that even at 8.12 mm the inner regions of the disk could be still optically thick. This, could be an indication that larger dust particles are accumulating at the deeper layers of the disk mid-plane, which is a natural outcome from dust settling.

Disk maximum grain size

In Agurto-Gangas et al. (2019), $a_{\max}$ in the disk was fixed to 1 cm, which is more than 10 times higher than the best fit obtained value in this work. The main difference with the Agurto-Gangas et al. (2019) model is the optical thickness of the disk. While in this study an optically thick layer zone is situated in the inner <25 au, the disk model with maximum grain size of 1 cm is completely thick (Agurto-Gangas et al., 2019). In Figure 3.6 we see that the optically thick model is overestimating the emission at baselines <1000 kλ. Still, mm or cm sized grains may be present in the disk mid-plane and inner regions of Per-emb-50, but with the current data-set we are not able to constrain the disk $a_{\max}$ within radius of 25 au.

From the best 10 disk models we can put a lower limit for $a_{\max}$ close to 735 μm while the upper limit could still be in agreement with grains of the order of mm-cm-sizes, specially in the deep layers of the disk.

It is interesting to compare the best model of $a_{\max} = 735\mu$m with others studies of grain growth in Class I protostars. In the analysis of Sheehan & Eisner (2017) using 1.3 mm visibilities and broadband SED data, the average maximum grain size of the Class I disks in Taurus is ~ 5 mm. Another study in a Class I disk in ρ Ophiuchus by Sheehan & Eisner (2018) uses ALMA at 870 μm and 3 mm and SED, revealing a maximum grain size of 8 ± 0.6 cm. Both studies support the idea that significant grain growth is already taking place in this young disks. However, to constraint $a_{\max}$ several precautions must be taken. Specially important is to explore the parameter space taking into account limits that makes sense physically and inform the model with previous studies in order to reduce the amount of free parameters.

Furthermore, multi-wavelength dust polarimetric observations have derived $a_{\max}$ values of

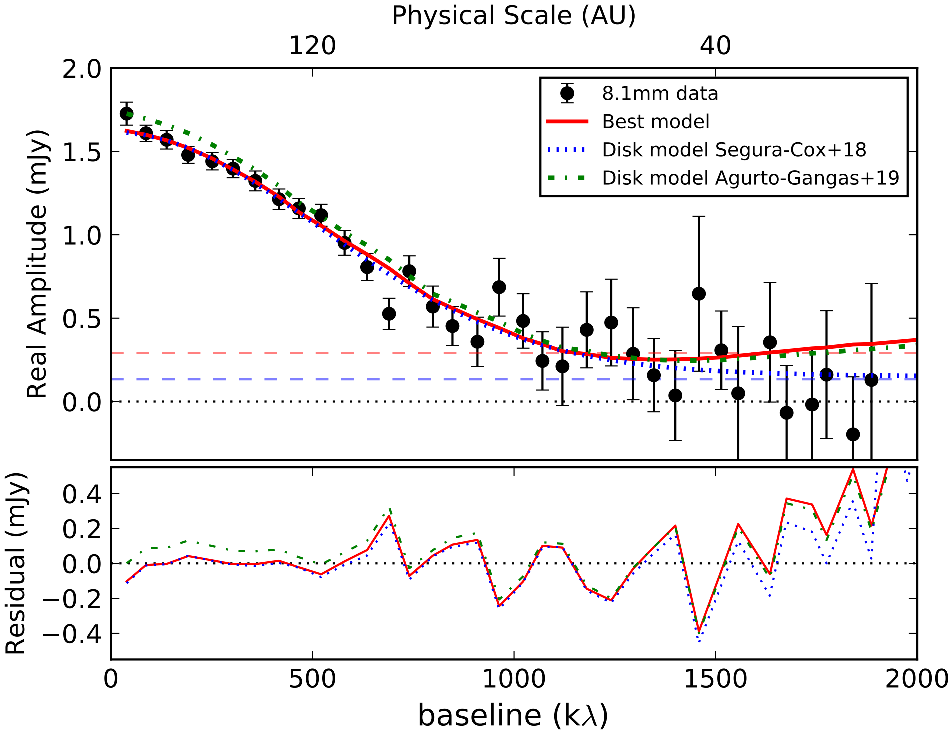

Figure 3.6: Visibility data and models at 8.12 mm vs baselines. The red curve shows the disk best model from this study with red dashed line showing the freefree point-source component. The blue dotted line indicates the analytic disk model and blue dashed line shows the freefree point-source component of 0.13 mJy both presented in Segura-Cox et al. (2018). The green dash-dotted line shows the disk model assumed in Agurto-Gangas et al. (2019). The bottom panel shows the residuals between the data and the models.

50–150 μm (Kataoka et al., 2015, 2016; Hull et al., 2018). Multi-wavelength analysis and modeling of Class I protostars are needed to constrain and reveal the dust grain size in the disk interiors.

3.5.2 Envelope properties

In this section the best fit envelope parameters are discussed and compared to the results in Agurto-Gangas et al. (2019) and Andersen et al. (2019).

Envelope mass

The envelope mass of Per-emb-50 is calculated in Stephens et al. (2018) and Andersen et al. (2019). We scaled those values of the mass to reflect the updated distance to Perseus (293 pc; Ortiz-León et al. (2017)). The Stephens et al. (2018) mass is 0.135 $M_\odot$ while Andersen et al. (2019) is 0.162 $M_\odot$. Both masses are calculated using Hildebrand (1983) equation,

$$M = \frac{d^2 F_\nu}{B_\nu(T)\,\kappa_\nu}, \tag{3.8}$$

and adopting $\kappa_{1.3\,\mathrm{mm}}$= 0.899 cm^2 g^{-1}, which is the dust opacity for coagulated dust grains with thin ice mantles in column 5 of Table 1 in Ossenkopf & Henning (1994). In Stephens et al. (2018) is assumed a T_{dust}=10 K, while Andersen et al. (2019) used the Dunham et al. (2014) dust temperature of 15 K for Class I sources. In Agurto-Gangas et al. (2019) the envelope model mass was derived using a spherically symmetric profile (Tafalla et al., 2002), which returns a total mass of 1.54 $M_\odot$. Considering the difference in terms of density structure within the Tafalla and Ulrich profile, it is not surprising to see a lower total mass of 0.07 $M_\odot$ in this new modeling. Compared with the envelope masses derived by Andersen et al. (2019), our result is in agreement with the mass trend seen in all Perseus protostars covered with MASSES. If we compare with the single dish data at 1.1 mm we have to take into account that Enoch et al. (2006) uses intensity, in units of Jy beam^{-1}, to calculate the envelope mass. A larger beam adds more flux per beam since the protostar is embedded in an extended cloud. The difference in the beam sizes, 31vs. 2, lead to overestimates in envelope flux, which affects the derived envelope mass. Our models support this, showing that the total flux at 1.1 mm is almost 50% lower than the single dish observations with Bolocam 1.1 mm.

Envelope rotational radius

The best model has an envelope rotational radius of 113 au. The spread within the best 10 models is small, from 38 au until ∼170 au. Still, the study of the transition zone from the in-falling rotating envelope to the disk scales is complex. Sakai et al. (2014b,a) revealed that line tracers as CCH, c-C_3H_2, and CS are needed to identify centrifugal radius and the centrifugal barrier of the infalling-rotating envelope. Thus, a detailed study of the

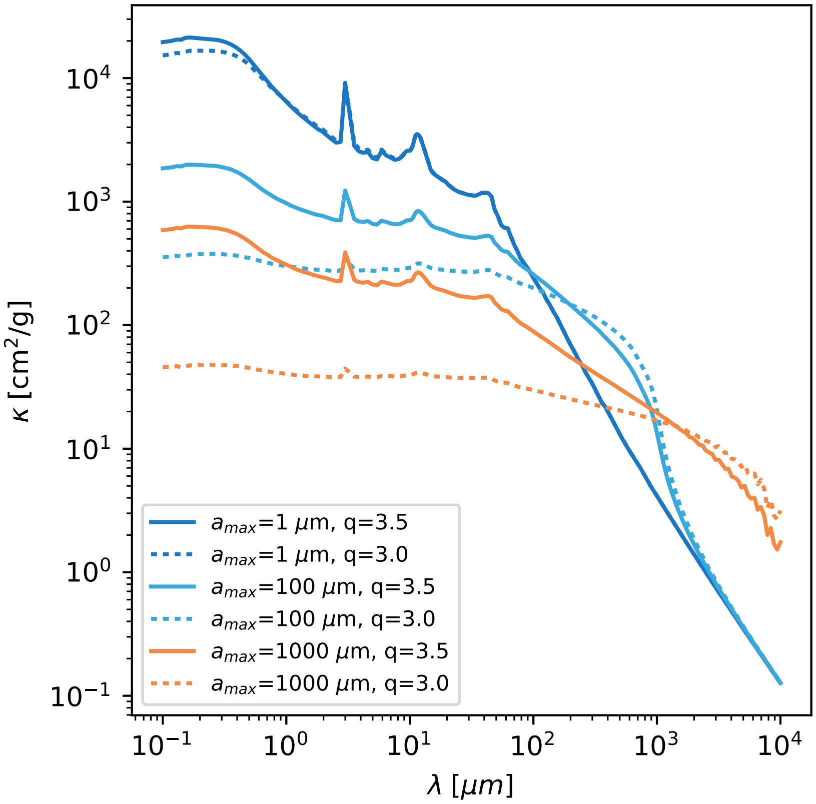

Figure 3.7: Dust absorption opacity as a function of wavelength for grain size distributions characterized by $n(a) \propto a^{-3.0,-3.5}$. $a_{\rm min}$ is fixed at $0.1\,\mu$m and the maximum grain size increases from $1\,\mu$m to $1000\,\mu$m.

transition zone in the vicinity of the protostar using different chemical tracers is mandatory to constraint the rotational radius and to understand disk formation as well.

Envelope grain size distribution

The main result from the radiative transfer modeling in Agurto-Gangas et al. (2019) is that there is no millimetre sized grains in the inner envelope of Per-emb-50 and that the maximum grain size is $\leqslant 100\,\mu$m. In this work, we decide to use the same dust power law distribution for the disk and envelope, fixed to $q = 3.5$, which does not pre-impose grain growth in the disk like a $q = 3.0$ assumption does, since 3.5 is the ISM value. This allows us to create a completely new grid of models to compare with previous studies, that fixed q to 3.0 for the envelope dust (Miotello et al., 2014; Agurto-Gangas et al., 2019). In the specific case of Per-emb-50, the q parameter is not affecting the result of $a_{\rm max}$ in the envelope in Agurto-Gangas et al. (2019). In figure 3.7 we illustrate this conclusion. The effect of q is important at shorter wavelengths, while the difference in opacity is small at millimeter wavelengths.

Additionally, we explored the effect of changing $a_{\rm min}$ from $0.1\,\mu$m to larger sizes until we reach a distribution with dust sizes similar to $a_{\rm max}$. In Fig. C.8 we show the change of $a_{\rm min}$ from $0.1\,\mu$m to $20\,\mu$m, keeping a value of $a_{\rm max}$ of $26\,\mu$m, which is the value of the best model. With increasing $a_{\rm min}$ the model deviates more and more from the observed data. At 2.72 mm this effect is more prevalent and it may indicates that the envelope of Per-emb-50 is dominated by few μm size grains. We have to remark that even changing the dust distribution power law in the envelope, $a_{\rm max}$ is consistently smaller than $< 100\,\mu$m within our best 10 models.

3.5.3 2.72 mm data

We have explored different alternatives to explain the bright emission at 2.72 mm compared to the radiative transfer models.

Per-emb-50 was observed during 2 nights separated by 6 days. We have cross-checked the flux calibrators with the ALMA calibrator catalog in order to compare the values and the consistency of the observing runs. The first run uses the 3C454.3 as bandpass calibrator and flux calibrator. The difference between the computed flux and model flux for the flux calibrator is 24%. On the other hand, comparing the flux used for 3C454.3 calculated for the second run, the variation in flux is 20%. A similar behaviour is seen when comparing to the values from the ALMA calibrator catalog. We have checked the possibility that having a 20% variation in the flux calibration between both sessions could affect the averaged visibilities. A new calibration using the flux calibrator of the first run was performed in both data-sets. This revealed that the visibilities of Per-emb-50 were not affected in either this new calibration method or the previous calibration in Agurto-Gangas et al. (2019).

In section 3.2.1 the contribution of the thermal free-free emission typically produced by jets or stellar winds, is calculated. The contribution at 2.72 mm is close to 2%, adding a constant flux emission of 0.47 mJy at all baselines. The free-free contribution of Per-emb-50 at 2.72 mm may be compared with the free-free contamination estimated for Class 0 protostars in Galametz et al. (2019). Their observations at 3.2 mm with NOEMA show that the free-free contribution, for a sample of Perseus Class 0 protostars, have values of 1.4-19 %, consistent with the value derived for Per-emb-50.

Another possibility discussed in Galametz et al. (2019), is that the enhanced emission at $\sim$3 mm may be attributed to the presence of amorphous dust grains. Models of emission from amorphous dust grains do predict enhanced long wavelength brightness mainly due to two-level system fluctuations in the dust grains (Meny et al., 2007; Paradis et al., 2011; Mason et al., 2020). Future explorations of the dust properties and different chemical composition than used in this analysis may help to understand the nature of this enhanced emission at 2.72 mm.

3.6 Conclusions

We have analyzed the 1.29, 2.72 and 8.12 mm continuum emission of the Class I protostar Per-emb-50 which has been observed with SMA, NOEMA and VLA at 400, 600 and 20 au resolution, respectively. Using radiative transfer modelling, we have fitted the envelope and disk emission with an Ulrich profile and a self-consistent disk model based on the two layer approximation. We derive the mass of the disk and envelope, that we then compared with values derived with the simple flux-to-mass conversion obtained by Segura-Cox et al. (2016); Stephens et al. (2018); Andersen et al. (2019). The discrepancies are due to the better determination of the temperature profile enabled by our radiative transfer analysis. The parameters derived with our best fit provide structural and dust grain property on the envelope and at disk scales. We reached the following conclusions:

- Our detailed radiative transfer modelling of the disk allow us to determine new estimates of the disk dust mass and radius of Per-emb-50, finding values of 0.0014 $M_{\odot}$ (468 $M_{\oplus}$) and 38 au, respectively. The dust content suggests that Per-emb-50 disk may form giant planets in the future, according to the Minimum Mass Solar Nebula (0.01–0.1 $M_{\odot}$) of Weidenschilling (1977).

- We put constraints on the level of grain growth in the region between 25 and 38 au of the disk, finding a lower limit of $a_{\rm max} \geqslant 735\,\mu$m, with a power law grain size distribution of q=3.5. The level of grain growth in the innermost disk zone (<25 au) remains unconstrained given that it is optically thick, requiring multi-wavelength observations to determine this.

- Additionally, we provide a better fit and constraints for the envelope contribution using a collapsing envelope Ulrich profile. This structure is suitable for the physical scales that the observations are probing. We find an envelope rotational radius of $\sim$ 113 au, and a maximum grain size of 26 μm, which is in agreement with the upper limit found in previous envelope models of (Agurto-Gangas et al., 2019).

- We confirm the results of Agurto-Gangas et al. (2019), finding that the Per-emb-50 envelope has no mm-size grains, while Miotello et al. (2014) finds grains with mm sizes in two envelopes of other Class I protostars in Ophiuchus. This could suggest that the environment may play a key role in the dust evolution in the earliest phases of star formation. Clearly, the study of a larger sample of Class I sources in different star-forming regions is urgently needed to understand how general and universal the grain growth process is in these stages.

Future ALMA observations, using a combination of compact and extended configurations to better spatially constrain the transition zone between disk and envelope, at different wavelengths, will allow us to remove the degeneracies in the modeling. This will provide new cases to understand and clarify the apparent dust grain size disagreement determined in the latest observations.

Chapter 4

Simple Disk Envelope (`SiDE`) fit framework

The code presented in this chapter is published and available in Zenodo:

Agurto-Gangas & Szucs (2020)

4.1 Framework overview

The `SiDE` (Simple Disk-Envelope) fit combines a flexible model setup, the radiative transfer, the (u, v) space transformation and the `emcee` MCMC sampler tool to optimise the model parameters in an open source framework. `SiDE` is based on Python packages (emcee,corner and uvplot), `radmc3dPy` and GALARIO for modeling radio and millimeter observations of the dust in young protoplanetary disks using interferometers like the NOrthern Extended Millimeter Array (NOEMA) and the Atacama Large Millimeter/Submillimeter Array (ALMA). The main utility of `SiDE` is to provide a direct interface between RADMC-3D and Python for creating radiative transfer models of protoplanetary disk and/or protostellar envelopes and to directly obtain images and visibilities from the models. With this Python integration of libraries we can fit models to the observations using a Bayesian Markov chain sampler to an adequate exploration of the parameter space. In the following sections we describe the motivation behind this tool, the basic functionality, the details on the modelling setup and the fitting procedure. The summary of the documentation and installation instructions are available in our git repository[1].

4.2 Motivation

In the last years, ALMA and VLA have provided a large amount of (sub-)mm observational data-sets with increasing angular resolution and sensitivity, making the multi-wavelength

---

[1] `https://github.com/cagurto/SiDE`

analysis an ideal tool to reveal the disk and envelope structure and the dust properties as well. In Chapter 3 we ran a grid of radiative transfer models for Per-emb-50 that were then compared with the millimeter data-sets in order to determine physical system parameters. However, this strategy to find the best model is limited to a small amount of discrete values for each parameter, and it can get computationally expensive and slow when the number of parameters is too large.

Here, we present a fitting framework that combines the radiative transfer procedure used in the previous Chapter with the addition that the model parameters are optimized using the Markov Chain Monte Carlo `emcee`[2] sampler tool (Foreman-Mackey et al., 2013b).

`SiDE` provides a Python interface for setting up a single or a set of radiative transfer models including: the computation of the wavelength dependent dust opacities for a user selectable grain size distribution and composition, computing their temperature distribution and synthetic images directly in Python and obtaining complex visibilities and χ^2 values if observational constraints are given.

The advantages of using this fitting tool is, firstly to setup a 3-D (axisymmetric) radiative transfer model with a physically motivated disk+envelope structure and a consistent dust temperature calculation instead of a 2D analytical model (Segura-Cox et al., 2016). Second, even though these models are computationally intensive to run, it is possible to speed up the run time when is run in parallel with a large number of CPU cores. Third, the flexible setup allows us to explore parameters that are usually fixed, as for example, envelope density profiles and minimum and maximum disk and/or envelope grain size distributions. We describe the physical components and free parameters of the model as well as details about the posterior probability distribution of the fitted parameters in the following sections.

4.3 Installation

Here we summarised the steps to build and install `SiDE` using Linux and/or Mac OS X operating systems.

4.3.1 Requirements

`SiDE` requires the previous installation of the following software's and libraries:

- Python (2.7 or 3.5+)
- matplotlib
- numpy
- radmc3dPy
- galario
- uvplot
- emcee
- corner
- mpi4py
- RADMC3D

---

[2] https://emcee.readthedocs.io

The latest release of RADMC-3D (version 0.41) needs to be patched before running this code. It is necessary to replace `main.f90` with `radmc3d_patch/main_patch.f90` in the `$RADMC3D_PATH/version_0.41/src` folder and recompile code. The patch is already merged to the development branch of RADMC-3D, but have not been released yet.

4.3.2 General instructions

The first step of this procedure is to either download the repository from the browser or clone the repository and create a directory where to install `SiDE`. Once you have installed the requirements, `SiDE` can be installed with the Python module:

```
$ python setup.py install --user
```

On Linux this installs the module to `~/.local/lib/python2.7/3.6/site−packages` directory, which is usually included in the python search path. Alternatively, it is possible to directly add the repository location to your `PYTHONPATH`:

```
$ export PYTHONPATH=$PYTHONPATH:/path/to/your/SiDE/directory
```

After completing the installation step, the module should be available in Python:

```
import side
```

4.3.3 Installation in Anaconda environment

If you are using the Anaconda distribution, you can create and activate for example, Python 3.7 environment, with,

```
conda create -n [new_environment] python=3.7
conda activate [new_environment]
```

where `new_environment` should be replaced with your preference name. Then, add conda-forge to the software channels:

```
conda config --add channels conda-forge
conda config --set channel_priority strict
```

and install requirements with:

```
conda install galario
conda install astropy
conda install ipython
conda install mpi4py
```

These instructions should be sufficient to download and install the program package:

```
git clone https://github.com/cagurto/SiDE.git
cd SiDE
python setup.py install --user
cd ..
```

Run a test to check if some more dependencies are needed,

```
ipython
```

```
import radmc3dPy
import side
```

Finally, install RADMC-3D

```
wget http://www.ita.uni-heidelberg.de/~dullemond/software/radmc-3d/*.zip
cd radmc-3d/version_0.41/src/
cp ../../../SiDE/radmc3d_patch/main_patch.f90 main.f90
make
make install
```

4.4 Code components

The `SiDE` fitting tool is written in Python language and links the Markov Chain Monte Carlo fitting with radiative transfer codes to model the structure of young protostars. The code components are the following:

- **radmc3dModel() class**
  Interface for creating, running and analysing RADMC-3D models. The class provides storage, read-in and write-out routines, runner interface to call RADMC-3D as a child process and interface to galario code to translate images to the complex visibility space. Plotting routines should be added in the future.

- **radmc3dRunner() class**
  The radmc3dRunner class provides a subprocess to compute dust temperature and dust continuum emission maps in the current folder.

- **emcee_chain() class**
  Class containing MCMC chain data and associated methods.

Additionally, `SiDE` uses the following files:

models.py

This Python library contains the density profile description of the flaring disk, a variety of envelope profiles and an slab profile. Additionally, dust mass and spectral energy distribution of the Interstellar Radiation Field calculations are described. A brief summary of each Python def is presented here:

- **def ulrich_envelope()**
  Returns dust density distribution of a rotationally flattened protostellar envelope. The profile is given by Ulrich (1976).
- **def tafalla_envelope()**
  Returns protostellar envelope dust density distribution according Tafalla et al. (2002).
- **def powerlaw_envelope()**
  Returns power law protostellar envelope dust density distribution.
- **def envelope_cavity()**
  Returns density distribution with reduced values in a cone or cylinder.
- **def slab()**
  Returns the dust density distribution of a slab between r0 and r1 radius and z0 and z1 in height. The slab is rectangular in Cartesian coordinates. `SiDE`, however, uses spherical coordinate system, where the cells have curved shapes. Adding a slab with Hz $<$ r will result in blocky density distribution.
- **def flaring_disk()**
  Returns flaring disk dust density distribution.
- **def computeEnvMass()**
  Compute envelope total dust mass and dust mass within 3000 au.
- **def ISradField()**
  Computes the spectral energy distribution of the Interstellar Radiation Field, based on Draine (1978) and Black (1994) prescription.

sampler.py

This Python library computes posteriori probabilities of parametrised Class 0/I models. A brief summary of the Python def is presented here:

- **def run_mcmc()**
  The observational constraints (visibility data) must be provided in the uvdata argument. The radiative transfer model parameters must be provided in the paramfile. The fitted parameters (specified in parname argument) will be changed during the MCMC procedure. The initial values of the fitted parameters are provided in the p0 argument. All other model parameters are as set in the paramfile. More details in Section 4.6.

bayes.py

This Python library contains the following functions:

- **def lnpriorfn()**
  Uniform prior probability function.
- **def lnpostfn()**
  Log of posterior probability function.

More details in Section 4.6.

4.5 Packages used by `SiDE`

`SiDE` uses the following packages:

- `radmc3dPy`[3] is a Python package to the 3D radiative transfer code RADMC-3D. Computes the dust density distribution given the model parameters and saves necessary input files for RADMC-3D to a temporary folder. It also proves the image class that is used to store the synthetic images.
- RADMC-3D computes the temperature for a given dust density distribution and heating stellar radiation with a Monte Carlo photon package based method (see Dullemond et al., 2012). The output file of this computation that assumes the dust is in radiative equilibrium with its radiation field is `dust_temperature.dat`, which contains the dust temperature everywhere in the model. Once the dust temperature is known, the ray-tracer utility computes synthetic emission maps at the requested wavelengths. Multiple wavelengths may be ray-traced at once in order to speed up computation, given that their resolution, field of view and orientation matches. For the test of this framework we assume that scattering has negligible effect on the dust temperature and the final image. RADMC-3D is called in child mode[4] once per model using the `subprocessing` Python module (and operating system provided pipes). `SiDE` is responsible for passing parameters and retrieving results (dust temperature, images) from RADMC-3D.
- GALARIO (Tazzari et al., 2017) computes synthetic visibilities given a model image (or an axisymmetric brightness profile) and their comparison to the observations. In this work we use its double precision CPU based sub-module. The default value for the number of threads in the parallel version is set to one, but can be set to the available number of processor cores. The visibilities of the image model are calculated through `galario.double.sampleImage`. It also computes the χ^2 values

---

[3] `https://www.ast.cam.ac.uk/~juhasz/radmc3dPyDoc`

[4] "child mode" means that all the outputs of RADMC-3D that usually would go to screen now are redirected to a separate file called `radmc3d.out`.

with `galario.double.chi2Image`, that are used to estimate the likelihood of the model. The effective χ^2 of a model is obtained by:

$$\chi^2 = \sum_{j=1}^{N} w_j * [(ReV_{obs\ j} - ReV_{mod\ j})^2 + (ImV_{obs\ j} - ImV_{mod\ j})^2] \tag{4.1}$$

where V_{mod} are the synthetic visibilities, which are computed with `sampleImage`.

- `emcee` (Foreman-Mackey et al., 2013a) is a Python implementation of Goodman & Weare's Affine Invariant Markov chain Monte Carlo (MCMC) Ensemble sampler that determines the new model parameters based on the likelihood of the previous generation of models. It provides MPI parallel capabilities which is used to distribute the computation of individual walkers to CPU cores and computer nodes. The Python classes of `EnsembleSampler` and `MPIPool` are used in `SiDE`. `EnsembleSampler` allows us to run simultaneously several walkers interacting with each other to converge to the maximum of the posterior and `MPIPool` facilitates the use of MPI pools instead of Python threads which is useful for running on computer clusters using multiple nodes.

Furthermore, `SiDE` provides utilities to combine content of two or more emcee chain class objects, to plot the path taken by walkers for each fitted parameters, to visualize the posterior probability of models explored by walkers and to plot the posteriori distribution of the fitted parameters with `corner` (Foreman-Mackey, 2016). More details in the following sections.

4.6 Example of basic usage

After installation, the load of a setup model including disk, envelope profiles can be done as following:

```python
import side
import numpy as np
# Read .inp parameter file
par = side.getParams(paramfile='source_params.inp')
```

Each parameter can be changed interactively in Python or in the main `source_params.inp` file. An example of the file can be found in Appendix D.1. In Figure 4.1 the data-flow for `SiDE` is presented. For the fitting procedure it is necessary to have the following files and information in a Python script:

- **Observational data** The data-sets have to be provided with the format: u [m], v [m], Re [Jy], Im [Jy], w [$1/\sigma^2$], where u and v are the plane locations of the observed visibilities, Re and Im are the real and imaginary part of the observed visibilities and w is the visibility weight. The data can be loaded following:

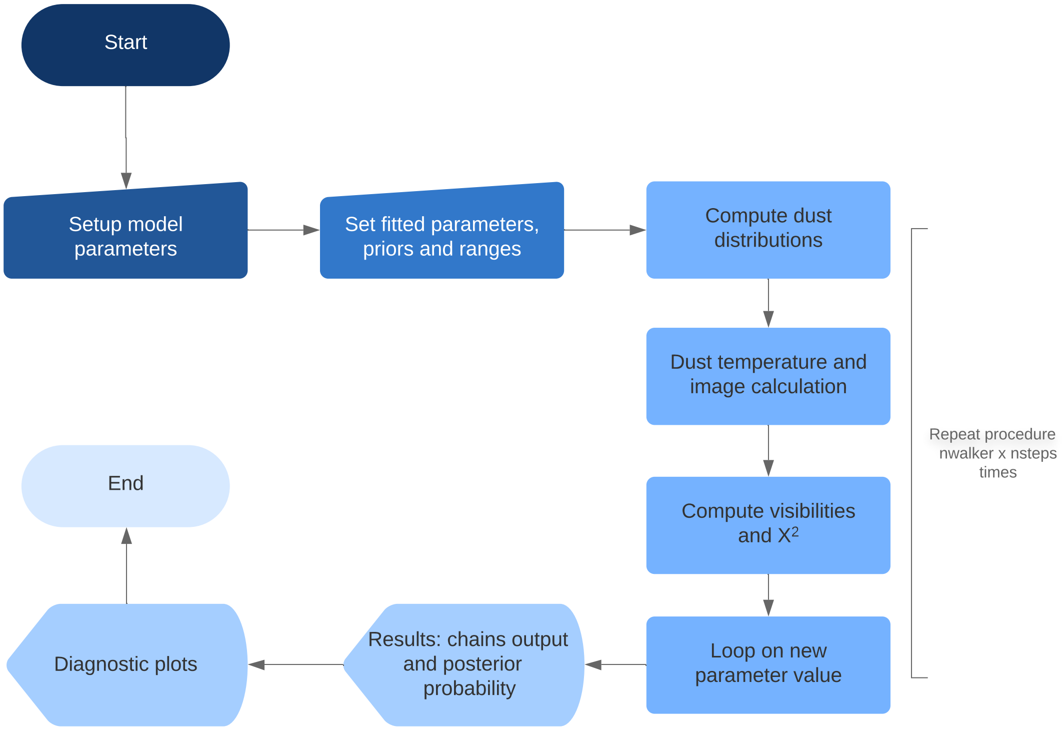

Figure 4.1: Flow chart of the algorithm proceeding from start to end. Right blue sequence is repeated during the Markov Chain Monte Carlo.

```
# Alternative 1 to read visibility file
u1, v1, Re1, Im1, w1 = np.require(np.loadtxt('visibility-file1.txt', unpack=True)
u2, v2, Re2, Im2, w2 = np.require(np.loadtxt('visibility-file2.txt', unpack=True)
# Alternative 2 open pickle files
import pickle
u1, v1, Re1, Im1, w1 = pickle.load(open('visibility-file1.p','rb'))
u2, v2, Re2, Im2, w2 = pickle.load(open('visibility-file2.p','rb'))
```

In this example we are loading two data-sets at different wavelengths. An example of observed visibility files can be found in `https://github.com/cagurto/SiDE/tree/master/examples`. To bundle the visibility data and to set the image parameters, `visdata` and `impar` have to be defined,

```
# Bundle visibility data
visdata = [{'u':u1, 'v':v1, 'Re':Re1, 'Im':Im1, 'w':w1, 'wav':1100.},
           {'u':u2, 'v':v2, 'Re':Re2, 'Im':Im2, 'w':w2, 'wav':3000.}]
```

```
# Set image parameters
impar = [{'npix':512,'wav':[1100.,3000.],'sizeau':11000,'incl':67.}]
```

- **Model image options** In `visdata` and `impar` have to be define `wav` which is the wavelength in microns, `npix` is the number of pixels on the rectangular images, `sizeau` is the diameter of the image in au and `incl` is the inclination angle of the source. In this framework the input original image size can be re-scaled to speed-up the model image time computing. This was implemented in the previous analysis of Chapter 3, where we required a large image size to model the observation, but only a small percent from extended emission contributed to the modelled *uv*-range. To avoid do the raytracing on pixels that doesn't contribute much to the overall visibility `sizeau_ext` is used. The new image conserves the original image resolution (in terms of au/px), the old image size is specified in `sizeau_ext` and `sizeau` covers the new image size. The original image is stored in the center of the new image, while the extended image size is filled out with zero values. It is recommended to check the data-sets with GALARIO, using `get_image_size`, before to implementing this change. In case of a typical model using for example the data-sets of Chapter 3, the computation time is dominated by the raytracing step. To fully resolve the models on the same scale as the observations, large synthetic images are needed. Typical runtime of the thermal radiation transport is 30 – 40 s, for GALARIO runtime is 6 – 10 s.

- **Model options** In the `paramfile` is possible to setup the stellar properties, dust opacity and density profiles for different components. The disk model is given by a flaring density profile in which is possible to change parameters as the height of the disk, flaring index, density power law, inner disk radius among others. The envelope profile has four options: `powerlaw, Tafalla2004, Ulrich1976` and `Ulrich1976_2`. In Table 4.1 are the parameters that have to be setup for each envelope density profile. In the case of `powerlaw` and `Tafalla2004` density models the parameter `r0Env` refers to the radius at which `rho0Env` is defined, while in the case of the `Ulrich1976` density profile `r0Env` is the centrifugal radius.
  The block of dust opacity contains the option to change the number of grain populations, `ngpop`. This version of the framework accepts up to three different dust populations, one for the disk and two for the envelope. If `Ulrich1976_2` is setup, `Envcut` has to be defined in the `paramfile`. `Envcut` is a limit in units of au where one dust population is in the inner part of `Envcut` and another dust population outside `Envcut`.
  Additionally, if the model contains an outflow cavity then it is possible to setup different cavity shapes with `modeCav`. The available cavity shapes are: `Sheehan2017, edgecenter` and `gridcenter`, see Fig. 4.2. `Sheehan2017` is a outflow cavity model from Sheehan & Eisner (2017) characterized by:

$$z > 1\,\mathrm{au} + r^{\zeta}, \tag{4.2}$$

Table 4.1: Model setup parameters

	Parameter				
Envelope model	`rho0Env`	`r0Env`[a]	`rTrunEnv`	`prhoEnv`	`ngpop`
`powerlaw`	✓	✓	✓	✓	1
`Tafalla2004`	✓	✓	✓	✓	1
`Ulrich1976`	✓	✓	✓	✗	1
`Ulrich1976_2`[b]	✓	✓	✓	✗	2

([a]) `r0Env` is the centrifugal radius in the Ulrich profile. ([b]) To setup 2 different dust populations in the Ulrich profile `Envcut` has to be define in units of au.

where 1 au is the height above the midplane where the cavity starts and ζ characterizes the shape and opening angle of the cavity. More details in Eisner (2012). In the `gridcenter` option the cavity start at the center of the model grid (0,0,0), while in the `edgecenter` the cavity start at the outer radius of the disk following the equation:

$$\arctan\left(\frac{r\sin\theta - r_{disk}}{r\cos\theta}\right) < \theta_{cav}, \tag{4.3}$$

where $r_{\rm disk}$ is the outer radius of the disk in au, and $\theta_{\rm cav}$ is the open angle onf the cavity in degrees.

- **Fitting arguments** The next step is to define a dictionary that contains keyword arguments for the logarithm of the posterior probability function `lnpostfn()`. An example of `kwargs` is given by:

```
kwargs = {'dpc': 125., 'incl': 67., 'impar': impar, 'verbose': True,
            'idisk':True, 'ienv':True, 'icav':False,
            'cleanModel': True, 'binary': True, 'chi2_only':True,
            'galario_check':False, 'time':True }
```

where `dpc` is the distace to the source in unit of parsec, `impar` collects the image parameters, `verbose` is an option to print a summary of the model parameters and the inclusion of the model profiles with `idisk` (disk profile), `ienv` (envelope profile), `icav` (outflow cavity) and `islab` (slab model). `cleanModel` is an option to delete the RADMC-3D model folder from disk after the posterior probability estimation, therefore the model files are not stored. If `binary` is True then RADMC3D will use binary format otherwise the file format is ascii. The use of binary files improves the computation speed and reduces disk space usage when models are kept.

The keyword `chi2_only` computes and store the χ^2 between the data and model. If it is True the synthetic visibility is computed but not stored (a zero value array is stored instead). The χ^2 is still computed and stored. Set this to True when running MCMC fitting in order to improve speed.

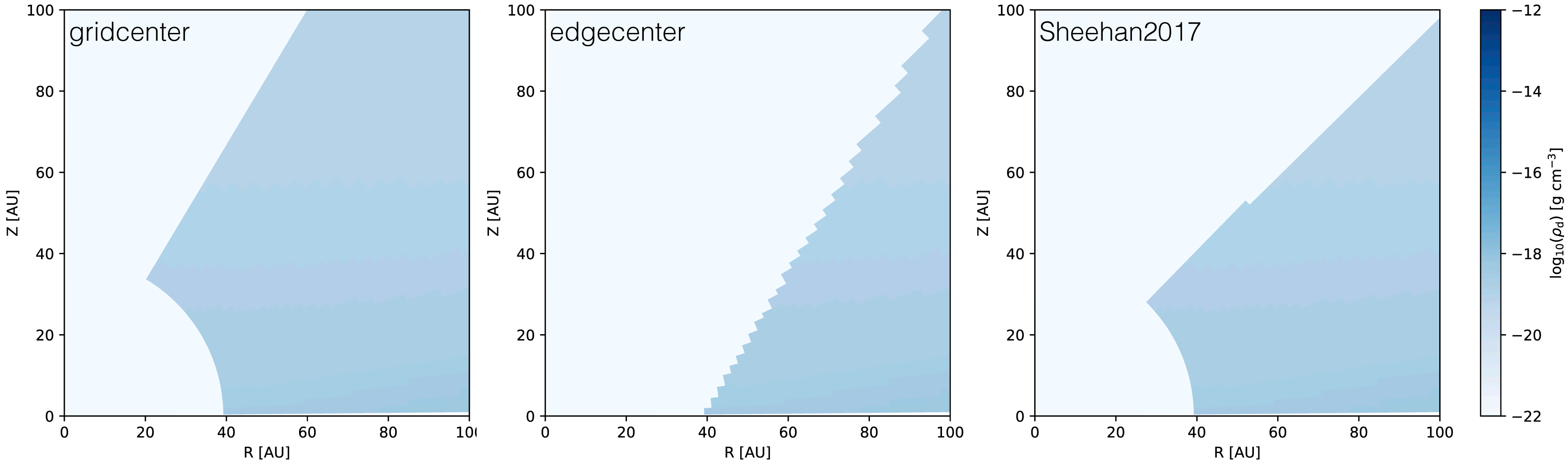

Figure 4.2: Three examples of 2D density maps for different shapes of outflow cavity. In `gridcenter` the outflow cavity starts at the center of the grid, `edgecenter` cavity starts at `rTrunEnv`, the inner radius of the envelope density profile and the `Sheehan2017` is a cavity described in Sheehan & Eisner (2017).

Finally, `galario_check` and `time`, return the Nyquist criterion for computing the synthetic visibilities in the (u, v) locations provided by GALARIO and the function run-time information, respectively.

The following step is to choose the fitting parameters, the range of the space exploration and the initial guess for the parameters. The fitted parameter names are listed in `parname`. These can be parameters from the model setup file and some special parameters as: source distance, inclination, position angle and offset in right ascension (RA) and declination (DEC). `p_ranges` are the limits for each parameter.

```
# Choose fitting parameters and initial values
parname = ['mdisk','rho0Env','gsmax_disk','gsmax_env']
p_ranges = [[-10., -2.],    # log disk dust mass [solar mass]
            [-23., -19.],    # log envelope dust density [g/cm**3]
            [-6., 0.],       # log disk grain size [cm]
            [-6., 0.]]       # log envelope grain size [cm]
```

Additionally, the initial guess for the parameters is assigned to `p0`. The mode of exploration of the initial guess parameter can be defined through the lists: `p_form`, `p_formprior` and `p_sigma`.

```
# initial guess for the parameters
p0 = [-5, -20, -4., -4.]
p_form = ['log', 'lin', 'log', 'log']
p_formprior = ['uniform', 'normal', 'uniform', 'uniform']
p_sigma = [0., 0.5, 0., 0., 0., 0.]
```

The `p_form` sets whether the prior probability `p[i]` is logarithmic (`value = 10**p[i]`) or linear (`value = p[i]`). `p_formprior` sets the functional form of the prior probability distribution. It should be set to `normal` or `uniform` for a Gaussian or rectangular distribution, respectively. `p_sigma` is the width of the Gaussian function.

- **`SiDE` on computer clusters**. `SiDE` has the option `use_mpi` where it is possible to use MPI pools instead of Python threads. This alternative is useful for running MCMC procedures on computer clusters using multiple nodes. To implement this, first it is necessary to add the runtime parameters as number of walkers (`nwalkers`) and the number of walker steps in the main run (`nsteps`) in the fitting Python script.

```
# Runtime parameters
    nwalkers = 240
    nburnin  = 0
```

```
    nsteps   = 100
    verbose  = True
    nthreads = 1
```

The second step it is to setup the Batch script for requesting resources and queuing the Python script on the cluster. One of the clusters used in this study is MPG Supercomputer COBRA, that contains 3,424 compute nodes, 136,960 CPU-cores, 128 Tesla V100-32 GPUs, 240 Quadro RTX 5000 GPUs, 529 TB RAM DDR4 and 7.9 TB HBM2. All compute nodes contain two Intel Xeon Gold 6148 processors (Skylake (SKL), 20 cores @ 2.4 GHz) and are connected through a 100 Gb/s Omni-Path interconnect. More information in the web page `https://www.mpcdf.mpg.de/services/computing/cobra`. The batch system on the HPC cluster COBRA is the open-source workload manager SLURM (Simple Linux Utility for Resource management) that allow to schedule jobs for large and small Linux clusters. An example to submit a job script to SLURM, which will find and allocate the resources required for the job is presented bellow.

```
#!/bin/bash -l

## SiDE example to submit fitting job on SLURM
##
## Run fitting on 60 cores of 2 nodes.
##
## Tested on cobra cluster at MPCDF
#
#SBATCH --job-name=job-test
#SBATCH --time=12:00:00
#SBATCH --partition=medium
#SBATCH --ntasks-per-node=30
#SBATCH --nodes=2
#SBATCH --mem=185000

date

## Load required software
module purge
module load intel
module load impi
module load anaconda
module load mpi4py

## Make sure that radmc3d binary is avaialble
```

```
export PATH=$PATH:~/bin

## Change to model directory, this is used as resource_dir in SiDE
cd ~/MODEL-TEST

pwd

echo "Starting thread:" $SLURM_ARRAY_TASK_ID

srun -n 60 python fitting_script.py start
```

- **Reading and combining chain files**. The outputs generated by `SiDE` as walker position, acceptance fraction and/or posterior probability are stored in ASCII *.dat or binary *.p pickle files. The ASCII file serves as restart file and can be used to track progress of the walkers. If the code abruptly crashes or stops (e.g. by the scheduler on the cluster), then this file can be used to restart the chain from where it left off. This file is continuously updated during run-time and can be used for track progress. Existing ASCII chain files are never overwritten by the fitting routine. The binary output contains more information, e.g. the initial parameters, prior parameter ranges, acceptance fraction, image properties, etc. It is written only when the computation is complete. If the computation was resumed from a restart file, then the walker positions and probabilities from the earlier run are combined with the current data and stored in the file, see Fig. 4.3.
  The following commands give examples for reading ASCII and binary format chain files to `emcee_chain` type objects.

```
from side import tools

# Read ASCII data
results = tools.read_chain_ascii('chain.dat')

# Read binary (pickle) data
results = tools.read_chain_pickle('chain.p')
```

The minimum data stored in a `emcee_chain` object are the following: the chain (parameter values explored by the walkers, with dimension `[nwalkers, nsteps,ndim]`), logarithm of posterior probability (dimension `[nwalkers, nsteps]`), number of walkers (`nwalkers`), steps (`nsteps`) and fitted parameters (`ndim`) and the name of the fitted parameters (dimension `[ndim]`).

To combine chain files from multiple runs can done with:

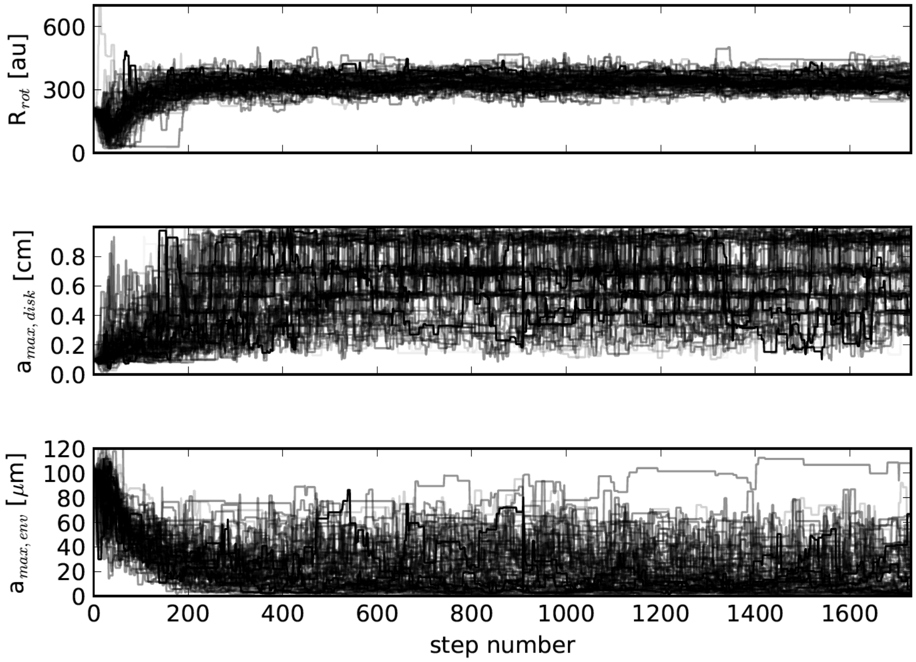

Figure 4.3: Positions of each walker as a function of the number of steps for three free parameters of a test model. The walker positions and probabilities from the several runs are combined to reach ∼1600 steps. The first panel is the rotational radius of the Ulrich density profile. The following two panels are the maximum grain sizes for the disk and envelope respectively.

```
from side import tools
a = side.tools.read_chain_ascii('chain.dat')
b = side.tools.read_chain_ascii('chain_0.dat')
ab = a.__add__(b)
```

The addition operation is not commutative and not associative. It is assumed that the second term follows the first one in time (i.e. walker progression). Chains with different number of walkers can not be added.

- **Model diagnostic plots** The `emcee_chain` class provides methods for plotting the distribution of explored parameters using corner plots, the progression of parameter combinations and the posterior probability value in the chain.
  `plot_chain` shows the walker progression. Figure 4.3 shows the path taken by walkers for each fitted parameters. `plot_corner` shows the posterior parameter distribution. A test example of the posteriori is presented in Figure 4.4. Additionally, `plot_lnprob` plots the posterior probability of models explored by walkers.

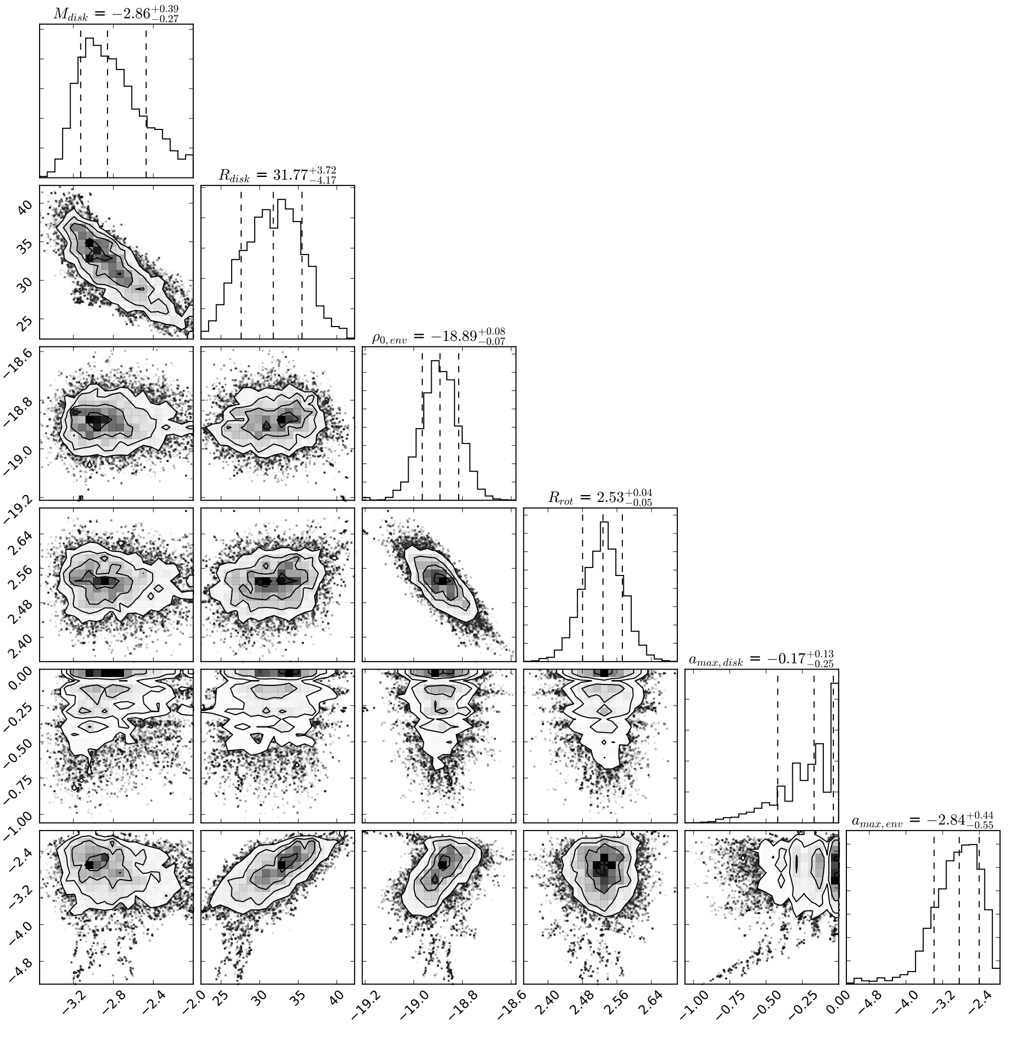

Figure 4.4: Projected posteriori probability distribution functions (PDFs) for every combination of parameter pairs. The free parameters of this test model are: the dust mass of the disk, disk radius, the envelope density, rotational radius of the Ulrich density profile and the maximum grain sizes for the disk and envelope respectively. On the top diagonal, the 1D histograms are the marginalized distributions of the fitted parameters; the vertical dashed lines represent (from left to right) the 16th, the 50th, and the 84th percentiles. The plot shows the posterior sampling provided by 1200 steps, we discard the samples of the burn-in phase.

4.7 Code performance

The following timing tests were done on an Intel(R) Xeon(R) CPU E5-1620 v3 @ 3.50GHz CPU with 16 GB DDR3 ECC RAM, nVidia GM107GL [Quadro K2200] and SATA 6 Gb/s spinning disk.

GALARIO and `emcee` packages both support multiprocessing. The underlying C++ code in GALARIO supports both OpenMP and CUDA parallelisation. The `emcee` code supports single node parallelisation using the multiprocessing Python infrastructure and MPI on single or multiple nodes. By default GALARIO tries to use all available CPU cores for the image to complex plane transformation. The following tests in Table 4.2 show that when `emcee` is used in multiprocessing or MPI modes then GALARIO should be instructed to either use GPU or a single CPU thread. If this is not ensured, then the runtime may increase by a factor of 10, due to resource competition. The number of CUDA core blocks (8 to 32) affect the performance marginally. On the test machine (old, entry level GPU) the MPI CPU mode of GALARIO is almost a factor of 2 faster than GPU computation. Note that in `SiDE` fitting the most time consuming step is the radiative transfer modelling. Nevertheless, it is important to optimize the image to uv-space transformation and model fitting as much as possible.

4.7.1 RADMC-3D

The RADMC-3D code has multiple parameters for speeding up the thermal Monte Carlo radiative transfer computation. By setting the option `ifast` to 1 or 2 will get a faster Monte Carlo simulation, at the cost of being less accurate. In Table 4.3 is presented a computations speed test using 100000 photon packages for the thermal Monte Carlo simulation and the option `modified_random_walk` switched on. The aim of `SiDE` is not to produce high precision radiative transfer models at each modelling step, but to probe a large parameter space in order to find best fit parameters within the model framework (i.e. assumptions on geometry, density distribution, etc.). The user should always recompute the best fit parameter model with much higher number of photon packages and optimization switched off (`ifast` = 0). The `modified_random_walk` flag might still be necessary to deal with optically thick regions.

4.8 Conclusions

We have developed a framework that combines the Markov Chain Monte Carlo fitting with a detailed dust radiative transfer code to model young protostar structure components. With this tool is possible to model multi-wavelength continuum millimeter observations and to create flexible disk+envelope models. The framework has a convenience design that allows the model to be modular and flexible. The disk and envelope structure and the dust properties can be tuned independently of each other, making it suitable for studying the

Table 4.2: Comparison between GALARIO threads using Multiprocessing or MPI.

GALARIO threads	emcee threads	Runtime (s)
`galario.double` + Multiprocessing		
1	1	1044
1	8	305.08
8	1	422.93
8	8	2346.1
`galario.double` + MPI		
1	8	291
1	2	1053
2	4	328
2	2	649
4	2	504.8
8	8	2688
`galario.double_cuda` + Multiprocessing		
8	1	633.5
16	1	636.1
16	8	536.4
32	1	645
`galario.double_cuda` + MPI		
16	2	641
16	8	539

Table 4.3: Single model computed with `nphot`=100000 and modified random walk switched on.

`ifast`	Runtime (s)
1	10.00
2	7.40
3	8.03

effects for example of different envelope density profiles or for testing different dust opacity distributions.

The results of the fit provide probability distributions for the value of each free parameter, estimates of their correlations, and a best-fit model. From the development and testing of the code we have learned:

- The number of free model parameters have to be driven and regulated by the knowledge of the source and previous studies. Increase the number of parameters to fit data-sets may force the model to fit data with unrealistic and nonphysical parameters.

- Before plotting the best set of parameters, first check the posterior probability progression of the chains. If it is necessary increase the number of walkers per parameter. A reasonable number is between 10 and 20 walkers per parameter.

- In the tests we allow the walkers to explore the parameter space for an extended burn-in period of ∼500–1000 burn-in steps, and ∼1000 further steps to sample the posterior. We seek that the walkers converge towards locations of parameter space that fit the data well.

The framework developed in this thesis is also designed to be use in the analysis of high resolution multi-wavelength observations of large samples of disks with ALMA that will allow us to spatially resolve the early growth of solids.

In order to expand the study of grain growth in Class I protostars, we modeled the dust properties in the outer and inner regions of the Class I protostar binary BHB07-11, better known as the **Cosmic Pretzel** (Alves et al., 2017, 2018, 2019). For this purpose, we are using multi-wavelength ALMA observation at a resolution of ∼30 au to determine whether there are spatial variations in the grain size distribution. In the Outlook of this thesis we show the capabilities and advantages of `SiDE` analysing this source.

Chapter 5

Conclusions and future work

5.1 Summary

The gas and dust budget around young protostars plays a fundamental role in the process of planet formation, since these are the ingredients from which planets will form. In this context, the main question that was explored in this thesis was, how early in the star and planet formation process the dust grains start to efficiently coagulate and grow from micron-sized particles to millimeter-size. This thesis focuses on the study of the Class I stage, in which a protostar and disk are still embedded in their natal envelope of gas and dust. In Class I protostars, the envelope and the disk are more–readily modeled at scales of hundreds to thousands of astronomical units. Only by combining large and small scale dust emission with full radiative transfer models we can disentangle the envelope from the protoplanetary disk component and reveal their dust grain properties.
Until this date only three single Class I protostars have been studied with radiative transfer modelling and with multi-wavelength observations to constrain the dust properties in the disk or in the envelope. While Miotello et al. (2014) found dust grains with mm-sizes in the envelope of two Class I protostars using a grid of partial radiative transfer models, Sheehan & Eisner (2018) fix the maximum dust grain size in the envelope to $1\,\mu$m and find disk maximum grain size of the order of centimeters. To better understand the process of the grain growth, it is urgent to increase the sample of modelled protoplanetary disks, as well as the diversity of environmental and internal properties. Motivated by the few studies on grain growth in Class I sources and the lack of self-consistent radiative transfer models, we studied in detail the Class I protostar Per-emb-50.

In Chapter 2 we developed a variety of analytical and radiative transfer models to constrain the physical and dust properties of the embedded disk of Per-emb-50. We adopted two modeling approaches. First we adapted the modelling of Miotello et al. (2014), where the protostar and the disk are modelled as point sources, and only the envelope profile was considered in the radiative transfer model, while in the second modelling we considered the disk and the envelope contribution in the radiative transfer models. For both modeling approaches we use the radiative transfer code RADMC-3D, and we set up a parameter grid, exploring different disk and envelope physical properties and a variety of envelope maximum grain sizes.

We found that the envelope of Per-emb-50 is consistent with a maximum grain size of $a_{\max} < 100\,\mu$m. Even though we find that Per-emb-50 has a $a_{\max}$ of a few hundred microns in the inner envelope, Miotello et al. (2014) find grains with mm sizes in other two Class I protostars in Ophiuchus. Clearly, the study of a larger sample of Class I sources in different star-forming regions and a more rigorous modeling is needed to understand how general and universal is the grain growth process in these stages.

In addition, we also reveal that the inclusion of the envelope is necessary to properly model the thermal emission in the disk. Indeed, the effect of the envelope's thermal emission on the disk (i.e. backwarming), often ignored for Class 0/I protostellar phase, can significantly affect the gas temperature, the gas-phase chemistry and the dust mantle chemistry in young sources. This effect can be very important depending on the envelope density profile, finding that only a radiative transfer modeling can capture this process, while analytical models cannot. In the collapsing envelope model (i.e. Ulrich (1976) profile), the backwarming effect on the outer regions of the disk is weak, but if a power-law envelope is used (Tafalla et al., 2002), the effect is more obvious.

In Chapter 3 we continue the exploration of the properties of the dust in Per-emb-50, where we combined our large scale observations of the envelope with disk scale observations (Segura-Cox et al., 2016). Our detailed radiative transfer modelling of the disk allows us to better determine the temperature profiles and to better constrain the disk parameters in comparison to previous estimations derived from flux-to-mass conversions and analytical models (Segura-Cox et al., 2016; Andersen et al., 2019). We find a new total mass in the disk of 0.14 $M_{\odot}$ (146.6 $M_{\rm Jup}$) with a mass in dust of $468\,M_{\oplus}$, and a disk radius of 38 au. This suggests that the Per-emb-50 disk has enough mass to form giant planets, according to the minimum threshold value of 0.01 $M_{\odot}$ (10.5 $M_{\rm Jup}$) (Weidenschilling, 1977). Concerning dust properties, we put constraints on the level of grain growth between 25 and 38 au in the disk, finding a lower limit of $a_{\max} \geqslant 735\,\mu$m with a power law grain size distribution of q=3.5. The level of grain growth in the innermost disk zone remains unconstrained given that it is optically thick, requiring multi-wavelength observations to determine this. Additionally, we provide a better fit and constraints for the envelope using an Ulrich density profile. We find an envelope rotational radius of ~ 113 au, and a maximum grain size of $26\,\mu$m, which is in agreement with the upper limit found in Agurto-Gangas et al. (2019).

In Chapter 4 is presented the newly developed fitting framework `SiDE` (Simple Disk-Envelope), which uses the radiative transfer tool RADMC-3D to produce synthetic dust maps based on protoplanetary disks observations. `SiDE` offers multiple setup options to generate radiative transfer models, that include for example different density profiles for the envelope component, different grain size distributions for each component, and more. Moreover, it uses Markov Chain Monte Carlo (MCMC) method to fit real interferometric observations. For the development and testing of this tool we used mm-data-sets from

Per-emb-50 and Elias-29. The future of this framework is to be used in the analysis of high resolution multi-wavelength observations of large upcoming samples of disks with ALMA that will allow us to spatially resolve the early growth of solids.

5.2 Future work

In order to expand the study of grain growth in Class I protostars, we decided to model the dust properties in the outer and inner regions of the Class I protostar binary BHB07-11 (Alves et al., 2017, 2018, 2019). BHB07-11 is the youngest member in the star-forming cloud Barnard 59 (B59). It is located at a distance of 163 pc (Dzib et al., 2018) and it is classified as a Class I protostar with a disk embedded in a dusty envelope (Brooke et al., 2007).

The high resolution multi-wavelength observations of Alves et al. (2018) provide a good opportunity to measure the spectral index to determine whether there are spatial variations in the grain size distribution inside and outside the disk. In this chapter we present mm-observations of BHB07-11 with the aim of constraining the grain size distribution on the disk and envelope. This object has been studied previously with single dish observations (Brooke et al., 2007; Román-Zúñiga et al., 2012; Hara et al., 2013), providing information about the envelope physical scales. In Sect. 5.2.1 we describe ALMA observations and ancillary data sets of BHB07-11 used in this analysis. Then, in Sects. 5.2.3 and 5.2.3 we present the modeling setup using `SiDE` and the model work in progress.

5.2.1 Source and Data

Source

BHB07-11 is classified as a Class I protostar from its infrared slope (Brooke et al., 2007). The bolometric temperature is $T_{\rm bol}$= 70±10 K and the distance corrected bolometric luminosity is $L_{\rm bol}$ = 3.7±0.3 $L_\odot$ (Myers & Ladd, 1993). From previous observations, the large scale envelope has a physical scale close to 3000 au (Román-Zúñiga et al., 2012) and it presents a molecular outflow perpendicular to the rotation plane of the envelope (Hara et al., 2013; Alves et al., 2017). Literature values for envelope mass, disk mass, disk inclination, and other parameters are presented in Table 5.1.

ALMA data

We used the dust continuum emission from ALMA observations presented in Alves et al. (2017, 2018). For the propose of this work we used the data sets centered at 97.5 GHz (Band 3), 233 GHz (Band 6) and 343.5 GHz (Band 7).

Band 3 observations were performed on November 14, 2017 using the 44 antennas from the main array. The uncertainty in the absolute flux density is 10 %. Band 6 observations were carried out on the 19th September of 2015 using 35 antennas of the array. Band 7 observations were completed on May 17th, 2017 using 45 antennas. In order to have a

Table 5.1: BHB07-11 Parameters from literature

Parameter	Value	References
RA_{J2000}	17:11:23.1057 (VLA 5a)	Alves et al. (2019)
Dec_{J2000}	27:24:32.818 (VLA 5a)	Alves et al. (2019)
$L_\star$ ($L_\odot$)	3.5	Alves et al. (2019)
$T_\star$ (K)	3336	
$M_\star$ ($M_\odot$)	2.25±0.13	Alves et al. (2019)
$R_\star$ ($R_\odot$)	5.6	Hara et al. (2013)
$M_{disk+env}$ ($M_\odot$)	0.17±0.06	Alves et al. (2018)
M_{disk} ($M_\odot$)	0.08	Alves et al. (2019)
R_{disk} (au)	90	Alves et al. (2019)
R_{env} (au)	2900^a	Román-Zúñiga et al. (2012)
PA_{disk} (deg)	138±15	Alves et al. (2018)
i_{disk} (deg)	48	Alves et al. (2018)
PA_{env} (deg)	167	Alves et al. (2018)
i_{env} (deg)	55	Alves et al. (2018)

(^{a}) The deconvolved size of 18×17 arcsec obtained from IRAM/MAMBO-II 1.2 mm continuum observations using a distance of 163 pc (Román-Zúñiga et al., 2012).

Table 5.2: Single dish fluxes BHB07-11

Wavelength (mm)	Flux (Jy)	size (arcsec)	Reference
0.87	15.7	21×21	(Redaelli et al., 2017)
1.20	7.05	18×17	(Román-Zúñiga et al., 2012)

data set with the same spatial scales, for the multi-wavelength analysis and modeling, we performed the same map cleaning as in Alves et al. (2018). We used a common *uv* range for all the observations, from 27 to 1310 kλ. The synthesized beams for Band 3, 6, 7 are 0.22"×0.17", 0.26"×0.15", 0.21"×0.18", respectively. Those beams correspond to an average spatial resolution of 32.6 au.

Ancillary Data Sets

We used 1.2 mm (250 GHz) observations with the MAMBO-II bolometer at the 30m IRAM telescope. The dust single dish data obtained by Román-Zúñiga et al. (2012) has a beam size of 11". Additionally, we used the LABOCA dust thermal emission map with APEX telescope at 870 μm (Redaelli et al., 2017). These data have a spatial resolution of 21.2". The 870 μm continuum maps are presented in Fig. 5.1. Single dish fluxes are presented in Table 5.2.

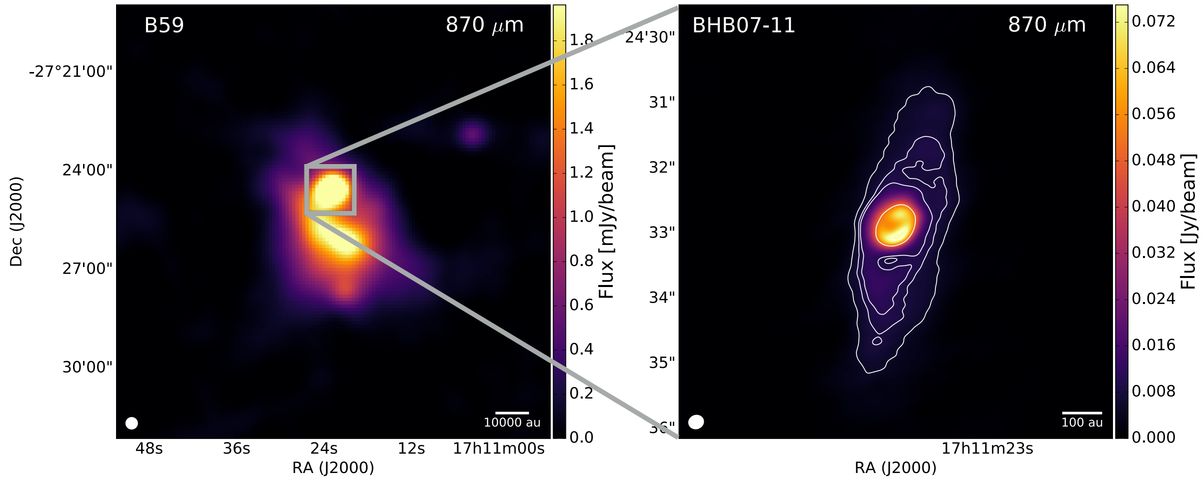

Figure 5.1: (Left) APEX continuum map of the star-forming cloud B59 at 870 μm. (Right) Zoom-in to the inner envelope and disk environment of BHB07-11. The map is adapted from Alves et al. (2018).

5.2.2 Observational Analysis

Spectral index map

We compute the millimeter spectral index $\alpha_{\rm mm}$ through the flux ratio between two wavelengths:

$$\alpha_{\rm mm} = \frac{\ln \mathrm{F}_1 - \ln \mathrm{F}_2}{\ln \nu_1 - \ln \nu_2}. \tag{5.1}$$

In this case, we use the data sets with the largest frequency separation (Band 3 and 7). Following Alves et al. (2018), we smoothed the data to a common circular beam of 0.25" in order to calculate the spectral index map. Fig. 5.2 shows the spatial distribution of the spectral index in the disk and extended emission. The minimum spectral index near the center of the disk and also reported by Alves et al. (2018) is 2.67±0.01 while in the outer regions of the disk varies from 3.01±0.02 to regions where it is ∼3.5. From the map we can infer that there are some variations in the spectral index from the inner to the outer regions. To quantify these values we performed a simple parametric model in order to distinguish a representative spectral index coming from the disk and the extended emission.

Parametric model

In order to quantify the spectral index differences in the envelope and disk of BHB07-11, we performed an observational analysis of the visibilities. We plot the real visibility of the two most separeted wavelengths as a function of the deprojected baseline length (*uv*-distance).

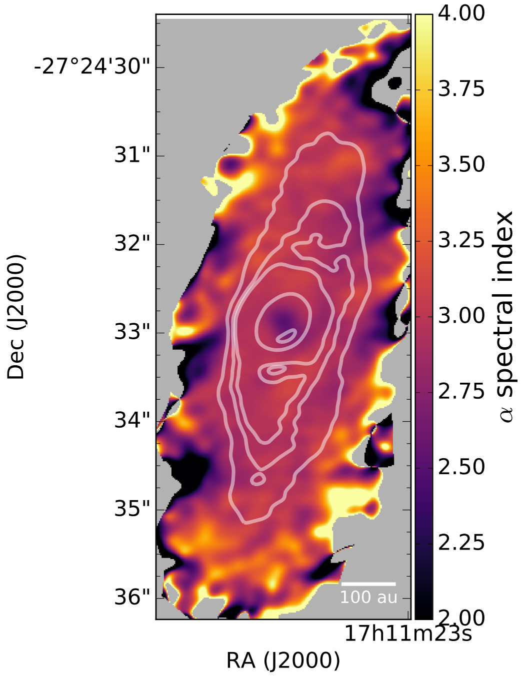

Figure 5.2: Spectral index map obtained from the emission between Bands 3 and 7. The Stokes I maps were smoothed to a common circular beam of 0.25 arcsec prior to spectral index computation. The contours show the Stokes I Band 7 flux as in Fig. 1.

The deprojection is given by $R{=}\sqrt{d_a^2 + d_b^2}$, where:

$$\begin{aligned} d_a &= \sqrt{u^2+v^2}\sin\phi, \\ d_b &= \sqrt{u^2+v^2}\cos\phi\cos i, \\ \phi &= \arctan(v/u) - PA \end{aligned} \tag{5.2}$$

The values for inclination i, and position angle, PA, are presented in Table 5.1. BHB07-11 has two clear components in the continuum map in both wavelengths. If we translate this into the visibilities, the inner envelope component dominates the short baselines, $<$100 kλ, while the disk physical scales dominates the long baselines. The parametric model consists of an extended emission described by a Gaussian, and an unresolved disk (point source) that has constant flux at large baselines. Therefore, the combined amplitude profile, that depends on the uv distance, defined as $\sqrt{u^2+v^2}$, and frequency, ν, is described by:

$$f(uv,\nu) = F_e \left(\frac{\nu_2}{\nu_1}\right)^{\alpha_e} \exp\left(\frac{-(uv)^2}{2\sigma^2}\right) + F_d \left(\frac{\nu_2}{\nu_1}\right)^{\alpha_d}, \tag{5.3}$$

where $F_{\rm e}$ and $F_{\rm d}$ are the flux densities from the Gaussian emission (inner envelope) and point source emission (unresolved disk), respectively, $\alpha_{\rm e}$ and $\alpha_{\rm d}$ are the spectral indexes of the two components, and σ is the width of the Gaussian given by $\sigma \approx$ FWHM/2.355.

We used the Markov chain Monte Carlo (MCMC) method, which is implemented in the python package EMCEE (Foreman-Mackey et al., 2013a), to fit the data. We explore the parameter space for F_e, σ and α_e, while F_d and α_d where fixed to 0.005 Jy and 2.7, respectively. The value of F_d is calculated taking the average flux at long baselines, while α_d is the value calculated by Alves et al. (2018) for the inner central disk.

In this study, we perform the fit using eight hundred chains for a three-dimensional parameter space. We initialize the chains around a prior that takes into account the shape of the visibilities and the previous knowledge about the parameter values. After initialization, the chains evolve during a burn-in period of 1000-1500 steps and then we take 2000-3000 steps to accomplish a good posterior probability distribution function (PDF).

Results parametric model

We present the staircase plot with the 1D and 2D marginalized posterior PDFs and a comparison between the observed and the model visibilities at 1.29 and 3.07 mm in Fig. 5.3. We present the best-fit parameters found for this parametric model in Table 5.3. We can constrain the envelope flux contribution of 0.33 Jy and the physical size of the region where the envelope emission arises, which has a 1-σ width of 43 kλ (820 au) and corresponds to the diameter of the flattened structure around the binary protostar. The value for the envelope spectral index is α_e=3.1±0.1 with an uncertainty calculated using a simplistic approximation for non-correlated errors of ±0.1.

Table 5.3: Parameters derived from the parametric model

Source	F_e (Jy)	σ (kλ)	α_e
BHB07-11	$0.34^{+0.002}_{-0.002}$	$43.02^{+0.22}_{-0.21}$	$3.17^{+0.01}_{-0.01}$

This result suggests a variation in dust grain properties between the two zones and that dust grains may have grown from an initial ISM-like dust population. Additionally, we can associate the observational value of the spectral index in the disk and envelope with the dust opacity index β calculated between 1.29 and 3.07 mm. Fig. 5.4 shows β as a function of the maximum grain size a_max. This relation between the a_max and β may suggests that the grain size in the disk and envelope is $\geqslant$300 μm.

To fully understand the dust and physical properties in BHB07-11, we will perform a full radiative transfer modelling using the framework `SiDE`.

5.2.3 `SiDE` Modeling

We are performing a full radiative transfer model on BHB07-11 in order to fit Bands 3,6,7 data simultaneously using the fitting framework `SiDE`. We used a physical model that consists of a protostar, disk, flattened zone, envelope and outflow cavity. We compute all the emission contributions using the radiative-transfer tool RADMC-3D from Dullemond et al. (2012). Details of each physical component will be discussed in the following sections.

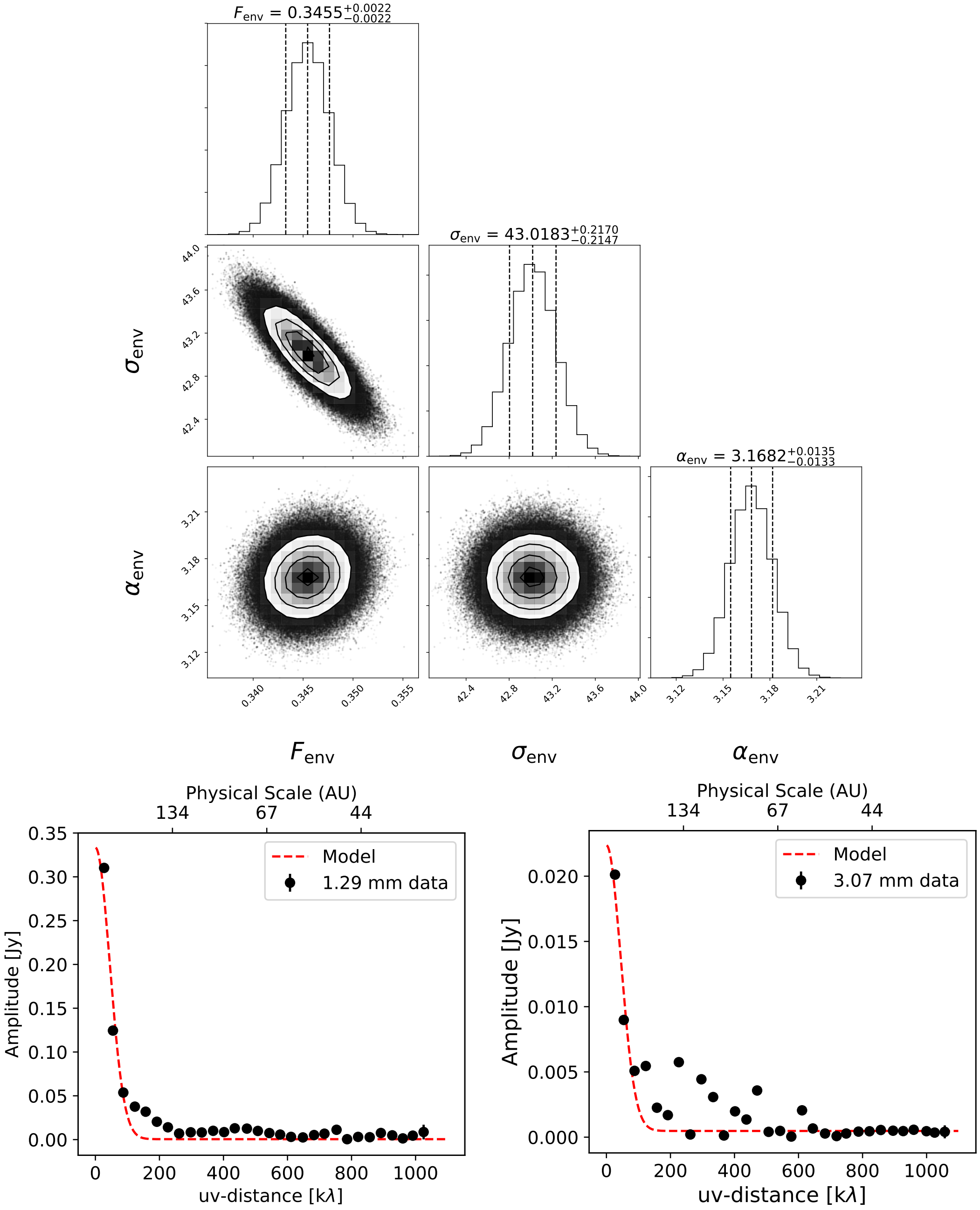

Figure 5.3: Upper panel: Staircase plot showing the marginalized and bi-variate probability distributions resulting from the fit for binned the visibilities of BHB07-11. Bottom panels: ALMA BHB07-11 binned visibilities as a function of uv-distance or, deprojected baseline. Red dashed lines represent the parametric model.

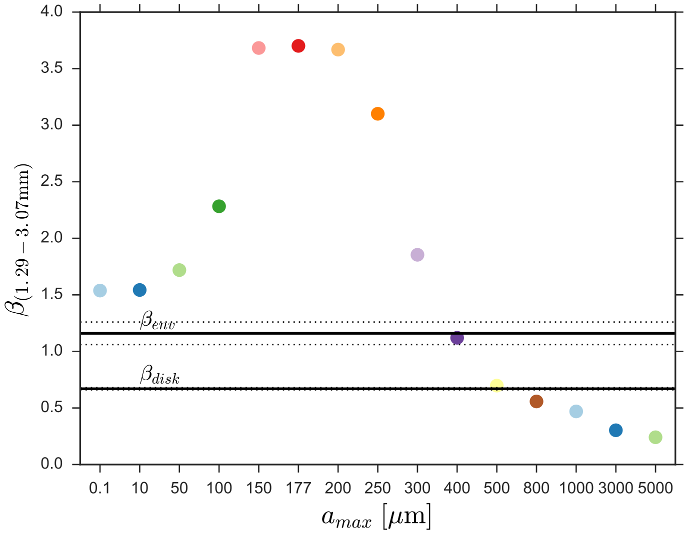

Figure 5.4: Spectral index β of the dust opacity calculated between the wavelengths of 1.29 mm and 3.07 mm as a function of the maximum grain size, for a grain size distribution n(a) $\propto a^{-3.5}$ characterised by a minimum grain size of 0.1 μm. The black solid lines represent the spectral index for the disk derived in Alves et al. (2018) and the envelope spectral index fitted by the parametric model.

Protostar parameters and disk model

The properties of the central protostar are given by previous SED modelling assuming that it emits black body radiation. We used the stellar radius from (Hara et al., 2013) while the stellar luminosity from Alves et al. (2019) is assumed to derive the stellar temperature.
Additionally, we adopt a disk model heated by its protostellar radiation. The surface density profile $\Sigma(r)$ is modeled as a truncated power law following Eq.3.5 with a power exponent of the surface density distribution p=1 and Σ_0 is scaled to accommodate the total mass of the disk $M_{\rm disk}$ which is a free parameter. The 2D volume density with an exponential vertical profile is defined by Eq.3.4 where H_p is the pressure scale height and is defined as H_p/r=0.1(r/r_{h_p})$^{\phi}$. In H_p definition the r_{h_p} is the reference radius and it sets at 50 au while the flaring index of the disk ϕ is set to 1.14. The outer radius of the circumbinary disk is estimated in Alves et al. (2019) and is fixed in the model to 90 au.

Envelope and flattened structure model

The envelope properties of BHB07-11 have been studied in the past with single dish observations. Riaz et al. (2009) and Hara et al. (2013) modeled a envelope radius of 4000 and 2300 au, respectively. In our model we set an average and conservative envelope radius taking into account the previous envelope sizes but using the deconvolved size of 18″ from (Román-Zúñiga et al., 2012), which at B59 distance is around 2900 au.
In order to model the flattened and extended emission around the disk a density structure

Table 5.4: Model set up exploration

Parameter	Unit	Limits	Initial prior value	Prior mode - σ	exploration space
$M_{\rm disk}$	($M_\odot$)	10^{-5} – 0.01	8×10^{-4}	uniform	log
$\rho_0^{\rm env}$	($\rm g\,cm^{-3}$)	10^{-20} – 10^{-18}	1.5×10^{-19}	normal	lin
$R_{\rm rot}$	(au)	50 – 600	400	uniform	lin
$a_{\rm max}^{\rm disk}$	(cm)	10^{-4} – 1.0	1.09	uniform	log
$a_{\rm max}^{\rm env}$	(cm)	10^{-4} – 1.0	1.39	uniform	log

Parameter description: ($M_{\rm disk}$) Disk dust mass, ($\rho_0^{\rm env}$) envelope central density, ($R_{\rm rot}$) envelope rotational radius, ($a_{\rm max}^{\rm disk}$) disk maximum grain size and ($a_{\rm max}^{\rm env}$) envelope maximum grain size.

given by a Ulrich (1976) is used. The 2D density profile follows the equation:

$$\rho_{\rm env}(r,\theta) = \rho_0 \left(\frac{R_{\rm rot}}{r}\right)^{3/2} \left(1+\frac{\cos\theta}{\cos\theta_0}\right)^{-1/2} \left(\frac{\cos\theta}{2\cos\theta_0}+\frac{R_{\rm rot}}{r}\cos^2\theta_0\right)^{-1}, \tag{5.4}$$

where ρ_0 is the density in the equatorial plane at the centrifugal radius $R_{\rm rot}$ of the envelope, and θ_0 is the solution of the parabolic motion of a particle.

Dust opacity

We adopt a dust population characterized by a distribution of grains with different sizes. We used a truncated power-law distribution $n(a) \propto a^{-q}$, between a minimum and a maximum grain size, $a_{\rm min}$ and $a_{\rm max}$ respectively. We implemented a chemical composition of a silicate, carbonaceous material and water ice in a 1:2:3 volume fractional ratio to be consistent with our previous analyzed source. Additionally, we set $a_{\rm min}$=0.1 μm and we use q=3.5 to describe the dust in the envelope and disk. $a_{\rm max}^{\rm disk}$ and $a_{\rm max}^{\rm env}$ are free parameters in the modelling.

Preliminary results

We performed a full RADMC-3D modeling using the framework `SiDE` presented in Chapter 4. We set a physical model that consists of a protostar, disk, flattened envelope and outflow cavity. The limits for each free parameter and prior mode are presented in Table 5.4. The limits and initial priors are constrained by the parametric model, radiative transfer model tests and previous studies on the source. We used two prior modes, uniform and with a normal distribution. In the case of the normal distribution we report the standard deviation σ. The last column in Table 5.4 shows the exploration space mode (logarithmic or linear) for each parameter. In this first attempt model we fix the radius of the disk to 90 au based on Alves et al. (2018), and we simultaneously fit the 1.29 and 3.07 mm data-sets. In Fig. 5.5 we present a staircase plot showing the posterior PDF computed from the chain, after 600 steps. The fit will need at least 2000 more burn-in steps to sample properly the posterior.

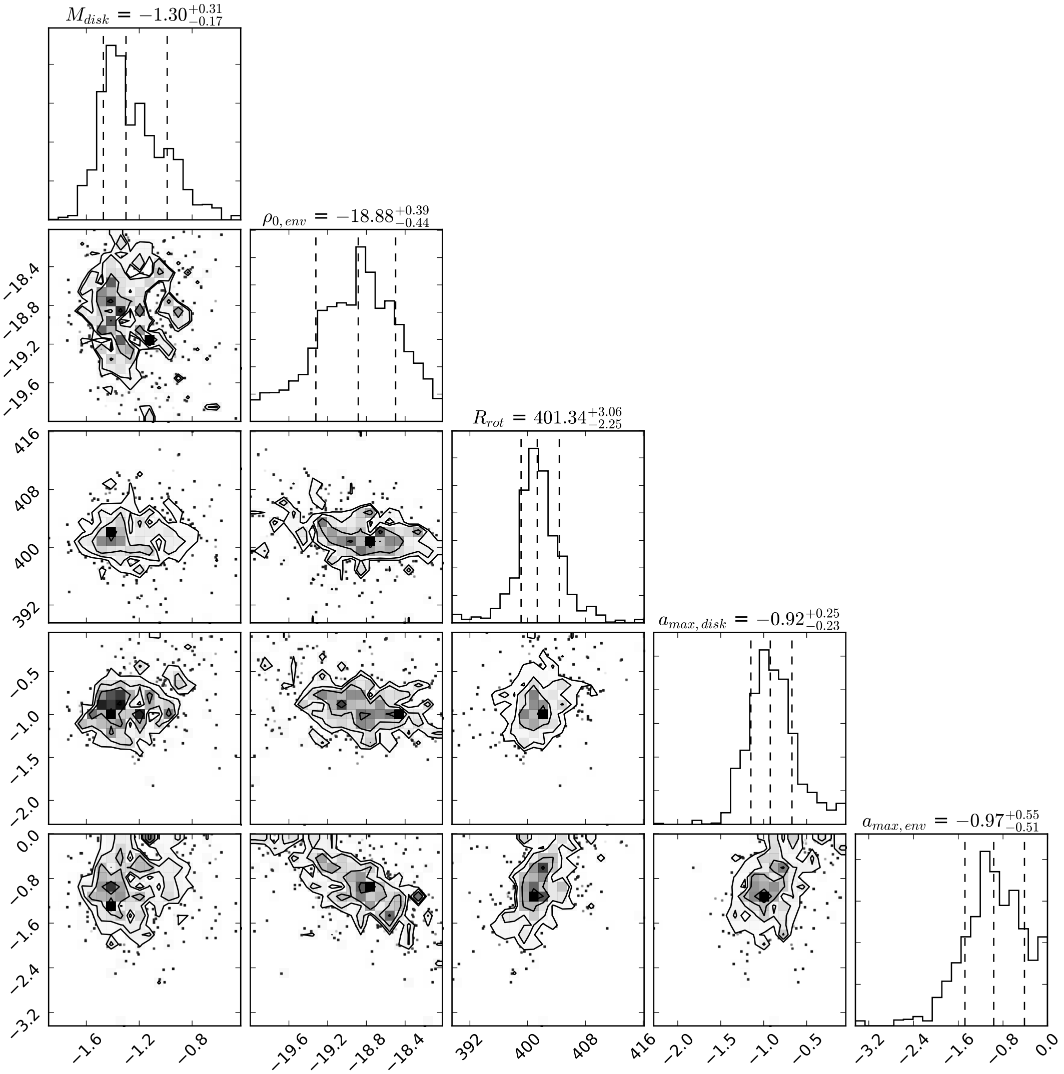

Figure 5.5: Preliminary projected posterior pdf for every combination of parameter pairs for BHB07-11. On the top diagonal, the 1D histograms are the marginalized distributions of the fitted parameters; the vertical dashed lines represent (from left to right) the 16th, the 50th, and the 84th percentiles. The 2D density plots represent the bi-variate distributions for each pair of parameters, with one dot representing one sample. The plot shows the posterior sampling provided by 600 steps, we discard the first 200 samples of the burn-in phase.

5.3 Future perspectives

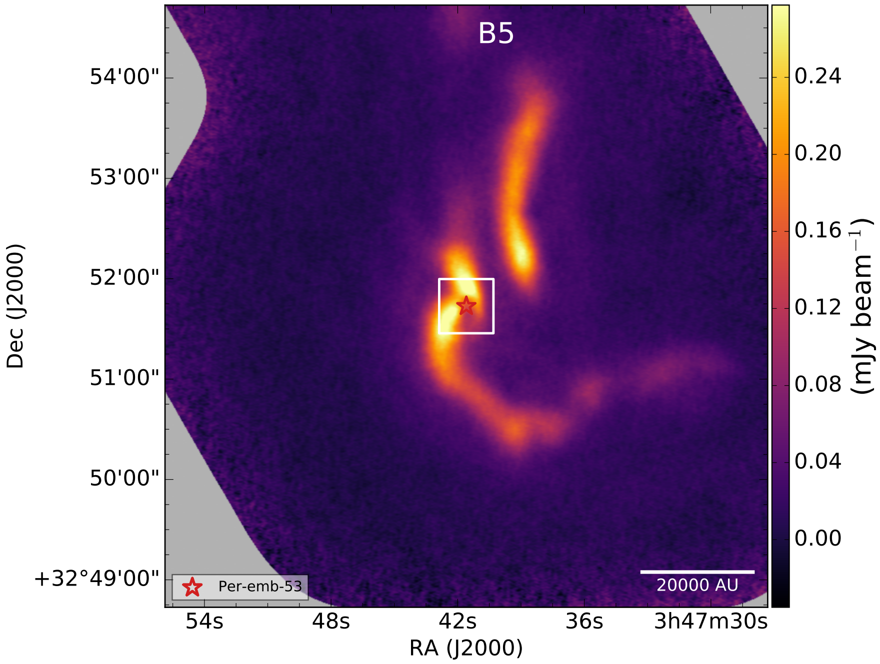

Figure 5.6: NH_3(1,1) map of the Class I protostar Per-emb-53 from Pineda et al. (2015)

Class I protostars are the perfect laboratories to study the evolution of the dust and grain growth in the early stages of star formation. Using a combination of ALMA compact and extended configurations will help to better spatially constrain the transition zone between disk and envelope, which has not been studied in detail. The radiative transfer models and framework developed in this dissertation are crucial to understand the physical structure and dust properties in the forthcoming high resolution and sensitive observations on protostellar disks.

Furthermore, molecular transitions of $C^{17}O$, SO_2 and cold CH_3OH (Artur de la Villarmois et al., 2019) can help us to understand the envelope thermal emission onto the disk, its backwarming effects, and how it affects the gas phase chemistry and the dust icy mantle chemistry, as well as the disk-envelope kinematics. This is why it is important to increase the sample of Class I protostars, for example within Perseus, but in different environments than Per-emb-50. Interesting is to explore the environmental effect on dust grain growth, for example, taking into account quiescent isolated dust environments to more complex surroundings as in Per-emb-53 (see Fig.5.6). The comparison of these kind of environments are very important to understand the previous observations of Per-emb-50, and will help us to differentiate the dust properties in the inner envelope and disk as well.
In order to inform our radiative transfer models, molecules such as N_2H^+, which is a high density tracer, will help us to reveal the true structure of the envelope at these scales, while

transitions of CH_3OH, CH_3CN and CH_3CCH, if detected, will provide an additional check on the gas temperature of the inner envelope via rotational diagrams.

Additionally, it would be important to derive independent constraints of the mm-spectral index and physical properties such as density and temperature in the inner envelope and disk scales of Class I protostars in a different environment than Perseus. Observations, for example Lupus I (see Fig.5.7), will significantly increase the sample of Class I sources on which a similar analysis has been done (Agurto-Gangas et al., 2019; Miotello et al., 2014). This will provide new cases to understand and clarify the apparent disagreement on the maximum grain size within the envelope determined in the latest observations.

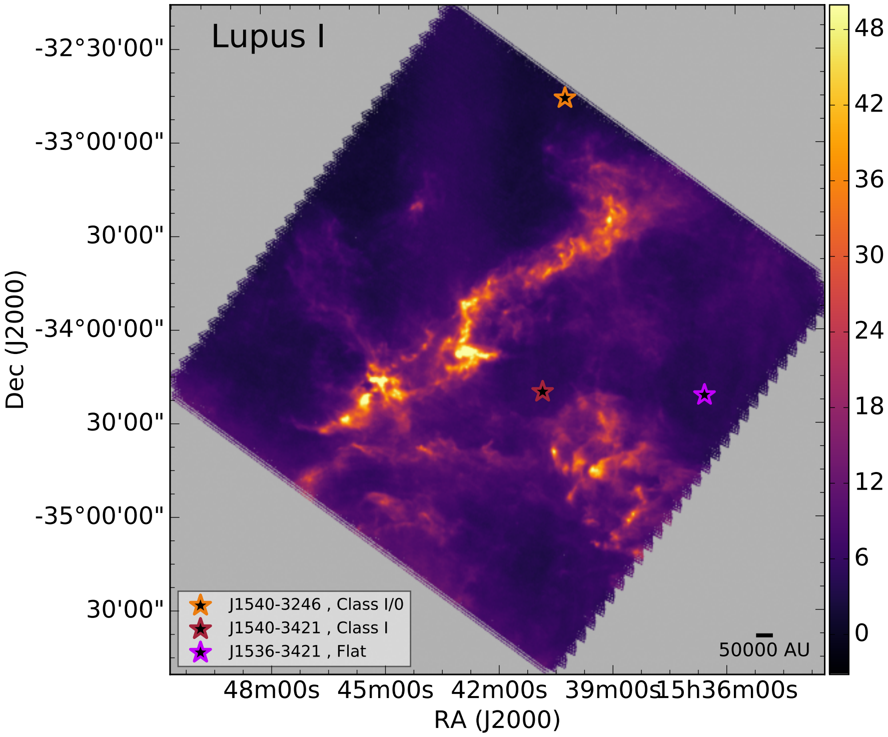

Figure 5.7: *Herschel* SPIRE 500 μm map of the dust continuum emission of the Lupus I cloud, which includes three Class I protostars (marked by stars).

As a final remark, I think that the future of star and planet formation lies in the study of young protostars through multiple wavelengths using different instruments and techniques. One of the most interesting results in the last couples of years were reveled using the combination of millimeter observations with infrared images to determine the properties of the building blocks of planets. The analysis on the T Tauri star PDS 70 made by Isella et al. (2019) and their sharp view of a planet-forming disk is an excellent example of how well can optical NIR and sub-mm observations complement each other for a more profound and complete analysis. They probe diverse aspects of planet accretion processes and put constraints on physical parameters as disk dust mass and radius. Forthcoming observations of nearby young disks featuring gaps and rings might reveal more infant planets interacting with their dusty surrounding material.

Appendix A

Physical and astronomical constants

A.1 Physical & astronomical constants

$$\mathrm{G} = 6.67430(15) \times 10^{-11} \frac{\mathrm{m}^3}{\mathrm{kg} \cdot \mathrm{s}^2} \tag{A.1}$$

$$\mathrm{h} = 6.62606957 \times 10^{-34}\, \frac{\mathrm{m}^2 \cdot \mathrm{kg}}{\mathrm{s}} \tag{A.2}$$

$$1\,\mathrm{au} = 1.5 \times 10^{8}\,\mathrm{km} \tag{A.3}$$

$$1\,\mathrm{L}_{\odot} = 3.889 \times 10^{26}\,\mathrm{W} \tag{A.4}$$

$$1\,\mathrm{W} = 1\,\frac{\mathrm{J}}{\mathrm{s}} = 1\,\frac{\mathrm{kg} \cdot \mathrm{m}^2}{s^3} \tag{A.5}$$

$$1\,\mathrm{M}_{\odot} = (1.98855 \pm 0.00025) \times 10^{30}\,\mathrm{kg} \tag{A.6}$$

$$1\,\mathrm{R}_{\odot} = 6.955 \times 10^{8}\,\mathrm{m} = 0.0046491\,\mathrm{au} \tag{A.7}$$

$$1\,\mathrm{GHz} = 10^{9}\mathrm{Hz} \tag{A.8}$$

$$1\,\mathrm{k_B} = 1.380649 \times 10^{-23}\,\frac{\mathrm{J}}{\mathrm{K}} \tag{A.9}$$

$$1\,\mathrm{Jy} = 10^{-26}\,\frac{\mathrm{W}}{\mathrm{m}^2 \cdot \mathrm{Hz}} \tag{A.10}$$

Appendix B

Chapter 2

B.1 Error estimate of the spectral index of the observed flux densities

The spectral index of the observed flux densities α_{mm} can be approximated using the flux density at two wavelengths. In this appendix, we discuss the error propagation from the observational uncertainty to the deduced α_{mm} value. Let F_1 and F_2 be the flux density at frequencies ν_1 and ν_2 , α_{mm} can be expressed as in Equation (1):

$$\alpha_{\mathrm{mm}} = \frac{\ln \mathrm{F}_1 - \ln \mathrm{F}_2}{\ln \nu_1 - \ln \nu_2}. \tag{B.1}$$

We assume that the fluxes F_1 and F_2 are independent and that σ_{F1} and σ_{F2} are their standard deviations; using the error propagation we obtain

$$\sigma_\alpha^2 = \left|\frac{\partial \alpha}{\partial \mathrm{F}_1}\right|^2 \sigma_{F1}^2 + \left|\frac{\partial \alpha}{\partial \mathrm{F}_2}\right|^2 \sigma_{F2}^2\,. \tag{B.2}$$

Taking the partial derivative of Equation (A.1), we obtain

$$\frac{\partial \alpha}{\partial \mathrm{F}_1} = \frac{1}{(\ln\nu_1 - \ln\nu_2)\mathrm{F}_1}, \tag{B.3}$$

$$\frac{\partial \alpha}{\partial \mathrm{F}_2} = \frac{1}{(\ln\nu_1 - \ln\nu_2)\mathrm{F}_2}. \tag{B.4}$$

Substituting equation A.3 and A.4 in equation A.2, the uncertainty of the derived α_{mm} is then:

$$\sigma_\alpha^2 = \left(\frac{1}{\ln\nu_1 - \ln\nu_2}\right)^2 \left(\frac{\sigma_{F1}^2}{\mathrm{F}_1^2} + \frac{\sigma_{F2}^2}{\mathrm{F}_2^2}\right). \tag{B.5}$$

Figure B.1: Representation of the MCMC results for Per-emb-50. On the top diagonal, the 1D histograms are the marginalized distributions of the fitted parameters; the vertical dashed lines represent (from left to right) the 16th, the 50th, and the 84th percentiles. The 2D density plots represent the bi-variate distributions for each pair of parameters, with one dot representing one sample. The plot shows the posterior sampling provided by 1000 steps of the 400-walkers chain (750 burn-in steps were performed to achieve convergence).

B.2 *emcee* implementation

To compute the posterior distribution for all the free parameters, we use a variant of the Markov Chain Monte Carlo (MCMC) (Mackay, 2003; Press et al., 2007) algorithm, which is widely known and efficient in finding a global maximum for a range of posteriors. We follow the affine-invariant ensemble sampler for MCMC by Goodman & Weare (2010), which basically transforms highly anisotropic and difficult-to-be-sampled multivariate posterior probability distribution function (PDFs) into isotropic Gaussians. The immediate advantage is that it is possible to simultaneously run many Markow chains (*walkers*) that will interact in order to converge to the maximum of the posterior.

This algorithm involves an ensemble $S = \{X_k\}$ of simultaneously evolving K walkers, where the transition distribution for each walker is based on the current position of the other $K - 1$ walkers belonging to the complementary ensemble $S_k = \{X_j, \ \forall j \neq k\}$. The position of a walker $X_k(t)$ is updated as follows:

$$X_k(t+1) = X_j + Z(X_k(t) - X_j), \tag{B.6}$$

where $X_j \in S_k$ and Z is a random variable drawn from a distribution that does not depend on the covariances between the parameters.

In this study we adopted an ensemble of 400 walkers, and let MCMC evolve for an initial burn-in phase. The burn-in phase is needed to allow MCMC to perform a consistent sampling of the space of parameters and to find the posterior maximum. To achieve the posterior maximum is needed to introduce the term: autocorrelation-time[1], which is a direct measurement of the number of the posterior PDF evaluations needed to produce independent samples of the target density. For the analysis of Per-emb-50, 750 burn-in steps were performed to achieve convergence. Fig. B.1 presents a staircase plot, using the Python module *corner* by Foreman-Mackey (2016), showing the marginalized and bivariate probability distributions resulting from the fit for Per-emb-50.

---

[1] Note: The longer the autocorrelation time, the larger the number of the samples we must generate to obtain the desired sampling of the posterior PDF.

B.3 Full radiative transfer models

The models presented in this appendix were created using a simple python module to set up RADMC-3D for disk plus envelope systems, `SimpleDiskEnv`[2]. Figures from B.2–B.6 show the best 36 models from a total of 288 for each maximum grain size (0.1,50,100,300,1000 μm).

B.4 Backwarming effect

We studied the net effect of the envelope on the disk temperature using a RADMC-3D toy model of a Class I protostar. As mentioned in Butner et al. (1994), the envelope can have an important backwarming effect on the disk, affecting the outer edges of the disk with a flat temperature distribution.

To probe this effect, we first modeled a disk of 25 AU without an envelope and with a distribution of dust grains in the disk with a maximum size a_{max}^{disk}=1 cm. Then we add a 1.3 $M_\odot$ envelope, with a Tafalla et al. (2002) density profile and grain sizes with a_{max}^{env}=100 μm. The inner edge of the envelope and the outer radius of the disk are the same. To compare and quantify the effect, we model a disk with the same characteristics but with a density profile of a collapsing envelope defined by Ulrich (1976). Fig D.1. shows the temperature structure (in cylindrical coordinates) for both of these cases. In the left panels (disk only) we can see that the outer regions of the disk are around 20–30 K. In the right upper panel (disk+envelope) using the Ulrich envelope structure, the temperature increases to 40–60 K. In the case of the model with a Tafalla et al. envelope structure the effect is quite strong, reaching disk outer temperatures of 120–140 K.

---

[2] `https://gitlab.mpcdf.mpg.de/szucs/SimpleDiskEnv`

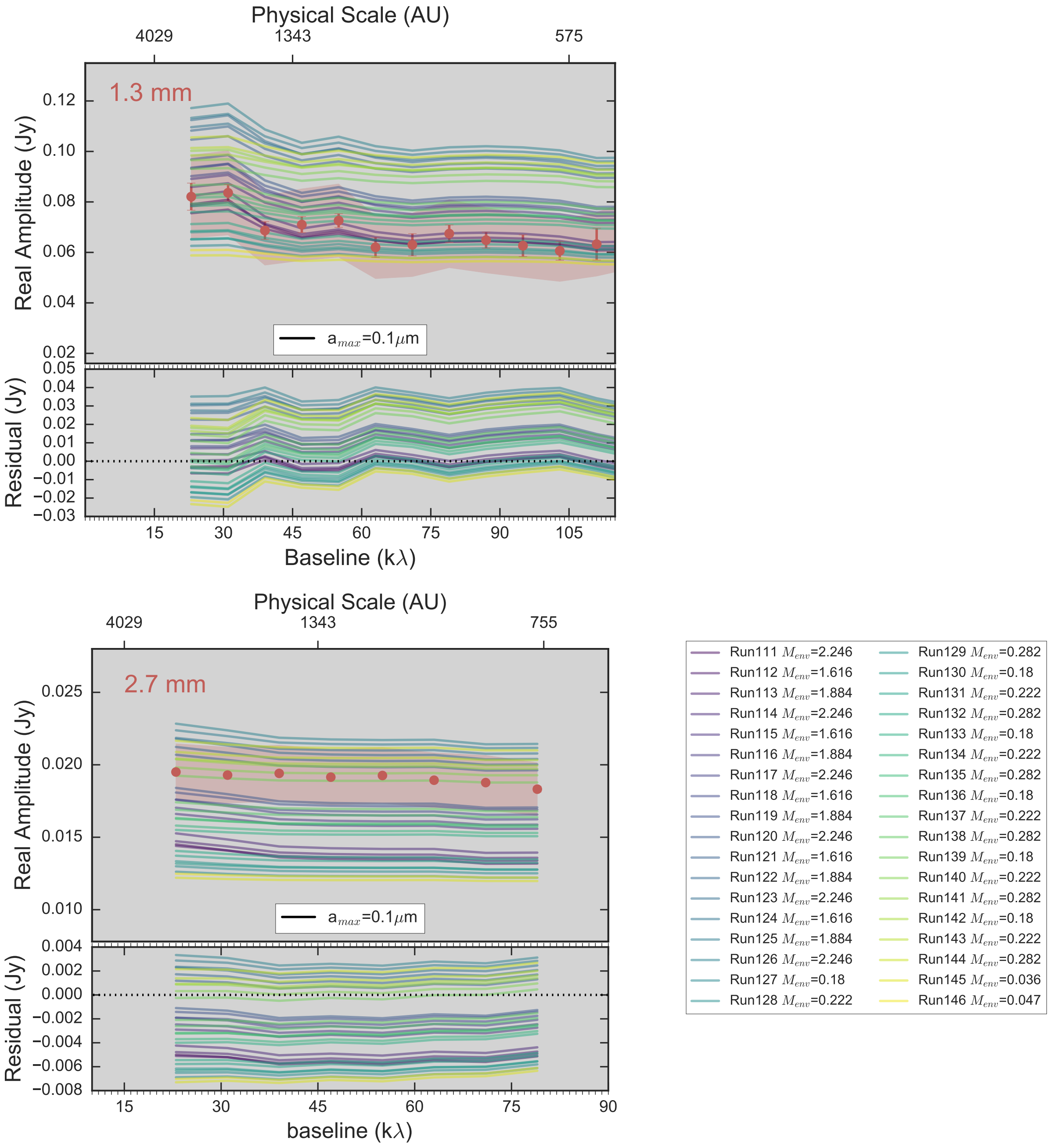

Figure B.2: Full radiative-transfer models for a_{max}=0.1μm. The name of the model and derived envelope mass are in the right panel. The color gradient represents the χ^2 from low (blue) to high values (yellow), that were used only as reference. After visual inspection, we chose the best models from the green area.

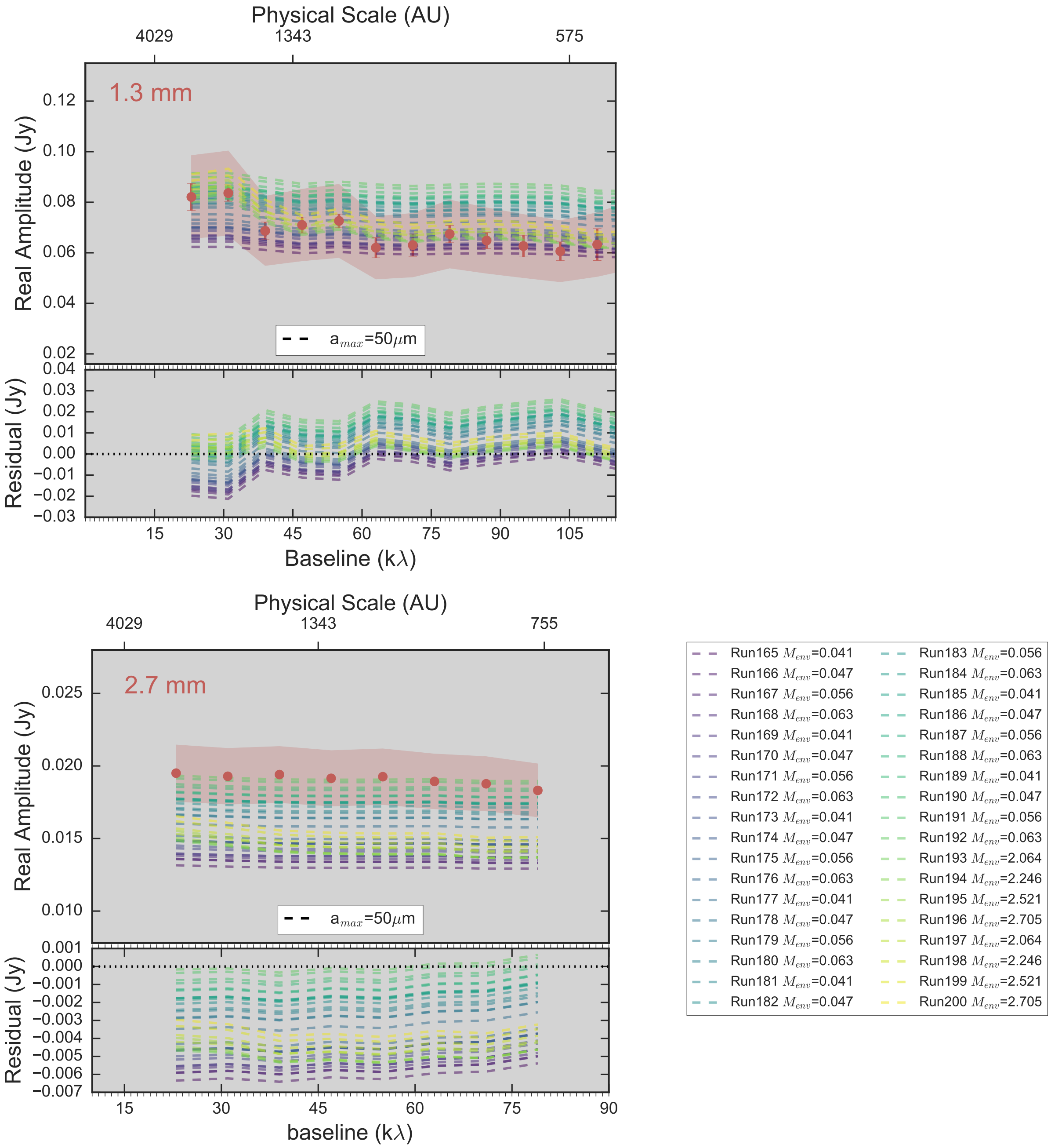

Figure B.3: Full radiative-transfer models for a_{max}=50μm. The name of the model and derived envelope mass are in the right panel. The color gradient represents the χ^2 from low (blue) to high values (yellow), that were used only as reference. After visual inspection, we chose the best models from the green area.

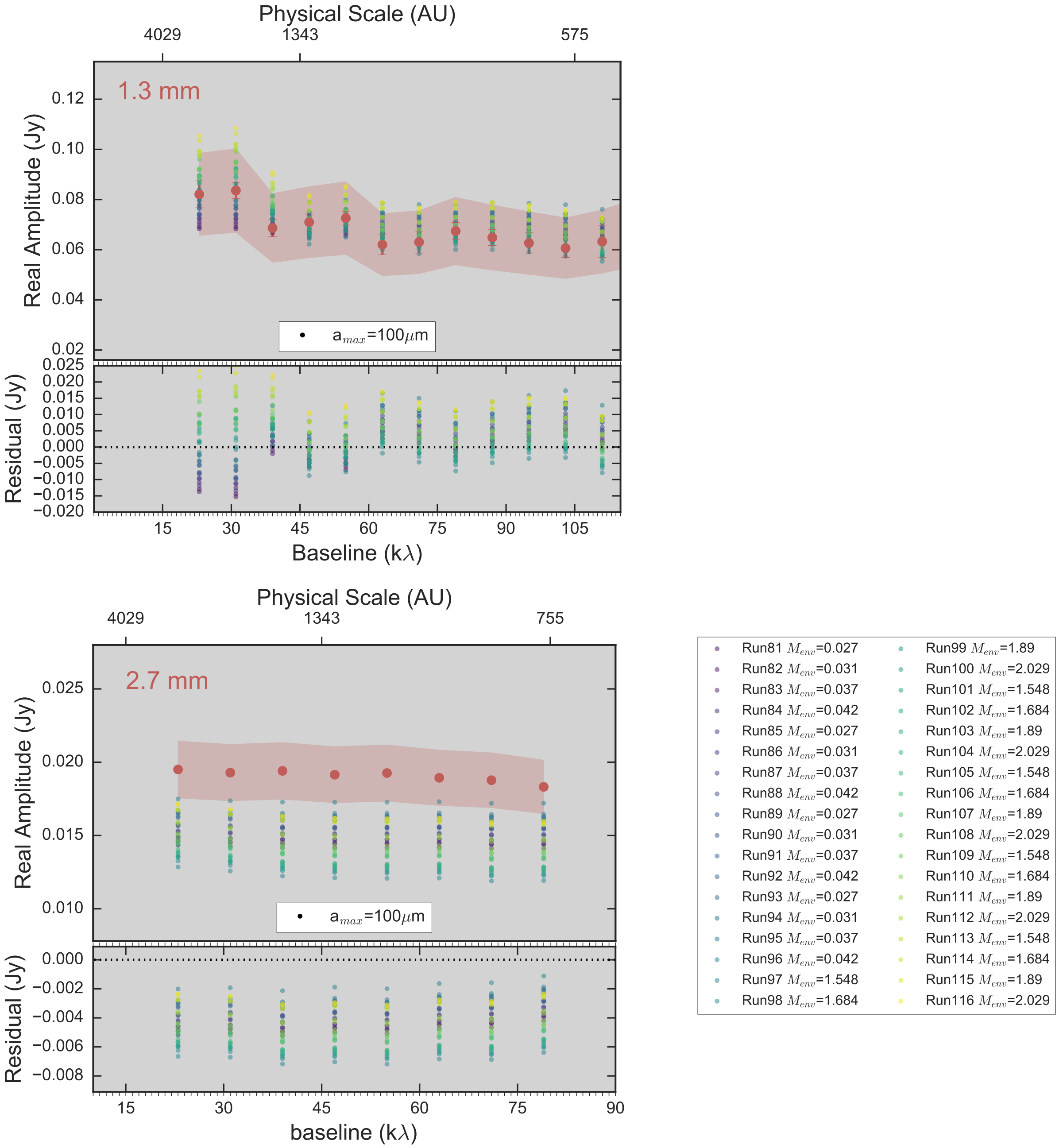

Figure B.4: Full radiative-transfer models for a_{max}=100μm. The name of the model and derived envelope mass are in the right panel. The color gradient represents the χ^2 from low (blue) to high values (yellow), that were used only as reference. After visual inspection, we chose the best models from the green area.

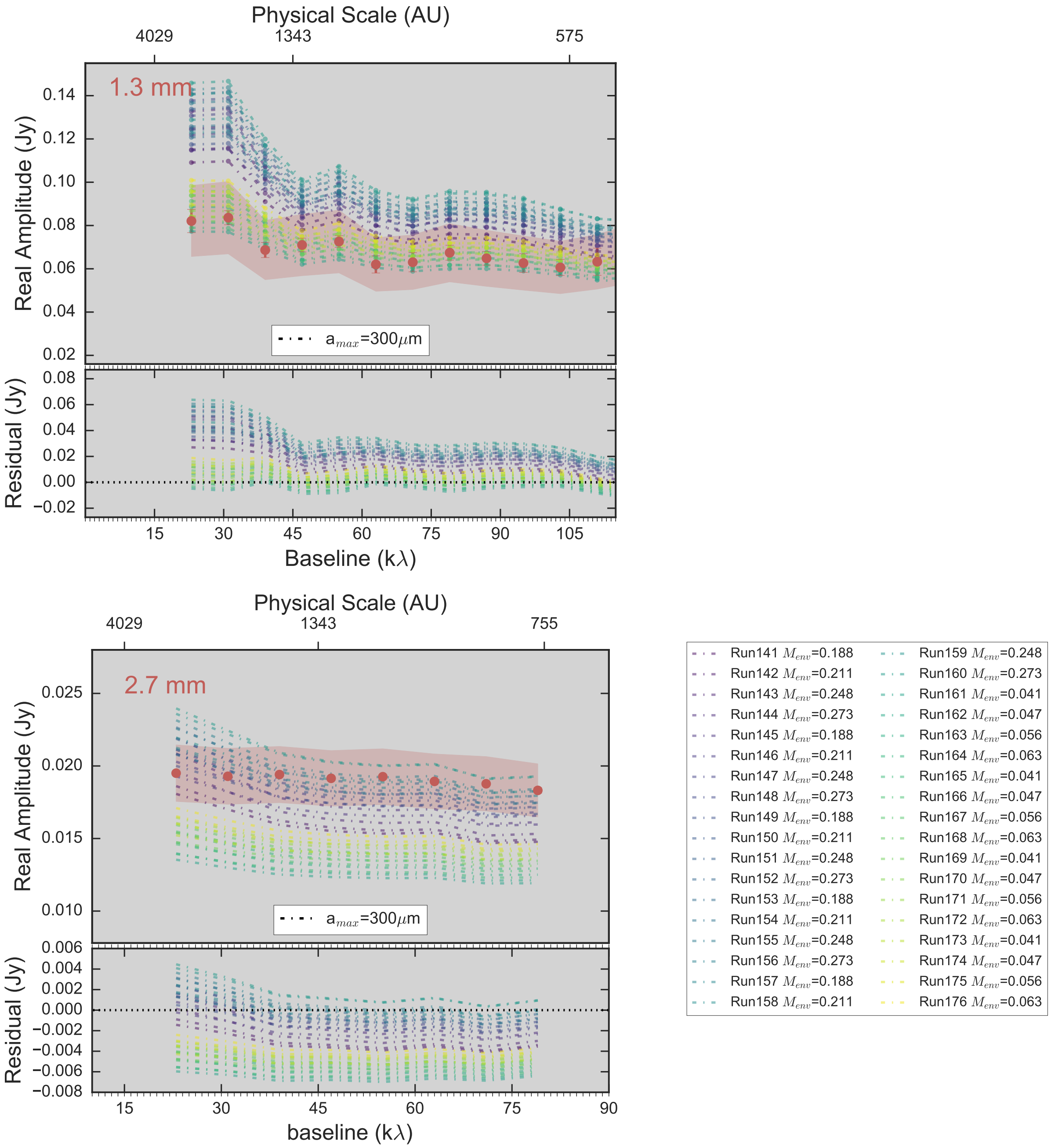

Figure B.5: Full radiative-transfer models for a_{max}=300μm. The name of the model and derived envelope mass are in the right panel. The color gradient represents the χ^2 from low (blue) to high values (yellow), that were used only as reference. After visual inspection, we chose the best models from the green area.

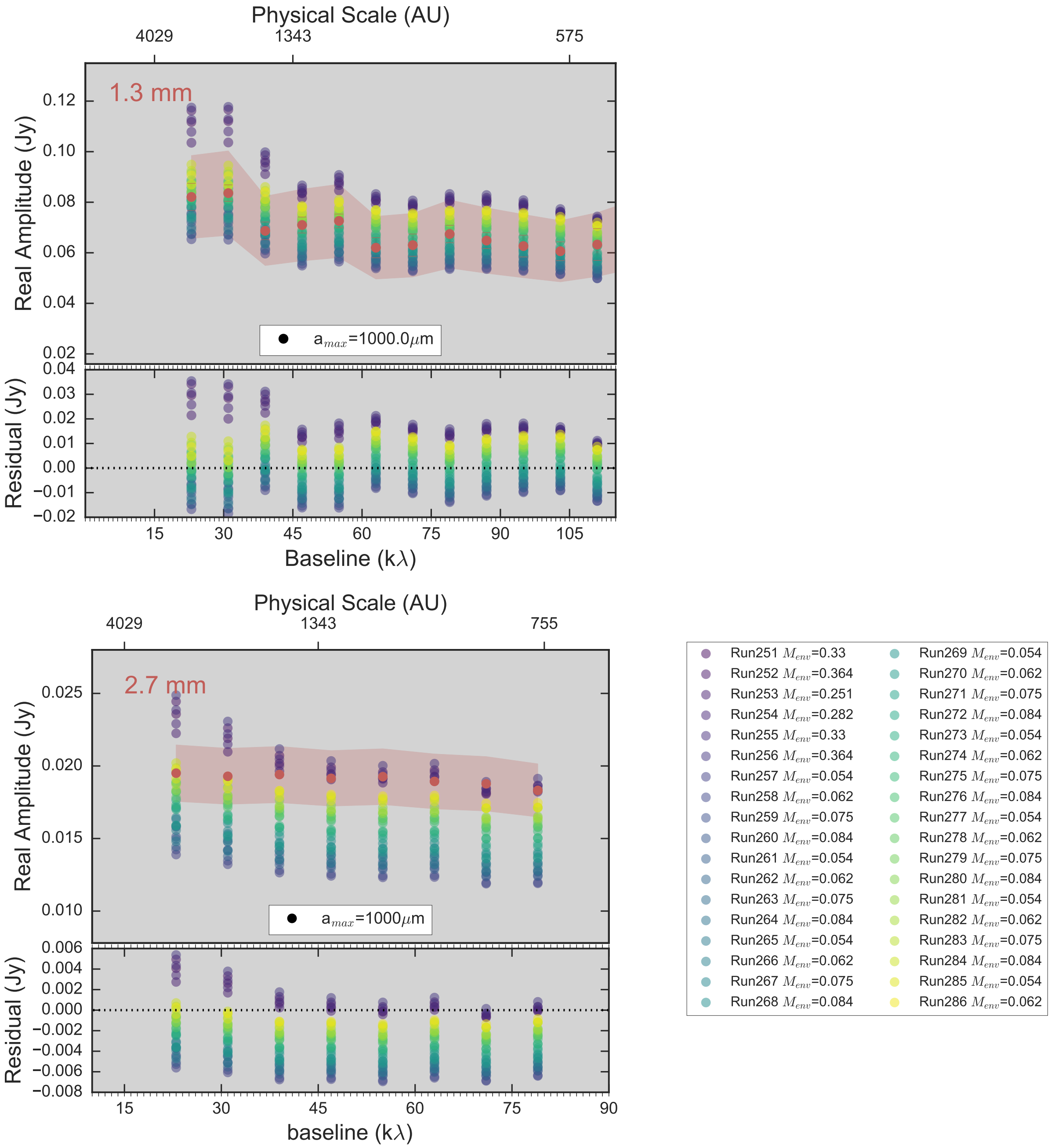

Figure B.6: Full radiative-transfer models for a_{max}=1000μm. The name of the model and derived envelope mass are in the right panel. The color gradient represents the χ^2 from low (blue) to high values (yellow), that were used only as reference. After visual inspection, we chose the best models from the green area.

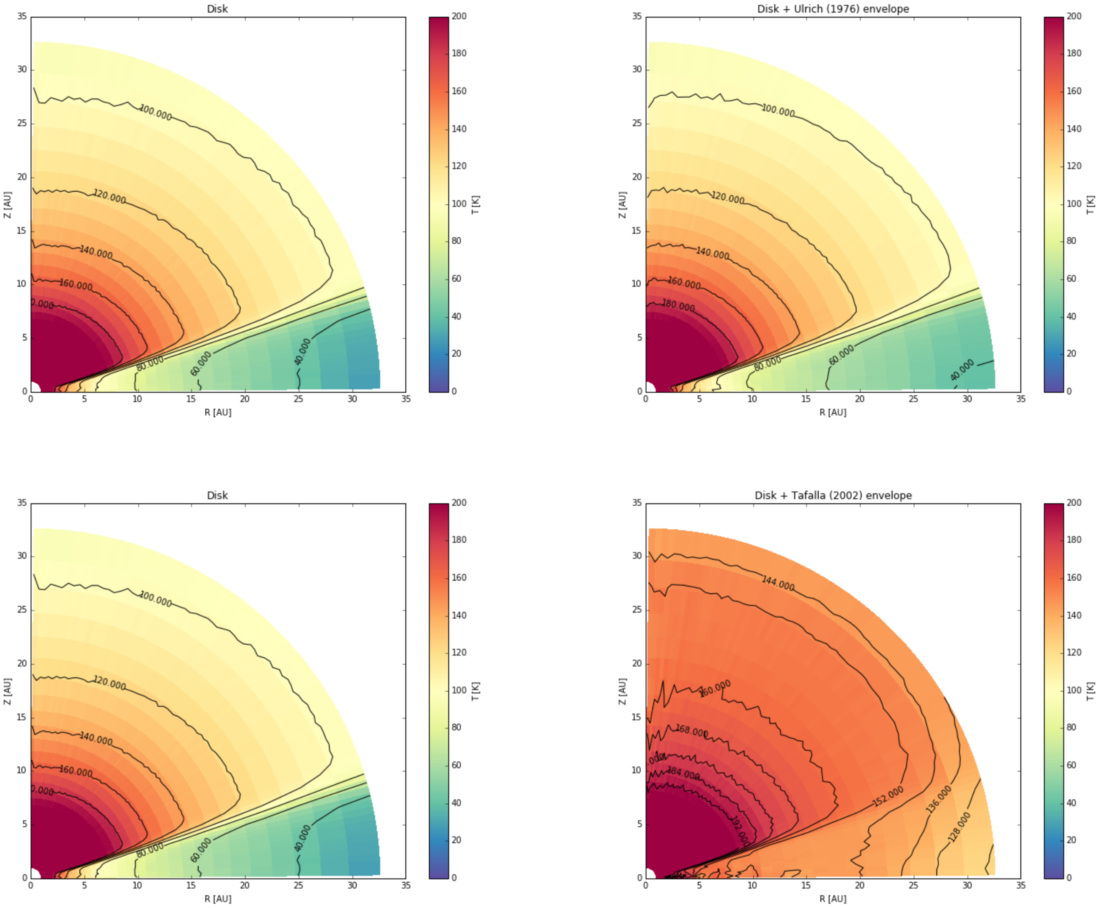

Figure B.7: Temperature structure in cylindrical coordinates of two cases: (top left panel) 25 AU disk with a_{max}^{disk}=1 cm and (top right panel) a 25 AU disk with a 1.3 $M_{\odot}$ Ulrich envelope structure and grain sizes with a_{max}^{env}=100 μm. (Bottom right panel) is the case of a 1.3 $M_{\odot}$ Tafalla et al. envelope profile with a_{max}^{env}=100 μm heating the 25 AU disk. 2D temperature contours are presented in black lines.

Appendix C

Chapter 3

C.1 New image size implementation

For this study we implemented a speed-up image time calculation by re-scaling the original image size suggested by GALARIO. The new image conserves the original image resolution (in terms of au/px), but it covers a new image size. The original image is stored in the center of the new image, while the extended image size is filled out with zero values.

In Figure C.1 we present three radiative transfer models at 8.12 mm. The grey line is a model with an image size of 11500 au and pixel scale of 13 au. The time cost of the ray-tracing is close to 300 s. To reduce the calculation time we decided to reduce the image size to 1000 and 2000 au, keeping the image resolution and filling the original image size of 11500 au with zeros. With this test it is possible to distinguish the effect of the image size in the visibilities (red and green dashed lines). The 2000 au image size is consistent with the larger image, while the 1000 au image starts to disagree with the grey line model after 500 kλ.

Table C.1 reports the values used to speed-up the fitting procedure on Per-emb-50. Please check your data-sets with GALARIO, using `get_image_size`, before to implementing this change.

Table C.1: Estimated raytracing cost and re-scaled image properties for recovering the resolution of Per-emb-50 data.

Wavelength [mm]	ext. image size [au]	image size [au]	n_{pix}	pixel scale [au]	t_{raytr} [s] [s]
1.29	42000	15000	1154	13	50
2.72	42000	15000	1154	13	50
8.12	11500	2000	358	5.6	30

Measured on machines equipped with Intel(R) Xeon(R) CPU E5-2660 v3 CPUs.

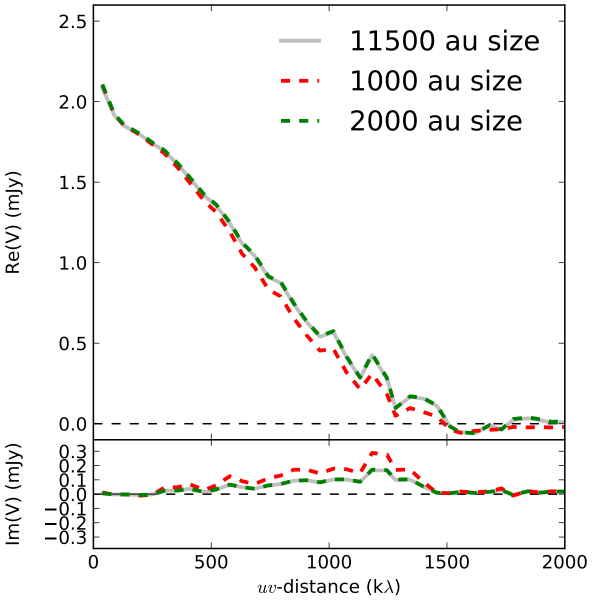

Figure C.1: Real and imaginary visibilities of the radiative transfer model at 8.12 mm. The gray line represents a model using an image size of 11500 au. The red and green dashed lines are models with image size of 1000 au and 2000 au, respectively, and an extended image size of 11500 au. The calculation cost for the image size of 2000 au is 10 times faster (30 s) than the image of 11500 au (300 s).

C.2 Data weights

The point source sensitivity[1] (in Jy) can be derived by:

$$\sigma = \frac{2\,k}{\eta_A A} \times \frac{< T_{sys} >}{\eta_C \eta_J \eta_P \sqrt{N(N-1)\Delta\nu\,\Delta t}} \times \frac{1}{\sqrt{N_P}}, \tag{C.1}$$

where, A is the collecting area in square meters (m^2) of a single antenna, η_A is the aperture efficiency, η_C is the correlator efficiency, η_J is the instrumental jitter, η_P is the atmospheric decorrelation, N_P are linear polarizations, T_{sys} is the system temperature in Kelvin (K), $\Delta\nu$ is the spectral bandwidth in Hz, and Δt is the integration time on-source in seconds. The continuum of the three data sets used in this analysis were produced by collapsing the line-free channels across all the spectral windows into a single continuum channel. The weight of a visibility is ideally $1/\sigma^2$, where σ is the error associated with each visibility and the error presented in the *uv*-distance vs. real amplitude figures. Since we are using three different data sets from different interferometers, we computed for each observation an average scaling factor to scale the weights. The scale factor provides new weights consistent with the real average dispersion in the measurements. Table C.2 presents the number of data weights visibilities N_w and the re-scaling factors f_{mm}.

Table C.2: Averaged weights and scale factors

$N_{1.29\,\mathrm{mm}}$	25810
$f_{1.29\,\mathrm{mm}}$	0.443569092259
$N_{2.72\,\mathrm{mm}}$	598500
$f_{2.72\,\mathrm{mm}}$	53699.5448394
$N_{8.12\,\mathrm{mm}}$	14839101
$f_{8.12\,\mathrm{mm}}$	54.0720825096

C.3 Two-step model best-fit parameters

The set of parameters that provided the best match with the observations is presented in Table C.3.

C.4 Testing model parameter limits

In order to complement and explain the grid of parameters, we created "border models". For each model we fixed each parameter to either the lower or upper value of Table 3.3,

---

[1] `http://www.iram.fr/IRAMFR/GILDAS/doc/pdf/noema-intro.pdf`

while the other five fit parameters are fixed to the best model values (see Table C.3). The domain for each parameter was chosen based on the previous studies of the source but also keeping a domain large enough to ensure adequate parameter space is covered in the grid search. In the following description of the figures we will explain the limits for each parameter.

Figure C.2 shows the radiative transfer models for 1.29, 2.72 and 8.12 mm data using a lower and upper limit for the disk dust mass of $5\times10^{-5}\,M_\odot$ and $0.005\,M_\odot$, respectively. With these mass limits we can see the variation in emission in the different wavelengths. A less massive disk translates in a lower emission in the visibilities (left panels), while a massive disk of total mass of $0.5\,M_\odot$ increases the emission in the vertical direction.

Figure C.3 shows the radiative transfer models for 1.29, 2.72 and 8.12 mm data using a lower and upper limit for the disk radius of 20 au and 100 au, respectively. We see that the emission follows a similar behaviour as in the disk mass case. A small size disk translates in a lower emission in the visibilities, while in the case of a larger disk the emission is greater than the data by a factor of 2. At 8.12 mm we can see that the model starts to show a sinusoidal shape. This is because the Fourier transform of a uniform disk with a sharp edge is given by a Bessel function and at the 8.12 mm physical scales the 100 au disk is resolved.

Figure C.4 shows the radiative transfer models for 1.29, 2.72 and 8.12 mm data using a lower and upper limit for the maximum grain size in the disk of $100\,\mu$m and $10000\,\mu$m, respectively. Since the disk is optically thick, the change of grain size is undetected at 1.29 mm but is slightly different at 2.72 mm. We start to see the effect of sizes at longer wavelengths, while small grains show lower disk emission (left bottom panel), centimeter grain sizes increase the disk emission at short u-distances by $\sim 20\,\%$.

Figure C.5 shows the radiative transfer models for 1.29, 2.72 and 8.12 mm data using a lower and upper limit for the envelope central density $1\times 10^{-17}\,\mathrm{g\,cm^{-3}}$ and $1\times 10^{-19}\,\mathrm{g\,cm^{-3}}$, respectively. In the case of lower inner densities the contribution in the visibilities is almost zero, therefore, the emission is dominated only by the disk. In the case of high central densities (right panels) the inner regions of the envelope are extremely dense and therefore effect the emission in the visibilities.

Figure C.6 shows the radiative transfer models for 1.29, 2.72 and 8.12 mm data using a lower and upper limit for the envelope rotational radius of 38 au and 519 au, respectively. In the case of a small rotational radius (left panels) the overall emission is dominated by the disk emission, while in the case of a large rotational radius, the envelope contribution appears at 1.29 and 2.72 mm where the inner envelope regions are covered. At 8.12 mm the 519 au rotational radius is not affecting the overall emission.

Figure C.7 shows the radiative transfer models for 1.29, 2.72 and 8.12 mm data using

Table C.3: Best radiative-transfer model

Parameter	Description	Status	Values
Radiation source			
$M_\star$ ($M_\odot$)	Stellar mass	Fixed	2.9
$R_\star$ (au)	Radius of the star	Fixed	0.025
$T_\star$ (K)	Effective temperature	Fixed	5,011
Opacity properties			
$g_{\rm dens}$ (g cm^{-3})	Grain material bulk density	Fixed	1.36
$g_{\rm powex}$	Power law index of grain size distribution	Fixed	3.5
$a_{\rm min}$ (μm)	Minimum grain size (disk, envelope)	Fixed	0.1
Disk parameters			
$M_{\rm disk}$ ($M_\odot$)	Disk mass	Varied	1.47×10^{-3}
$\Sigma_{\rm disk}$ (g cm^{-2})	Disk dust surface density	Varied	1.43
ϕ	Flaring index	Fixed	1.14
H_p/r (au)	Reference radius	Fixed	25
$H_{\rm r,disk}$	Ratio of the pressure scale height over the reference radius	Fixed	0.1
p	Power exponent of the surface density distribution	Varied	-1.5
$r_{\rm disk}$ (au)	Disk outer radius	Varied	38
$r_{\rm in}$ (au)	Disk inner radius	Fixed	1.0
$a_{\rm max}^{\rm disk}$(μm)	Disk maximum grain size	Varied	735
Envelope parameters			
	Cavity mode	Fixed	Grid center
$R_{\rm out}$ (au)	Envelope diameter	Fixed	8 800
ρ_0 (g cm^{-3})	Central density	Varied	2.5×10^{-19}
$M_{\rm env}$ ($M_\odot$)	Envelope dust mass	Varied	7.35×10^{-4}
$R_{\rm rot}$ (au)	Rotational radius	Varied	113
$r_{\rm trun}$ (au)	Truncation radius	Fixed	$r_{\rm disk}$
θ (°)	Opening angle of the cavity	Fixed	30.0
$a_{\rm max}^{\rm env}$(μm)	Envelope maximum grain size	Varied	26

Table C.4: Full radiative-transfer best fit model from Agurto-Gangas et al. (2019)

Description	Parameter	Best-Model 2
Disk		
Total mass	$M_{\rm disk}$ (M$_\odot$)	0.24
Surface density	$\Sigma_{\rm disk}$ (g cm^{-2})	364.2
Outer radius	$r_{\rm out}$ (au)	27
Max. grain size	$a_{\rm max}^{\rm disk}(\mu$m)	10 000
Tafalla envelope profile		
Power law profile	p	-1.1
Central density	ρ_0 (g cm^{-3})	1.5×10^{-16}
Total mass	$M_{\rm env}$ (M$_\odot$)	1.54
Truncation radius	$r_{\rm trun}$ (au)	27
Flattening radius	r_0 (au)	27
Max. grain size	$a_{\rm max}^{\rm env}(\mu$m)	100

a lower and upper limit for the maximum grain size in the envelope of 5 μm and 200 μm, respectively. Contrary to the case of grain sizes in the disk at 1.29 and 2.72 mm, the envelope grain size is affecting emission in those wavelengths. Increasing the grain size in the envelope increases the envelope emission in all wavelengths. This test limits also confirms that the dust size in the envelope is mostly dominated by small grains on the order of μm-sizes.

Border models: disk mass

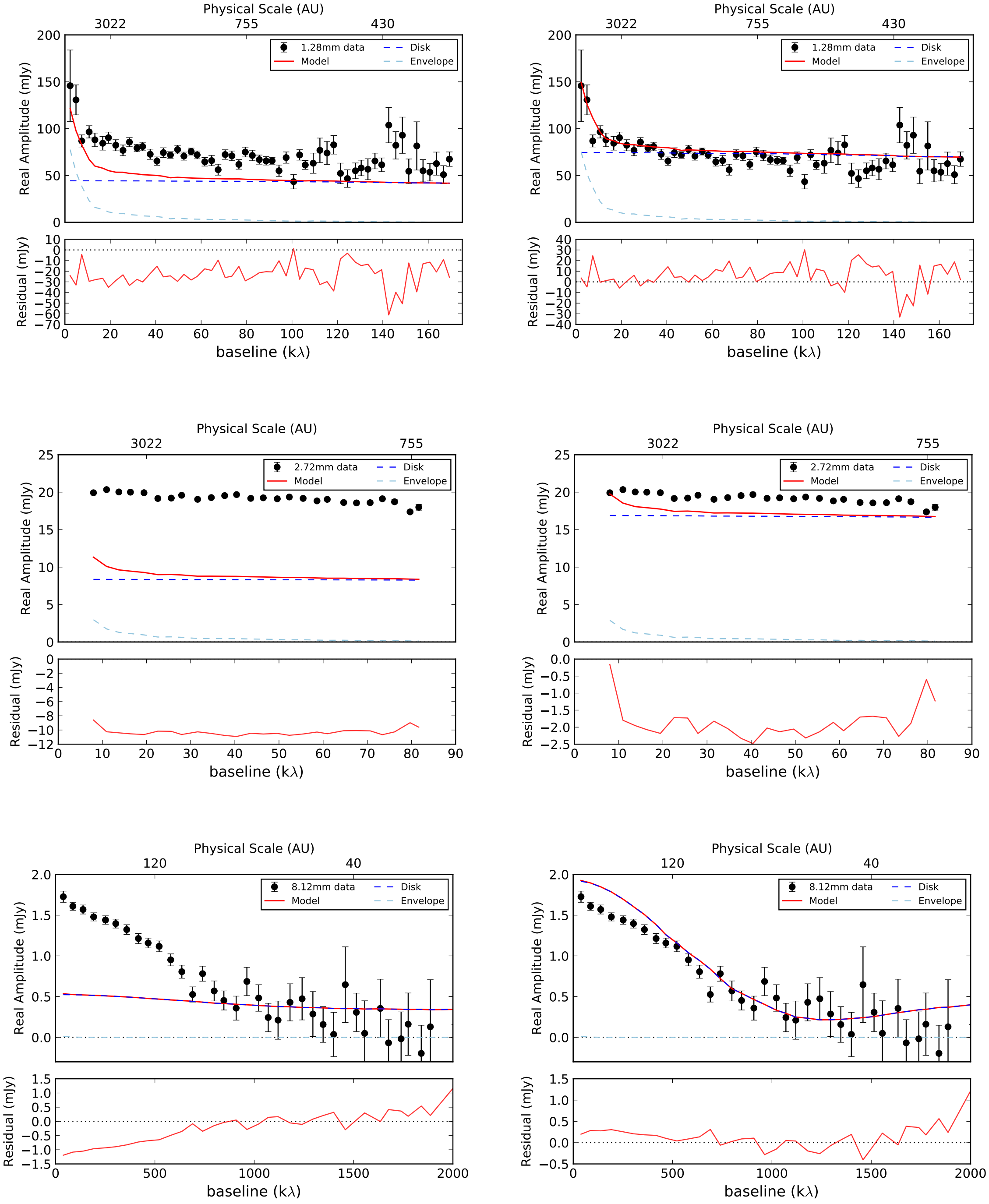

Figure C.2: Real and imaginary visibilities with the radiative transfer model using lower and upper limits for the dust disk mass. From top to bottom we show the 1.29, 2.72 and 8.12 mm data. In the upper panel we used a dust disk mass of $1\times 10^{-5}\,M_\odot$ while in the bottom panels we used an upper limit of $1\times 10^{-2}\,M_\odot$. $R_{\rm disk}$, $\rho_0^{\rm env}$, $R_{\rm rot}$, $a_{\rm max}^{\rm disk}$ and $a_{\rm max}^{\rm env}$ are fixed to the best model values of Table C.3. For each wavelength we show: disk contribution in blue dashed line, envelope contribution in dashed light blue, and in red line the total model (disk+envelope). The bottom of each panel shows the residual between the data and the model.

C.5 Testing envelope minimum grain size

Here is modified the a_{min} value of the envelope dust distribution of the best model, see Table C.3 and C.8. The change of a_{min} from $0.1\,\mu$m to $20\,\mu$m, keeping a value of a_{max} of $26\,\mu$m. With increasing a_{min} the visibilities deviate more and more from the observed data. At 2.72 mm this effect is more notorious and it may indicates that the envelope is dominated by small μm-sizes grains.

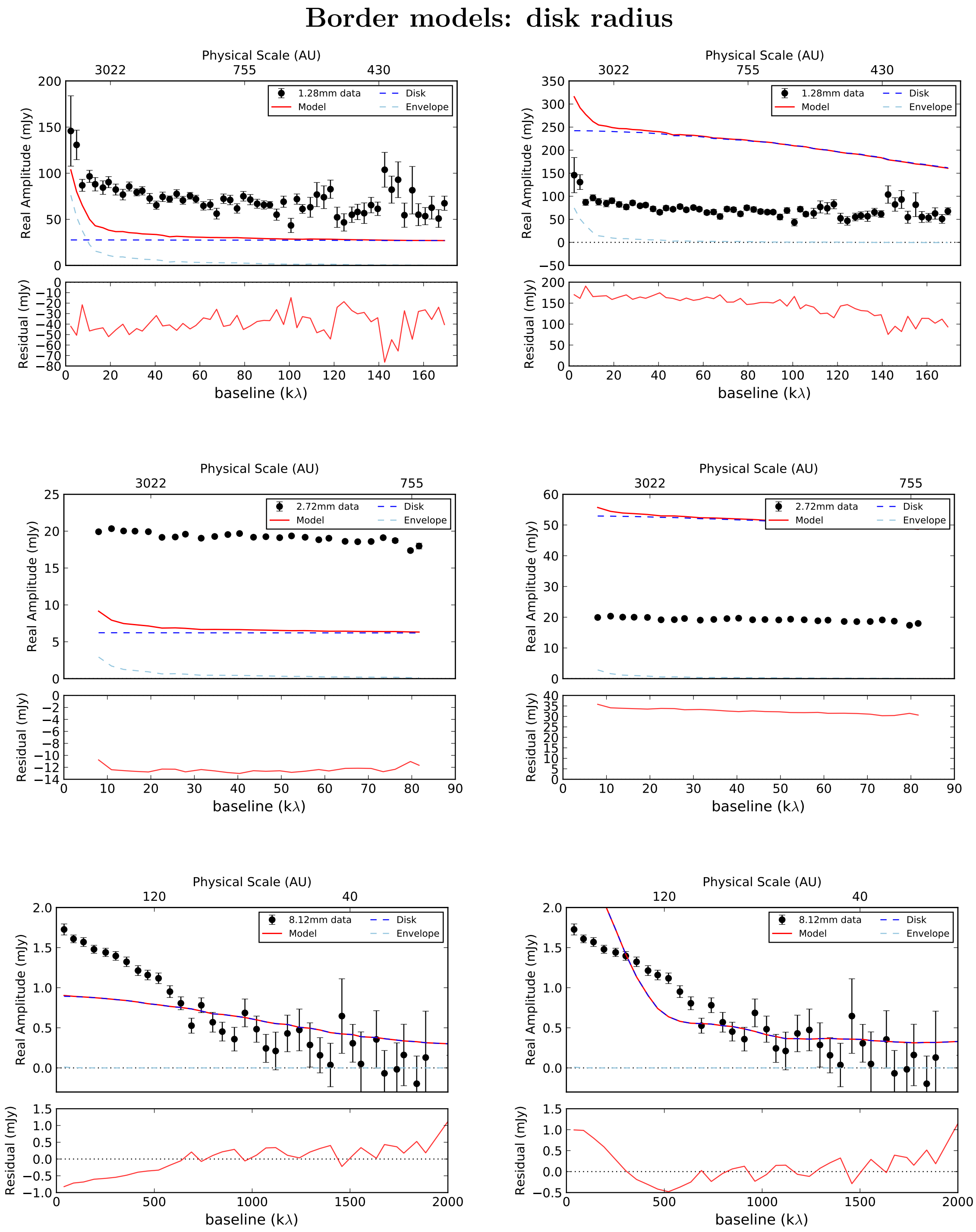

Figure C.3: Real and imaginary visibilities with the radiative transfer model using lower and upper limits for the disk radius. From top to bottom we show the 1.29, 2.72 and 8.12 mm data. In the upper panel we used a disk radius of 10 au while in the bottom panels we used an upper limit of 100 au. $M_{\rm disk}$, $\rho_0^{\rm env}$, $R_{\rm rot}$, $a_{\rm max}^{\rm disk}$ and $a_{\rm max}^{\rm env}$ are fixed to the best model values of Table C.3. For each wavelength we show: disk contribution in blue dashed line, envelope contribution in dashed light blue, and in red line the total model (disk+envelope). The bottom of each panel shows the residual between the data and the model.

Border models: disk maximum grain size

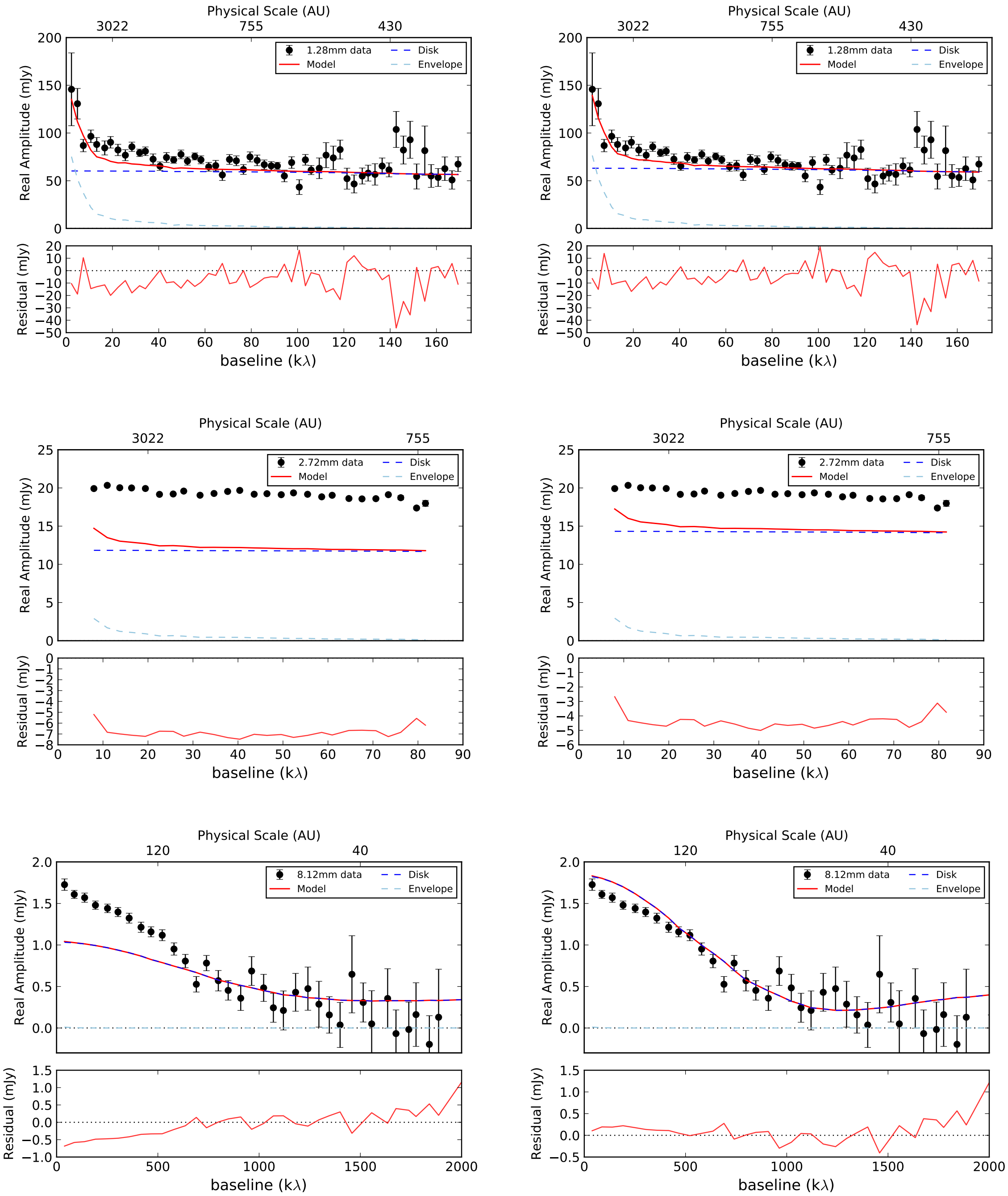

Figure C.4: Real and imaginary visibilities with the radiative transfer model using lower and upper limits for the maximum grain size of the disk. From top to bottom we show the 1.29, 2.72 and 8.12 mm data. In the upper panel we used a disk a_{max} of 1×10^{-4} cm while in the bottom panels we used an upper limit of 1 cm. $M_{\rm disk}$, $R_{\rm disk}$, $\rho_0^{\rm env}$, $R_{\rm rot}$ and $a_{\rm max}^{\rm env}$ are fixed to the best model values of Table C.3. For each wavelength we show: disk contribution in blue dashed line, envelope contribution in dashed light blue, and in red line the total model (disk+envelope).The bottom of each panel shows the residual between the data and the model.

Border models: envelope central density

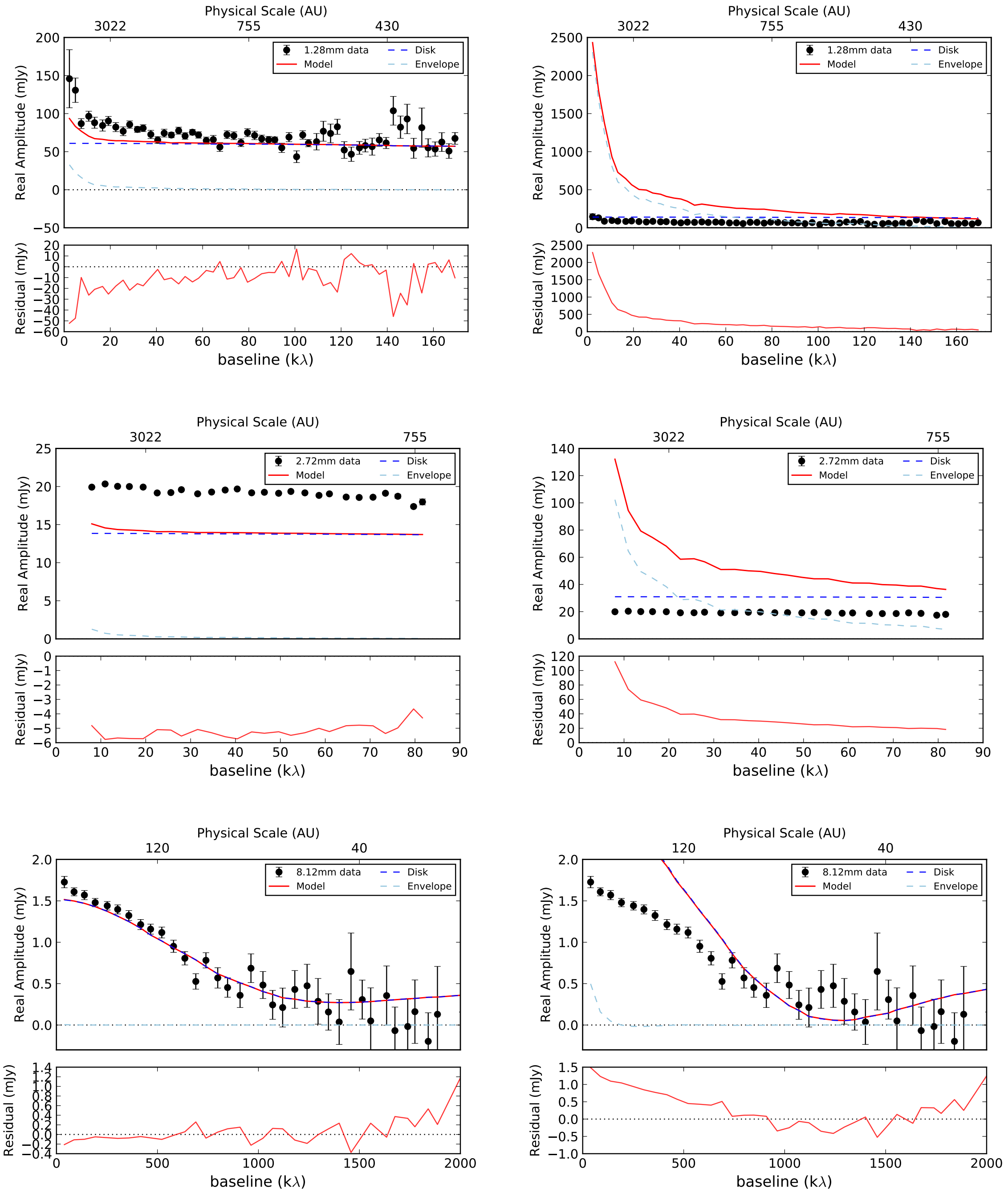

Figure C.5: Real and imaginary visibilities with the radiative transfer model using lower and upper limits for the central envelope density. From top to bottom we show the 1.29, 2.72 and 8.12 mm data. In the left panel we used a central density of $1\times 10^{-19}\,\mathrm{g\,cm^{-3}}$ while in the right panels we used an upper limit of $1\times 10^{-17}\,\mathrm{g\,cm^{-3}}$. $M_{\rm disk}$, $R_{\rm disk}$, $R_{\rm rot}$, $a^{\rm disk}_{\rm max}$ and $a^{\rm env}_{\rm max}$ are fixed to the best model parameters of Table C.3. For each wavelength we show: disk contribution in blue dashed line, envelope contribution in dashed light blue, and in red line the total model (disk+envelope).The bottom of each panel shows the residual between the data and the model.

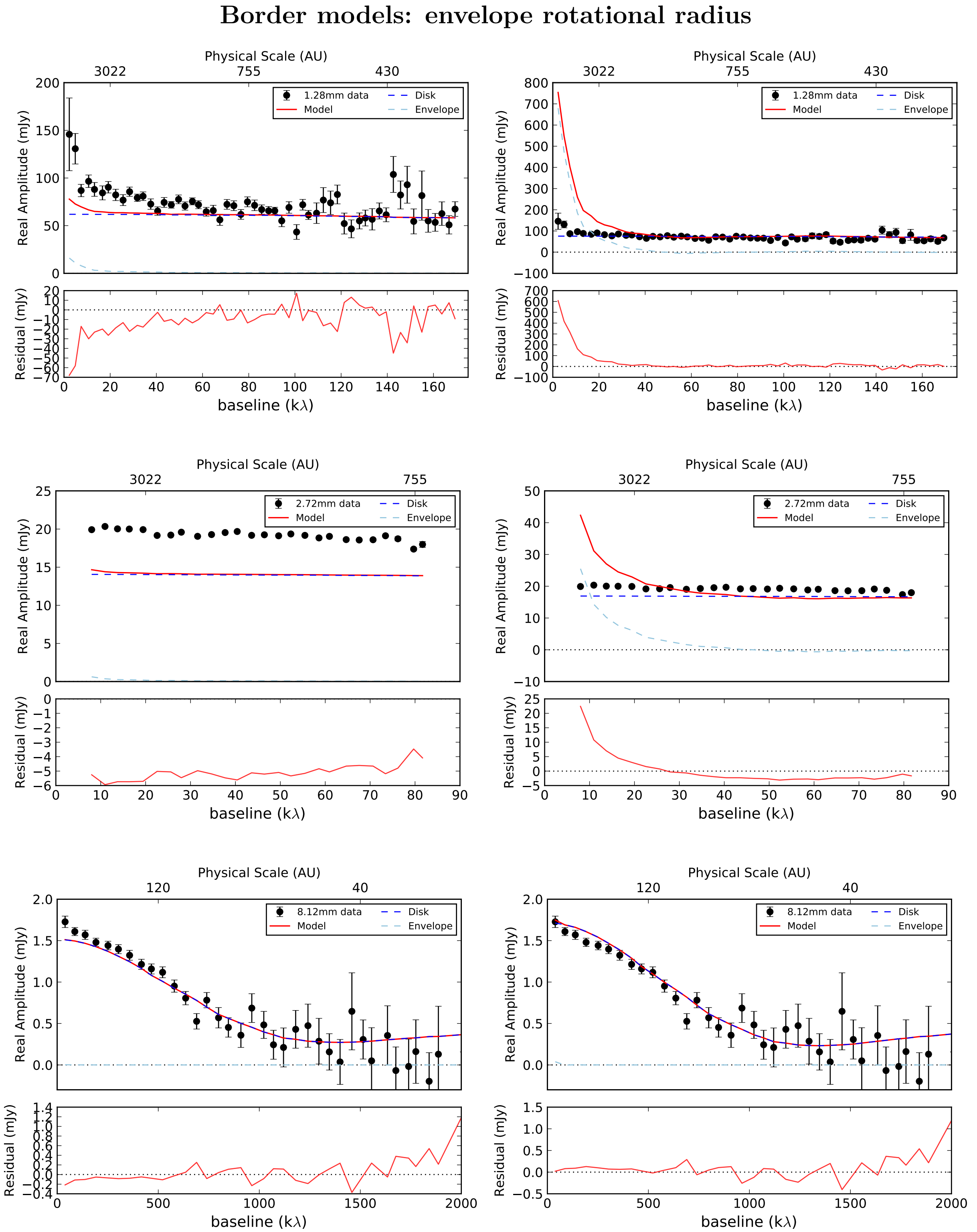

Figure C.6: Real and imaginary visibilities with the radiative transfer model using lower and upper limits for the envelope rotational radius. From top to bottom we show the 1.29, 2.72 and 8.12 mm data. In the upper panel we used a rotational radius of 38 au while in the bottom panels we used an upper limit of 519 au. $M_{\rm disk}$, $R_{\rm disk}$, $\rho_0^{\rm env}$, $a_{\rm max}^{\rm disk}$ and $a_{\rm max}^{\rm env}$ are fixed to the best model values of Table C.3. For each wavelength we show: disk contribution in blue dashed line, envelope contribution in dashed light blue, and in red line the total model (disk+envelope). The bottom of each panel shows the residual between the data and the model.

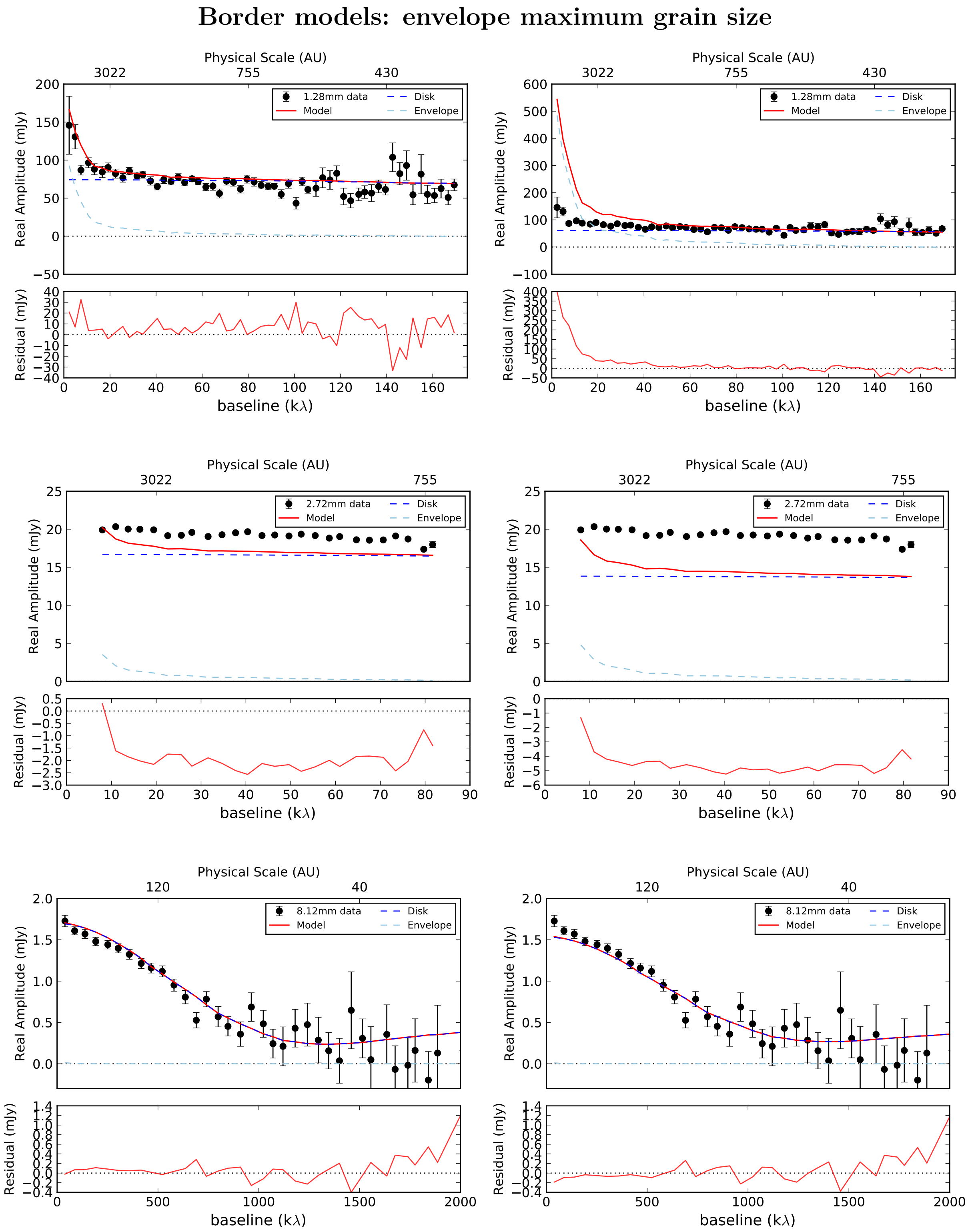

Border models: envelope maximum grain size

Figure C.7: Real and imaginary visibilities with the radiative transfer model using lower and upper limits for the maximum grain size of the envelope. From top to bottom we show the 1.29, 2.72 and 8.12 mm data. In the left panels we used an envelope a_{max} of 5 μm while in the right panels we used an upper limit of 200 μm. $M_{\rm disk}$, $R_{\rm disk}$, $\rho_0^{\rm env}$, $R_{\rm rot}$ and $a_{\rm max}^{\rm disk}$ are fixed to the best model values of Table C.3. For each wavelength we show: disk contribution in blue dashed line, envelope contribution in dashed light blue, and in red line the total model (disk+envelope). The bottom of each panel shows the residual between the data and the model.

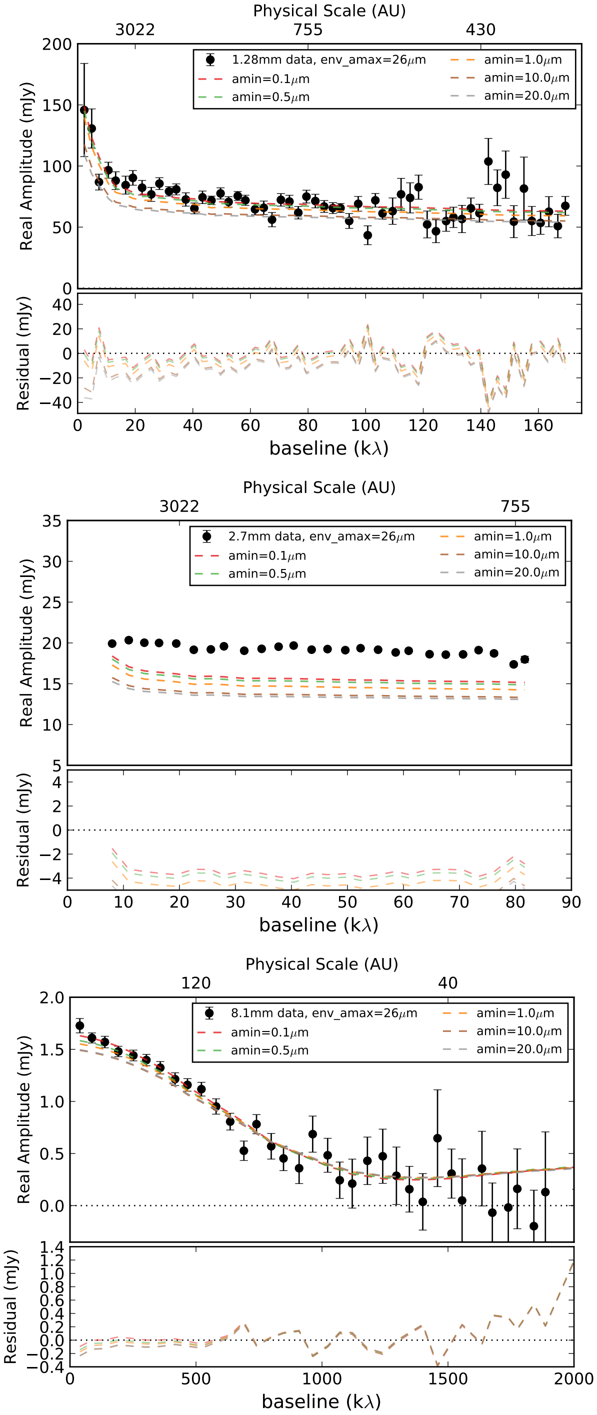

Figure C.8: Real visibilities vs baselines at 1.29 mm, 2.72 mm and 8.12 mm. Colored dashed lines represent the synthetic visibilities of different radiative transfer models with $a_{\rm min}$=0.1–20 μm and $a_{\rm max}$=25 μm. The bottom of each panel shows the residuals between the data and the models.

Appendix D

Chapter 4

D.1 Example input file

To setup a model is necessary to write an input file in radmc3dPy format (.inp).

```
#####################################################
# RADMC-3D PARAMETER SETUP
# Created by the python module of RADMC-3D
#####################################################
# ---------------------------------------------------
# Block: Radiation sources
# ---------------------------------------------------
iext                       = False  # Include external radiation?
mstar                      = [2.25*ms]  # Mass of the star(s)
pstar                      = [0.0, 0.0, 0.0]  # Position of the star(s) (cartesian coordinates)
rstar                      = [5.6*rs]  # Radius of the star(s)
tstar                      = [3336.0]  # Effective temperature of the star(s) [K]
# ---------------------------------------------------
# Block: Grid parameters
# ---------------------------------------------------
crd_sys                    = 'sph'  # Coordinate system used (car/cyl)
nw                         = [50, 150, 100]  # Number of points in the wavelength grid
nx                         = [50,50]  # Number of grid points in the first dimension
ny                         = 60  # Number of grid points in the second dimension
nz                         = 0  # Number of grid points in the third dimension
wbound                     = [0.1, 7.0, 25.0, 1e4]  # Boundaries for the wavelength grid
xbound                     = [1.0*au,80.*au,1450.*au]  # Boundaries for the x grid
ybound                     = [0.,pi/2.]  # Boundaries for the y grid
zbound                     = [0., 2.0*pi]  # Boundaries for the z grid
```

```
# --------------------------------------------------
# Block: Dust opacity
# --------------------------------------------------
gdens                     = 1.36  # Grain material bulk density
gsdist_powex              = [-3.5,-3.5]  # Power law index of grain size distribution
gsmax                     = [800.*1.0e-4, 400.*1.0e-4]  # Maximum grain size [disk, envelope]
gsmin                     = [0.1*1.0e-4, 0.1*1.0e-4]  # Minimum grain size [disk, envelope]
lnk_fname                 = 'mix_compact_bruggeman.lnk'  # Optical constant (n,k) input file name
ngpop                     = 2  # Number of grain populations
ngs                       = 60  # Number of grain size bins between gsmin and gsmax

# ---------------------------------------------------
# Block: Code parameters
# ---------------------------------------------------
istar_sphere              = 1  # 1 - take into account the finite
                               #size of the star, 0 - take the star to be point-like
itempdecoup               = 1  # Enable for different dust components to
                               # have different temperatures
lines_mode                = -1  # Line raytracing mode
modified_random_walk      = 1  # Use the modified random walk method to improve speed?
nphot                     = 5e5  # Nr of photons for the thermal Monte Carlo
nphot_scat                = 1e5  # Nr of photons for the scattering Monte Carlo (for images)
nphot_spec                = 1e5  # Nr of photons for the scattering Monte Carlo (for spectra)
rto_style                 = 1  # Format of output files (1-ascii, 2-unformatted f77, 3-binary
scattering_mode_max       = 0  # 0 - no scattering, 1 - isotropic scattering,
                               # 2 - anisotropic scattering
tgas_eq_tdust             = 1  # Take the dust temperature to identical
                               # to the gas temperature
# ----------------------------------------------------
# Block: Model disk and envelope
# ----------------------------------------------------
bgdens                    = 0.0  # Background density (g/cm^3)
dusttogas                 = 0.01  # Dust-to-gas mass ratio
hrdisk                    = 0.1  # Ratio of the pressure scale height over radius at hrpivot
hrpivot                   = 50.0*au  # Reference radius at which Hp/R is taken
mdisk                     = 8.e-4*ms  # Mass of the disk !!! should be 0.1*ms
modeCav                   = 'gridcenter'  #
modeEnv                   = 'Ulrich1976'  #
model_dir                 = '.'  # model folder path
plh                       = 0.14  # Flaring index
plsig1                    = -1.0  # Power exponent of the surface density distribution
                                  #as a function of radius
```

```
plsig2                     = -12.0  # Power law exponent at r > rdisk
                                    # (abrubt cutoff at rdisk is not realistic)
prhoEnv                    = -1.5  # Power exponent of the radial density distribution
r0Env                      = 400.0*au  # Within this radius the density profile is flat
rTrunEnv                   = 300.*au  # Truncation radius
rdisk                      = 90.*au  # Outer radius of the disk
redFactCav                 = 0.0  #
redFactEnv                 = 0.0  #
rho0Env                    = 1.5e-19  # New central density gr/cm3 dust density volume
rin                        = 1.0*au  # Inner radius of the disk
thetac_deg                 = 25  # Opening angle of the cavity
# -----------------------------------------------------
# Block: Slab parameters
# -----------------------------------------------------
h0_slab                    = 10.0*au          # Slab inner height [cm]
h1_slab                    = 100.0*au         # Slab outer height [cm]
r0_slab                    = 30.0*au          # Slab inner radius [cm]
r1_slab                    = 1000.0*au        # Slab outer radius [cm]
sig0_slab                  = 1.0e-4           # Sigma0 [gram/cm**2]
m_slab                     = 0.01*ms          # Slab mass [gram]
# -----------------------------------------------------
# Block: contributions
# -----------------------------------------------------
slab                       = False # Include slab in model?
icav                       = True  # Include envelope cavity in model?
ienv                       = True  # Include envelope in model?
idisk                      = True  # Include disk in model?
```

Bibliography

Ábrahám, P., Juhász, A., Dullemond, C. P., et al. 2009, , 459, 224

Adams, F. C., Emerson, J. P., & Fuller, G. A. 1990, , 357, 606

Adams, F. C., Lada, C. J., & Shu, F. H. 1987, , 312, 788

Agurto-Gangas, C., Pineda, J. E., Szucs, L., et al. 2019, arXiv e-prints, arXiv:1901.05021

Agurto-Gangas, C. & Szucs, L. 2020, Simple Disk Envelope fit (SiDE)

Alves, F. O., Caselli, P., Girart, J. M., et al. 2019, Science, 366, 90

Alves, F. O., Girart, J. M., Caselli, P., et al. 2017, , 603, L3

Alves, F. O., Girart, J. M., Padovani, M., et al. 2018, , 616, A56

Andersen, B. C., Stephens, I. W., Dunham, M. M., et al. 2019, The Astrophysical Journal, 873, 54

André, P. & Montmerle, T. 1994, , 420, 837

André, P., Ward-Thompson, D., & Barsony, M. 1993, , 406, 122

Andrews, S. M. & Williams, J. P. 2007, , 671, 1800

Artur de la Villarmois, E., Jørgensen, J. K., Kristensen, L. E., et al. 2019, arXiv e-prints, arXiv:1904.13161

Banzatti, A., Testi, L., Isella, A., et al. 2011, , 525, A12

Beckwith, S. V. W. & Sargent, A. I. 1991, , 381, 250

Beckwith, S. V. W., Sargent, A. I., Chini, R. S., & Guesten, R. 1990, , 99, 924

Birnstiel, T., Ricci, L., Trotta, F., et al. 2010, , 516, L14

Black, J. H. 1994, in Astronomical Society of the Pacific Conference Series, Vol. 58, The First Symposium on the Infrared Cirrus and Diffuse Interstellar Clouds, ed. R. M. Cutri & W. B. Latter, 355

Bohren, C. F. & Huffman, D. R. 1983, Absorption and scattering of light by small particles

Boulanger, F., Abergel, A., Bernard, J. P., et al. 1996, , 312, 256

Brooke, T. Y., Huard, T. L., Bourke, T. L., et al. 2007, , 655, 364

Bruggeman, D. A. G. 1935, Annalen der Physik, 416, 636

Butner, H. M., Natta, A., & Evans, II, N. J. 1994, , 420, 326

Carrasco-González, C., Henning, T., Chandler, C. J., et al. 2016, , 821, L16

Chacón-Tanarro, A., Caselli, P., Bizzocchi, L., et al. 2017, , 606, A142

Chacón-Tanarro, A., Pineda, J. E., Caselli, P., et al. 2019, , 623, A118

Chiang, E. & Youdin, A. N. 2010, Annual Review of Earth and Planetary Sciences, 38, 493

Chiang, H.-F., Looney, L. W., & Tobin, J. J. 2012a, , 756, 168

Chiang, H.-F., Looney, L. W., & Tobin, J. J. 2012b, , 756, 168

Cortes, S. R., Meyer, M. R., Carpenter, J. M., et al. 2009, , 697, 1305

Crapsi, A., van Dishoeck, E. F., Hogerheijde, M. R., Pontoppidan, K. M., & Dullemond, C. P. 2008, , 486, 245

D'Alessio, P., Calvet, N., & Hartmann, L. 2001, , 553, 321

D'Alessio, P., Calvet, N., Hartmann, L., Franco-Hernández, R., & Servín, H. 2006, , 638, 314

Draine, B. T. 1978, , 36, 595

Draine, B. T. 2003, , 41, 241

Draine, B. T. 2006, , 636, 1114

Dullemond, C. P., Dominik, C., & Natta, A. 2001, , 560, 957

Dullemond, C. P., Juhasz, A., Pohl, A., et al. 2012, RADMC-3D: A multi-purpose radiative transfer tool, Astrophysics Source Code Library

Dunham, M. M., Vorobyov, E. I., & Arce, H. G. 2014, , 444, 887

Dzib, S. A., Loinard, L., Ortiz-León, G. N., Rodríguez, L. F., & Galli, P. A. B. 2018, , 867, 151

Eisner, J. A. 2012, , 755, 23

Enoch, M. L., Evans, II, N. J., Sargent, A. I., & Glenn, J. 2009, , 692, 973

Enoch, M. L., Young, K. E., Glenn, J., et al. 2006, , 638, 293

Evans, M. G., Ilee, J. D., Boley, A. C., et al. 2015, , 453, 1147

Evans, II, N. J., Allen, L. E., Blake, G. A., et al. 2003, , 115, 965

Foreman-Mackey, D. 2016, The Journal of Open Source Software, 24

Foreman-Mackey, D., Hogg, D. W., Lang, D., & Goodman, J. 2013a, , 125, 306

Foreman-Mackey, D., Hogg, D. W., Lang, D., & Goodman, J. 2013b, , 125, 306

Furlan, E., Hartmann, L., Calvet, N., et al. 2006, , 165, 568

Galametz, M., Maury, A. J., Valdivia, V., et al. 2019, arXiv e-prints, arXiv:1910.04652

Goodman, J. & Pindor, B. 2000, , 148, 537

Goodman, J. & Weare, J. 2010, Communications in Applied Mathematics and Computational Science, Vol. 5, No. 1, p. 65-80, 2010, 5, 65

Greene, T. P., Wilking, B. A., Andre, P., Young, E. T., & Lada, C. J. 1994, , 434, 614

Guilloteau, S. & Lucas, R. 2000, in Astronomical Society of the Pacific Conference Series, Vol. 217, Imaging at Radio through Submillimeter Wavelengths, ed. J. G. Mangum & S. J. E. Radford, 299

Hara, C., Shimajiri, Y., Tsukagoshi, T., et al. 2013, , 771, 128

Hartmann, L., Herczeg, G., & Calvet, N. 2016, , 54, 135

Heim, L.-O., Blum, J., Preuss, M., & Butt, H.-J. 1999, Phys. Rev. Lett., 83, 3328

Heng, K. & Kenyon, S. J. 2010, , 408, 1476

Hewish, A., Bell, S. J., Pilkington, J. D. H., Scott, P. F., & Collins, R. A. 1968, , 217, 709

Hildebrand, R. H. 1983, , 24, 267

Hirota, T., Bushimata, T., Choi, Y. K., et al. 2008, , 60, 37

Högbom, J. A. 1974, , 15, 417

Hull, C. L. H., Yang, H., Li, Z.-Y., et al. 2018, , 860, 82

I-Hsiu Li, J., Liu, H. B., Hasegawa, Y., & Hirano, N. 2017, ArXiv e-prints [[arXiv]1704.06246]

Isella, A., Benisty, M., Teague, R., et al. 2019, , 879, L25

Jeans, J. H. 1902, Philosophical Transactions of the Royal Society of London Series A, 199, 1

Jones, A. P., Fanciullo, L., Köhler, M., et al. 2013, , 558, A62

Jones, A. P., Koehler, M., Ysard, N., et al. 2016, 1

Jørgensen, J. K., Bourke, T. L., Myers, P. C., et al. 2007, , 659, 479

Juhász, A., Dullemond, C. P., van Boekel, R., et al. 2012, , 744, 118

Kataoka, A., Muto, T., Momose, M., Tsukagoshi, T., & Dullemond, C. P. 2016, , 820, 54

Kataoka, A., Muto, T., Momose, M., et al. 2015, , 809, 78

Kwon, W., Looney, L. W., Mundy, L. G., Chiang, H.-F., & Kemball, A. J. 2009, , 696, 841

Lada, C. J. 1987, in IAU Symposium, Vol. 115, Star Forming Regions, ed. M. Peimbert & J. Jugaku, 1

Lada, C. J. & Wilking, B. A. 1984, , 287, 610

Lay, O. P., Carlstrom, J. E., & Hills, R. E. 1997, , 489, 917

LeBlanc, F. 2010, An Introduction to Stellar Astrophysics by Francis LeBlanc. Wiley, 2010. ISBN: 978-0-470-69956-0

Lommen, D., Maddison, S. T., Wright, C. M., et al. 2009, , 495, 869

Mackay, D. J. C. 2003, Information Theory, Inference and Learning Algorithms, 640

Mason, B., Dicker, S., Sadavoy, S., et al. 2020, , 893, 13

Mathis, J. S., Rumpl, W., & Nordsieck, K. H. 1977, , 217, 425

McClure, M. K., Furlan, E., Manoj, P., et al. 2010, , 188, 75

Meny, C., Gromov, V., Boudet, N., et al. 2007, , 468, 171

Michelson, A. A. & Pease, F. G. 1921, , 53, 249

Mie, G. 1908, Annalen der Physik, 330, 377

Miotello, A., Testi, L., Lodato, G., et al. 2014, , 567, A32

Myers, P. C. & Ladd, E. F. 1993, , 413, L47

Natta, A. & Testi, L. 2004, in Astronomical Society of the Pacific Conference Series, Vol. 323, Star Formation in the Interstellar Medium: In Honor of David Hollenbach, ed. D. Johnstone, F. C. Adams, D. N. C. Lin, D. A. Neufeeld, & E. C. Ostriker, 279

Natta, A., Testi, L., Calvet, N., et al. 2007, Protostars and Planets V, 767

Oliveira, I., Pontoppidan, K., 'i n, B. M., et al. 2010, Astrophysical Journal, 714, 778

Olofsson, J., Augereau, J. C., van Dishoeck, E. F., et al. 2009, , 507, 327

Ormel, C. W., Paszun, D., Dominik, C., & Tielens, A. G. G. M. 2009, Astronomy & Astrophysics, 502, 845

Ortiz-León, G. N., Loinard, L., Dzib, S. A., et al. 2018, , 865, 73

Ortiz-León, G. N., Loinard, L., Kounkel, M. A., et al. 2017, , 834, 141

Ossenkopf, V. & Henning, T. 1994, , 291, 943

Pagani, L., Bacmann, A., Steinacker, J., Stutz, A., & Henning, T. 2011, in EAS Publications Series, Vol. 52, EAS Publications Series, ed. M. Röllig, R. Simon, V. Ossenkopf, & J. Stutzki, 225–228

Pagani, L., Steinacker, J., Bacmann, A., Stutz, A., & Henning, T. 2010, Science, 329, 1622

Palla, F. & Stahler, S. W. 1990, , 360, L47

Palla, F. & Stahler, S. W. 1991, , 375, 288

Paradis, D., Bernard, J. P., Mény, C., & Gromov, V. 2011, , 534, A118

Peraiah, A. 2001, The equation of radiative transfer (Cambridge University Press), 2963

Pérez, L. M., Carpenter, J. M., Chandler, C. J., et al. 2012, , 760, L17

Pérez, L. M., Chandler, C. J., Isella, A., et al. 2015, , 813, 41

Pineda, J. E., Arce, H. G., Schnee, S., et al. 2011, , 743, 201

Pineda, J. E., Offner, S. S. R., Parker, R. J., et al. 2015, , 518, 213

Pinilla, P., Birnstiel, T., Ricci, L., et al. 2012, , 538, A114

Pinte, C., Ménard, F., Duchêne, G., & Bastien, P. 2006, , 459, 797

Pollack, J. B., Hollenbach, D., Beckwith, S., et al. 1994, , 421, 615

Press, W., Teukolsky, S., Vetterling, W., & Flannery, B. 2007, Numerical Recipes: The Art of Scientific Computing, 3rd edn. (Cambridge University Press)

Redaelli, E., Alves, F. O., Caselli, P., et al. 2017, , 850, 202

Riaz, B., Martín, E. L., Bouy, H., & Tata, R. 2009, , 700, 1541

Ricci, L., Testi, L., Natta, A., & Brooks, K. J. 2010a, , 521, A66

Ricci, L., Testi, L., Natta, A., et al. 2010b, , 512, A15

Ricci, L., Testi, L., Natta, A., et al. 2010c, , 512, A15

Robitaille, T. P. 2011, , 536, A79

Rodmann, J., Henning, T., Chandler, C. J., Mundy, L. G., & Wilner, D. J. 2006, , 446, 211

Román-Zúñiga, C. G., Frau, P., Girart, J. M., & Alves, J. F. 2012, , 747, 149

Rybicki, G. B. & Lightman, A. P. 1979, Radiative processes in astrophysics

Sadavoy, S. I., Stutz, A. M., Schnee, S., et al. 2016, ArXiv e-prints [[arXiv]1601.06769]

Sakai, N., Oya, Y., Sakai, T., et al. 2014a, , 791, L38

Sakai, N., Sakai, T., Hirota, T., et al. 2014b, , 507, 78

Sallum, S., Follette, K. B., Eisner, J. A., et al. 2015, , 527, 342

Sault, R. J., Teuben, P. J., & Wright, M. C. H. 1995, in Astronomical Society of the Pacific Conference Series, Vol. 77, Astronomical Data Analysis Software and Systems IV, ed. R. A. Shaw, H. E. Payne, & J. J. E. Hayes, 433

Schräpler, R. & Henning, T. 2004, , 614, 960

Segura-Cox, D. M., Harris, R. J., Tobin, J. J., et al. 2016, , 817, L14

Segura-Cox, D. M., Looney, L. W., Tobin, J. J., et al. 2018, , 866, 161

Sheehan, P. D. & Eisner, J. A. 2017, , 851, 45

Sheehan, P. D. & Eisner, J. A. 2018, , 857, 18

Stephens, I. W., Bourke, T. L., Dunham, M. M., et al. 2019, arXiv e-prints, arXiv:1911.08496

Stephens, I. W., Dunham, M. M., Myers, P. C., et al. 2018, , 237, 22

Stephens, I. W., Dunham, M. M., Myers, P. C., et al. 2017, , 846, 16

Tafalla, M., Myers, P. C., Caselli, P., Walmsley, C. M., & Comito, C. 2002, , 569, 815

Tazzari, M., Beaujean, F., & Testi, L. 2017, galario: Gpu Accelerated Library for Analyzing Radio Interferometer Observations

Tazzari, M., Beaujean, F., & Testi, L. 2018, , 476, 4527

Tazzari, M., Testi, L., Ercolano, B., et al. 2016a, , 588, A53

Tazzari, M., Testi, L., Ercolano, B., et al. 2016b, , 588, A53

Testi, L., Birnstiel, T., Ricci, L., et al. 2014, Protostars and Planets VI, 339

Tobin, J. J., Dunham, M. M., Looney, L. W., et al. 2015, , 798, 61

Tobin, J. J., Hartmann, L., Chiang, H.-F., et al. 2013, , 771, 48

Tobin, J. J., Hartmann, L., Looney, L. W., & Chiang, H.-F. 2010, , 712, 1010

Tobin, J. J., Looney, L. W., Li, Z.-Y., et al. 2016, , 818, 73

Tychoniec, Ł., Manara, C. F., Rosotti, G. P., et al. 2020, arXiv e-prints, arXiv:2006.02812

Tychoniec, Ł., Tobin, J. J., Karska, A., et al. 2018, , 238, 19

Ubach, C., Maddison, S. T., Wright, C. M., et al. 2012, , 425, 3137

Ulrich, R. K. 1976, , 210, 377

van Cittert, P. H. 1934, Physica, 1, 201

Weidenschilling, S. J. 1977, Monthly Notices of the Royal Astronomical Society, 180, 57

Weintraub, D. A., Sandell, G., & Duncan, W. D. 1989, , 340, L69

White, R. J. & Hillenbrand, L. A. 2004

Wong, Y. H. V., Hirashita, H., & Li, Z.-Y. 2016, , 68, 67

Woody, D. P., Scott, S. L., Scoville, N. Z., et al. 1989, , 337, L41

Youdin, A. N. & Shu, F. H. 2002, , 580, 494

Ysard, N., Köhler, M., Jones, A., et al. 2016, , 588, A44

Zernike, F. 1938, Physica, 5, 785

Zhao, B., Caselli, P., Li, Z.-Y., & Krasnopolsky, R. 2018, , 473, 4868

Zhao, B., Caselli, P., Li, Z.-Y., et al. 2016, , 460, 2050

Zucker, C., Schlafly, E. F., Speagle, J. S., et al. 2018, ArXiv e-prints [[arXiv]1803.08931]

Acknowledgments

The last months have been the craziest of my life. It was difficult to believe that I would be finishing my thesis under a global pandemic, but thanks to the support of many people, this chapter has come to the end. My grateful thanks to Paola Caselli to give me the opportunity and freedom to choose my PhD project and be the most patience and supportive supervisor that is needed in this journey. I would like to thank to Jaime Pineda, László Szűcs and Dominique Segura-Cox, without your patience, mentorship and discussions during my time at CAS, I would not be here today. I also want to thank my collaborators Leonardo Testi, Anna Miotello, Marzo Tazzari, Mike Dunham and Ian Stephens for their valuable guidance at the beginning of my PhD and in the development of my first publication.

Agradezco a Felipe y Victor, por las risas, por el apoyo y ayudarme con los últimos detalles de este manuscrito. Ana, muchas gracias por tu apoyo a pesar de la distancia.

I thank to the entire CAS group, thank you all for the great time we spent together chatting in the coffee room, IMPRS parties, birthdays and Ringberg retreats. I would also like to thank my office mates Johanna, Elena and Domenico, thanks for the laughs, conversations and the support when I needed it.

To my Star Tres, Javiera and Karina, thank you very much to share with my this passion for science and outreach. Even during the hardest times these past years, Star Tres reminded me why I become a scientist and helped to keep motivated.

I would like to acknowledge the financial support of the Agencia Nacional de Investigación y Desarrollo/Becas Chile/Nr. 5594/2015.

Agradezco a mi familia, Pablo, Cristina, Contanza, Cristi y Juan Pablo, los más de 12 mil kilometros que nos separan nunca fueron un impedimento para sentir su apoyo en este sueño. Gracias infinitas por darme ánimos y por no dudar nunca de mis capacidades. A mis segundos padres, Ana y Claudio, gracias por sus palabras de energía durante todos estos años. A mis amigas de la vida, Carolina, Nadia, Catalina, Alejandra, Natalia y Macarena, gracias por su apoyo, por recibirme con los brazos abiertos cada vez que pude viajar a Chile y por sacarme sonrisas con sus historias y bebés.

Finalmente, quiero agradecer a mi mejor amigo y compañero de vida Matías. Sin tu amor y apoyo durante todos estos años nada de esto sería posible. Hasta el infinito y más allá juntos.